Two-dimensional Wakes and Fluid-structure Interaction of Circular Cylinders in Cross-flow

Wenchao Yang

Dissertation submitted to the Faculty of the
Virginia Polytechnic Institute and State University
in partial fulfillment of the requirements for the degree of

Doctor of Philosophy
in
Engineering Mechanics

Mark A. Stremler, Chair
James Hanna
Sunghwan Jung
Shane D. Ross
Pengtao Yue

September 20, 2018
Blacksburg, Virginia

Keywords: Wake interaction, Flow-induced vibration, Vortex dynamics.

Two-dimensional Wakes and Fluid-structure Interaction of Circular Cylinders in Cross-flow

Wenchao Yang

(ABSTRACT)

The wake of a bluff body is a representative issue in vortex dynamics that plays a central role in civil engineering, ocean engineering and thermal engineering. In this work, a flowing soap film was used to investigate the wakes of multiple stationary circular cylinders and of a single oscillating cylinder. Corresponding computer simulations were also conducted. Vortex formation of a stationary circular cylinder was analyzed by proper orthogonal decomposition (POD). The POD analysis was used to define an unsteady vortex formation length, which suggests a relationship between the vortex formation length of a single cylinder and the critical spacing of two cylinders in a tandem arrangement. A systematic parametric study of the wake structure was conducted for a controlled transversely oscillating cylinder. Neural network and support vector machine codes assisted the wake classification procedure and the identification of boundaries between different wake regimes. The phase map of the vortex shedding regimes for the (quasi) two-dimensional experiment qualitatively agrees with previous three-dimensional experiments. The critical spacings of two identical tandem circular cylinders in a flowing soap film system were determined using visual inspections of the wake patterns and calculations of the Strouhal frequencies. The dimensionless spacing was both increased and decreased quasi-statically. Hysteresis was observed in the flow patterns and Strouhal numbers. This study appears to provide the first experimental evidence of critical spacing values that agree with published computational results. The wake interaction between a stationary upstream circular disk and a free downstream circular disk was also investigated. With the ability to tie together the wake structure and the object motion, the relationship between energy generation and flow structure in the simplified reduced order

model system was studied. The research results find the optimal efficiency of the energy harvesting system by a parametric study.

Two-dimensional Wakes and Fluid-structure Interaction of Circular Cylinders in Cross-flow

Wenchao Yang

(GENERAL AUDIENCE ABSTRACT)

The wake of a bluff body is a classic issue in vortex dynamics that has been the subject of much research in civil engineering, ocean engineering and thermal engineering. Bluff bodies, especially circular cylinders, can be found extensively in heat exchangers, cooling systems and offshore structures. Flow-induced vibration of a bluff body due to the formation of a wake is an important problem in many fields of engineering. Flow-induced vibration determines the oscillation of flexible pipes that transfer oil from the seabed to the surface of the ocean, for example [71]. In civil engineering, flow-induced vibration affects the design of bluff structures in wind such as bridges, chimneys and buildings [62]. Flow-induced vibration caused by vortices being shed from a bluff body is also a promising way to extract energy from geophysical flows [10]. FIV energy harvesting systems are especially suitable for slow flow speeds in the range 0.5-1.5m/s which cannot be efficiently harvested by traditional hydroelectric power technologies. When a pair of tandem cylinders is immersed in a flow, the downstream cylinder can be excited into wake-induced vibrations (WIV) due to the interaction with vortices coming from the upstream cylinder.

In this work, a flowing soap film was used to investigate the flow-induced vibration of the downstream cylinder of a tandem pair. With the ability to tie together the wake structure and the object motion, we investigate the relationship between energy generation and flow structure in the reduced order model system. The research results find the optimal efficiency of the energy harvesting system by a parametric study. To get deep physical understanding of the flow-induced vibration, wake structures of a circular cylinder undergoing controlled motion and the critical spacing of two identical tandem circular cylinders were also investi-

gated in this research. These research results can help not only the optimization of energy harvesting systems based on flow-induced vibration of the circular-cylinder system, but also will benefit the understanding of wake interactions between multiple bluff bodies such as schooling fish, natural draft cooling towers and wind turbine farms.

Dedication

Dedicated to my parents Kun Yang and Lihua Chang,

and to my wife Qian Liang.

Acknowledgments

First, I would like to pay special thankfulness, warmth and appreciation to my doctoral advisor Dr. Mark A. Stremler, who supported and assisted me at every point during my research. His advices for my research proved to be a significant effort towards the completeness of my degree. This significant career move is inseparable from his continuing encouragement and professional guidance.

I would also like to show my gratitude to my doctoral committee members Dr. Pengtao Yue, Dr. Shane D. Ross, Dr. Sunghwan Jung, and Dr. James Hanna for valuable opinions and constructive suggestions on my study and research. And, I sincerely thank all the graduate students at Virginia Tech with whom I have collaborated at various phases of my doctoral years. Most notable among them are Gary Nave, Saikat Basu, Souvick Chatterjee, Sean Gart, Brian Chang, and Farzad Ahmadi. I would like to pay my regards to Dr. Todd Lowe from aerospace engineering. I have benefited greatly from the data analysis in fluid dynamics course which he had taught at Virginia Tech. I also wish to present my special thanks to the staff-members at the Engineering Mechanics program, more specifically Sally Shrader, Lisa L. Smith, Dave Simmons, Darrell Link, Mark Warbeck, Tim Tomlin, Melissa Nipper and Jessica Grimes for helping me out with the various administrative details.

Finally, I would like to show my gratitude to my parents, Kun Yang and Lihua Chang, and my beloved wife Qian Liang for their love and sacrifices. None of my academic or non-academic pursuits and achievements would have been possible without the strong family support, particularly from Qian, who has stood by me through all hard and happy times.

Table of contents

List of Figures

List of Tables

List of Abbreviations

A Oscillation amplitude

μ_b Bulk viscosity of soap film

ℓ_{c} Critical spacing between two tandem cylinders

$\ell_{\mathrm{c,max}}$ Maximum spacing between two tandem cylinders

$\ell_{\mathrm{c,min}}$ Minimum spacing between two tandem cylinders

D Diameter of the circular cylinder

ρ Desity of a fluid

D_{d} Diameter of the circular disk

h_{d} Thickness of the circular disk

μ_f Effective viscosity of soap film

E_M Marangoni elasticity energy

h_{f} Thickness of the soap film

L Vortex formation length of single cylinder

$L_{\mathrm{I,max}}$ Maximum vortex formation length based on POD analysis of image intensity

$L_{\mathrm{I,min}}$ Minimum vortex formation length based on POD analysis of image intensity

$L_{\mathrm{p,max}}$ Maximum vortex formation length based on POD analysis of pressure field

$L_{\mathrm{p,min}}$ Minimum vortex formation length based on POD analysis of pressure field

L_r Vortex formation length for mean recirculation region

L_f Vortex formation length for maximum velocity fluctuation

$L_{\mathrm{u,max}}$ Maximum vortex formation length based on POD analysis of stream-wise velocity

$L_{\mathrm{u,min}}$ Minimum vortex formation length based on POD analysis of stream-wise velocity

Fr Froude number

f Oscillation frequency

f_N Shedding frequency of the stationary cylinder

f^* Frequency ratio

g Longitudinal gap between two tandem cylinders

M_e Elastic Mach number

m_D Mass of circular disk

m_f Mass of soap film (the same area of circular disk)

m^* Mass ratio

A^* Normalized oscillation amplitude

P_1 First intensity probe

P_2 Second intensity probe

V_r $U_\infty/f_N D_{\mathrm{d}}$ Reduced velocity

Re Reynolds number

Sc	Scruton number
s	Separation between two tandem cylinders
v_M	Marangoni wave speed
ℓ	Longitudinal spacing between two tandem cylinders
U_∞	Flow speed
St	Struhal number
S	Surface area
Γ	Surface concentration of soap film
μ_S^s	Surface Poise of soap film
σ	Surface tension of soap film
η	Thickness variations of soap film
$\boldsymbol{u}$	Velocity field in the two-dimensional plane
K^*	Virtual thickness of the interface
μ	Viscosity of a fluid
λ^*	$U_\infty / f D_\mathrm{d}$ Normalized wavelength

Chapter 1

Introduction

1.1 Overview

The wake of a bluff body is a representative issue in vortex dynamics that has played a central role in civil engineering, ocean engineering and thermal engineering. The structure and dynamics of a vortex wake can change the pressure distribution on the object forming the wake. Therefore the alternate shedding of vortices can result in periodic forces on the object, which then induce it to oscillate. This issue of vortex-induced vibration is a classic problem in fluid mechanics because of many applications from engineering. For example, this fluid-structure interaction determines the oscillation of flexible tubes that transfer oil from the seabed to the surface [71]. In civil engineering, vortex-induced vibration also affects the design of bluff structures in wind such as bridges, chimneys and buildings [62]. Due to the complexity of wakes for bluff structures both alone and in groups, many issues regarding vortex street classification, multiple vortex interactions, and fluid-structure interaction are poorly understood. Previous research results have included theoretical, experimental and numerical analyses [1, 45, 69]. On the whole, most experiments have been performed in either a water tunnel or a wind tunnel and are thus three dimensional (3D) [2, 69, 99]. However, most numerical simulations focus on two-dimensional (2D) flows [45, 55, 67, 72, 89, 97]. This PhD research focuses on quasi-2D experiments in a flowing soap film and corresponding 2D simulations. By comparing the present results with previous 3D results from the literature

[2, 69], the role of 3D effects on the wake patterns of tandem and oscillating cylinders is evaluated.

Soap film systems have been widely applied to investigate (quasi-) 2D flows [102, 106, 117] and have been utilized by various research groups for exploring wake structures (see, e.g., [22, 88]). Three decades ago, Couder & Basdevant [22] found that a "2P" wake can be produced in a soap film by in-line oscillation of a circular cylinder. Schnipper *et al.* [88] carried out a systematic parametric study of wakes behind a flapping foil and classified several different wake patterns. The other studies conducted on flowing soap films are closely associated with this PhD research work and will be fully discussed in the following sections [5, 43].

For this PhD research work, the experimental systems were developed; a variety of flow measurements and visualizations were conducted; the wake of one or two circular cylinders was simulated by a two-dimensional Lattice Boltzman method; and the gathered data was processed, modeled and analyzed by many scientific methods and algorithms. Chapter 2 introduces the research appoach in this PhD work consisting of the experimental setup, numerical methods and data analysis algorithms. Chapter 3 illustrates a new definition of vortex formation length based on POD analysis. Chapter 4 presents the wake structures of a circular cylinder undergoing controlled motion. Wake structures of two stationary tandem circular cylinders are shown in Chapter 5. Chapter 6 dicusses flow-induced vibration of the downstream cylinder of a tandem pair.

The purpose of this PhD research work is aimed in part at revealing the significance of dimensionality in the wake patterns. Three-dimensional effects can play an important role in vortex wake dynamics [12, 26, 115]. However, there is both historical [46, 47, 48] and recent [14, 100] evidence that a two-dimensional model can provide important information about the structure and dynamics of a vortex-dominated wake and the forces it produces on the

generating body. Therefore, the fundamental issues are necessary to be understood within two-dimensional models before substantive progress can be made on a three-dimensional theory of exotic wake development.

1.2 Vortex formation of a stationary circular cylinder

Although vortex formation in the wake of a single cylinder has been a fundamental subject in vortex dynamics for many years, the understanding of the wake behind a bluff body remains incomplete. One of these unknown issues is how a separating free shear layer evolves into the classical vortex street configuration. von Kármán first conducted the original flow stability analysis of vortex street configurations and inspired many studies on the instability of a vortex array [1, 6, 7]. However, these instability analyses did not connect the infinite vortex arrays with the wake right after the bluff bodies. Thus the physical understanding of the wake right behind a bluff body and the vortex street formation has been the critial purpose of many experimental and numerical studies.

Many investigations have been conducted on bluff body wakes in order to estimate the length and the width of the "vortex formation" region. One definition of the "vortex formation" length is the distance between the center of the cylinder and the location of the streamline saddle point (wake stagnation point) in a time averaged field [44, 73, 78, 96] . This "vortex formation length" definition, which is based on a mean recirculation region in the wake as shown in Figure 1.1(I), depends on the dimensionality of the flow and the Reynolds number. Nishioka & Sato [73] found that the formation length at $Re = 100$ is about 1.9 diameters in a low-speed wind tunnel. Similarly, Papaioannou *et al.* [78]'s two-dimensional simulation also obtained a formation length of 1.9 diameters at $Re = 100$. Jiang & Cheng [44] confirm that the formation length is around 2 in their two-dimensional simulation. The variation of the

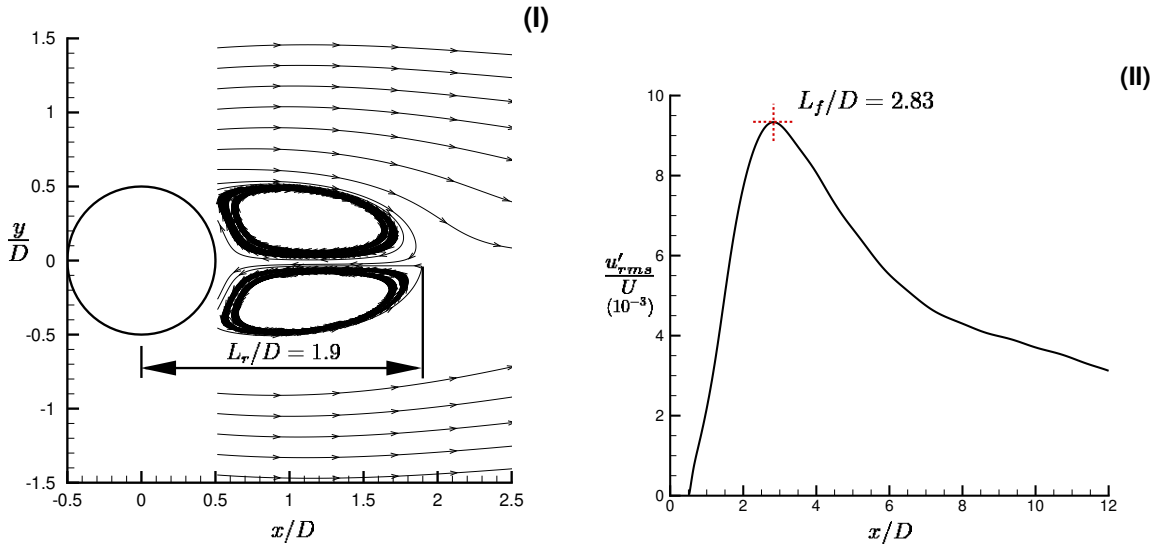

Figure 1.1: Definitions of vortex formation of a cylinder wake ($Re = 100$): (I) mean recirculation; (II) maximum velocity fluctuation

recirculation region length with Reynolds number as predicted by Papaioannou *et al.* [78]'s two-dimensional simulation is shown in Figure 1.2. In the low Reynolds number regime ($Re < 500$), the formation length decreases monotonically with an increase of Re. Papaioannou *et al.* [78]'s numerical studies show that the qualitative variation of formation length (based on mean recirculation region) as Re increases appears consistent with the variation of the critical spacing of two tandem cylinders in both two- and three-dimensional simulation. However, the vortex formation length is much smaller than the critical spacing.

Another important definition of the "vortex formation length" refers to the point at which the velocity fluctuation increases to a maximum [8, 34], as shown in Figure 1.1(II). Figure 1.3 summarizes several definitions of the formation region length from experiments. The results of Griffin & Ramberg [35] show the position of maximum velocity fluctuation on the wake centerline. This definition of formation length decreases monotonically from 2.9 to 1.8 with the increase of Re from 120 to 350.

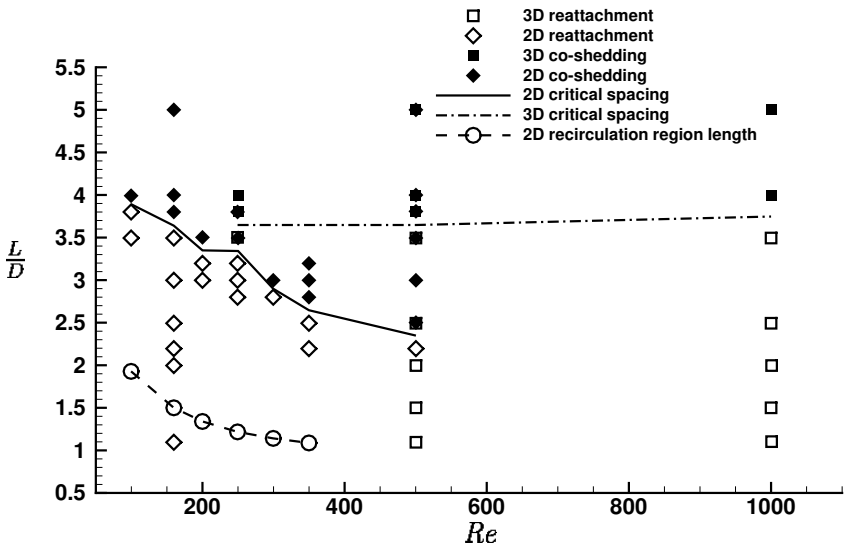

Figure 1.2: Vortex formation length and critical spacing as the change of Reynolds number in two- and three-dimensional simulations. □, three-dimensional reattachment wake; ◇, two-dimensional reattachment wake; ■, three-dimensional co-shedding wake; ◆,two-dimensional co-shedding wake; ——,middle distance between L/D of last reattachment wake and first co-shedding wake of two-dimensional simulations for given Re; $-\cdot-$, middle distance between L/D of last reattachment wake and first co-shedding wake of three-dimensional simulations for given Re; $--\circ--$, variation of the recirculation region length for a single stationary cylinder with Re (two-dimensional prediction).

In general, most definitions of vortex formation length decrease with increasing Re for the low Reynolds number regime ($Re < 400$). Similary, the critical spacing between two tandem cylinders also decreases monotonically with the increase of Re in a two-dimensional simulation (see Figure 1.2). However, an exact connection between the formation length of a single cylinder and the critical spacing of two tandem cylinders has not been determined [78]. For one part of this PhD work, a new definition of the vortex formation length based on the unsteady flow is introduced. Proper orthogonal decomposition (POD) was used to define the maximum and minimum vortex formation lengths, which relate to the maximum and minimum critical spacing, respectively. The POD reconstruction then decomposed the spatiotemporal flow field into two individual parts and generated a reduced order model of the unsteady flow field. The POD analysis provides a direct connection between the new

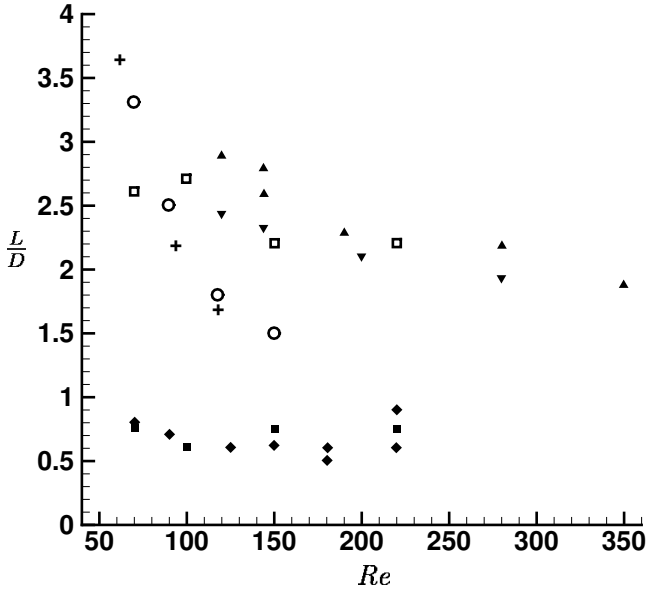

Figure 1.3: Vortex formation in the near wake of a circular cylinder as the change of the distance L/D downstream and the Reynolds number Re. Green & Gerrard [31]: ■, formation of separated area of vorticity, which is eventually partially shed; □, position of vortex center downstream from the shear stress region and, at same time, the position of maximum vortex strength. Gerrard [28]: ♦, the formation region length determined by dye injection. Schaefer & Eskinazi [87]: +. Nishioka & Sato [73]: ○, location of maximum longitudinal velocity amplitude at the fundamental shedding (Strouhal) frequency (off the wake centreline). Griffin [32, 33]: ▼. Griffin & Ramberg [35]: ▲, location of maximum longitudinal velocity amplitude at twice the shedding (Strouhal) frequency (on the wake centreline).

definition of the vortex formation length and the critical spacing. The POD analysis also benefits the understanding of the vortex formation process and the wake interaction between multiple bluff bodies.

1.3 Wake structures of a circular cylinder undergoing controlled motion

To better understand vortex-induced vibration phenomena, many researchers have investigated the controlled vibration of a cylindrical body in a water channel flow, where the cylinder is effectively translated with a prescribed sinusoidal trajectory relative to the fluid [69, 105]. Morse & Williamson [69]'s controlled-vibration experiment confirmed that it is possible to predict the response of a freely vibrating cylinder by employing the force-contour data from a forced cylinder experiment.

Williamson & Roshko [105] observed a set of different vortex-formation modes, existing within certain regimes in a plot of normalized amplitude and wavelength of the body motion, as shown in Figure 1.4 [105]. Among the vortex-formation modes they found were a "2S" mode representing two single vortices formed per cycle, a "2P" mode meaning two pairs of vortices formed per cycle, and an asymmetric "P+S" mode comprised of a pair of vortices and a single vortex in each cycle, as shown in Figure 4.3. The controlled motion data of recent experiments by Morse & Williamson [68, 69, 70] has already proved to predict steady, unsteady and transient vortex-induced vibration.

Different from the experimental results, simulation results show another map of the vortex-shedding regime for controlled motion of a cylinder. Leontini *et al.* [53] employed two-dimensional numerical simulations and found no "2P" mode wake pattern, as shown in Figure 1.5. In addition, the synchronization regime and the wake modes observed within the synchronized regime were shown to be Re dependent. Leontini *et al.* [53] conjecture that the difference with the experimental results is related to the differences in flow dimensionality and Reynolds number but without any concrete explanation. The obvious reason for the difference would appear to be the effect of the third spatial dimension in the experiments.

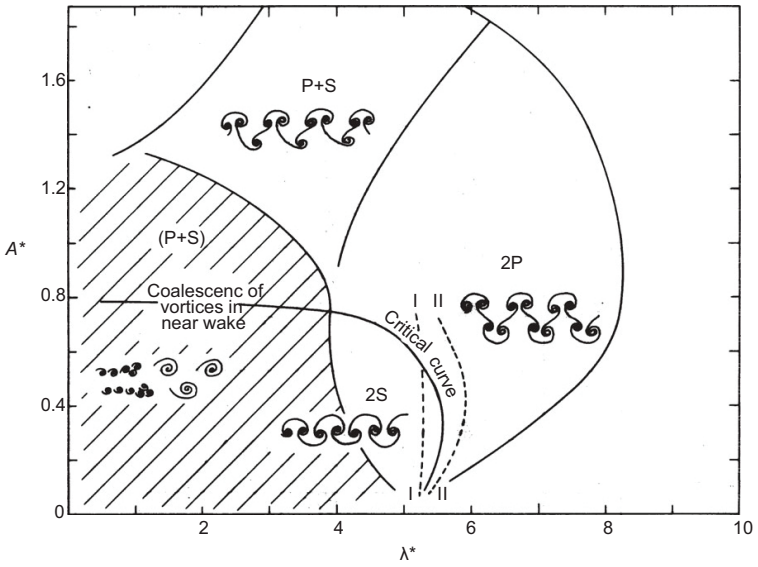

Figure 1.4: Map of vortex-shedding regimes obtained by Morse & Williamson [69] for $300 < Re < 3000$.

Williamson & Roshko [105] state that the "P+S" mode replaces the "2P" mode when $Re < 300$. Thus the "2P" mode probably derives from the three-dimensional flow. However, this conjecture has not been validated by other experimental results.

A similar systematic parametric study of wake structure has been performed for a flapping foil [88]. Various wakes were visualized by Schnipper *et al.* [88] in a flowing soap, including the von Karman vortex street, the inverted von Karman vortex street, 2P wakes, 2P+2S wakes and novel wakes ranging from 4P to 8P, with variation of the frequency and amplitude of the oscillation. Mareck *et al.* [63] also observed the 2P wake in the flowing soap for the wake of a flexible loop. The flowing soap film has the advantage of effective and economic flow visualization, which can provide the details of the vortex formation process.

To investigate the role of system dimensionality in the wake structure of an oscillating cylinder, a variety of experiments were conducted in a flowing soap film tunnel as one part of this PhD work, as shown in Chapter 4. A systematic parametric study of the wake structure produced was investigated in the frequency-amplitude-space accessible to the soap

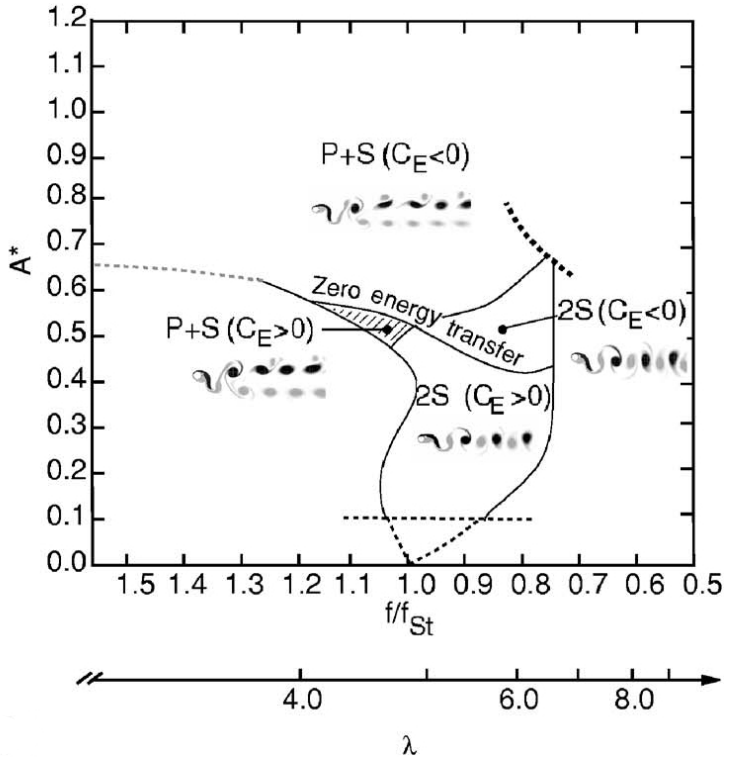

Figure 1.5: Map of vortex-shedding regimes obtained by Leontini *et al.* [53] for $Re = 300$.

film experimental system.

1.4 Wake structures of two stationary tandem circular cylinders

Classifying the system behavior when a steady cross flow encounters two immersed, stationary circular cylinders aligned one behind the other is a classic problem that idealizes the situation encountered in many engineering applications. A schematic of the basic system configuration is shown in Figure 1.6(a). Upstream of the cylinders, a fluid with constant viscosity μ and density ρ is assumed to be moving steadily in the x direction with a uniform speed U_∞. The cylinders both have diameter D, and their centers are separated in the x

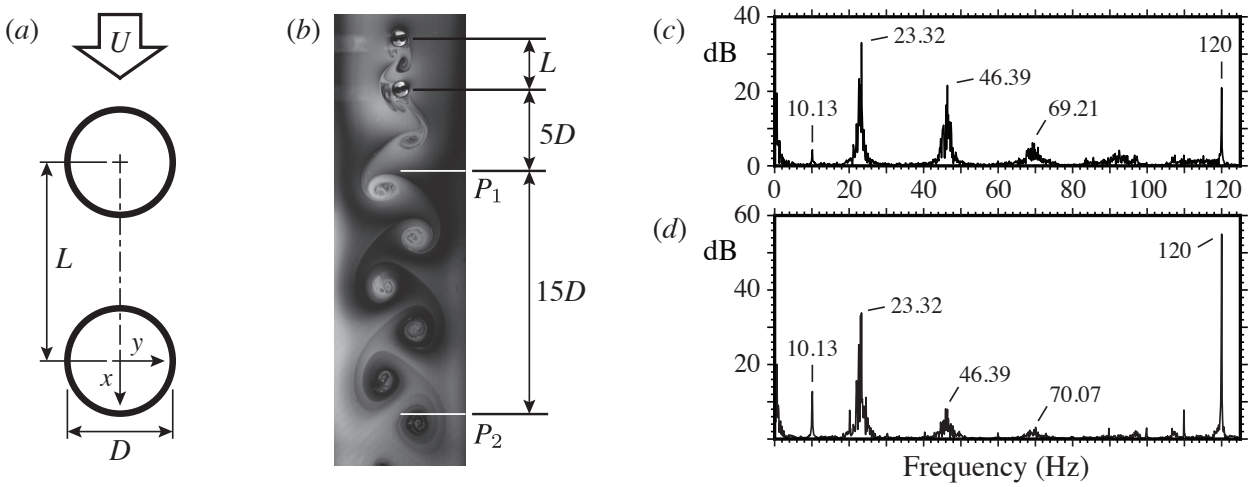

Figure 1.6: Flow past two stationary circular cylinders in tandem arrangement: (*a*) Schematic of the tandem cylinder configuration. (*b*) Probe locations used to determine Strouhal numbers (white lines). Probe P_1 is located at $x = 5D$ and probe P_2 at $x = 20D$. Both probe areas measure $3 \times 197\,\mathrm{px}^2$. Example spectra are shown from (*c*) P_1 and (*d*) P_2 for the case $\ell = 3.03$ with decreasing spacing in Trial 3 (see details in Chapter 5). The peak at 23.32 Hz corresponds to vortex shedding; the peak at 120 Hz is from the light source.

direction by a distance s. In general the cylinders may also be separated transversely; here it is assumed that there is no such offset in the y direction, so that the two cylinders are aligned in tandem in the direction of the flow. For flow at a given Reynolds number, $Re = \rho U_\infty D/\mu$, the system behavior can be parameterized by the dimensionless cylinder spacing, $\ell = s/D$; the gap ratio, $g = \ell - 1$, is used in some analyses. This discussion presumes $Re \gtrsim 50$ so that vortex shedding would occur in the flow past an isolated cylinder [103].

Most of the published research results [see, e.g., the reviews by 76, 93, 111, 114, 118] agree that for steady flow past identical, smooth, tandem, circular cylinders with $50 \lesssim Re \lesssim 2.5 \times 10^5$ there exists a particular value of the dimensionless cylinder spacing, the *critical spacing* ℓ_c, at which several key flow characteristics change abruptly: the flow pattern in the gap between the cylinders; the Strouhal number in the wake, $St = fD/U_\infty$, where f is the characteristic frequency; and the lift and drag forces on the cylinders. The critical spacing ℓ_c is sometimes referred to as the *drag inversion separation* [16] because of the abrupt change

in drag force. However, there has not been a clear consensus regarding the value of ℓ_c.

Several different flow regimes can be identified as a function of the cylinder spacing; the classification by [114] identifies three basic regimes, although other classifications may be used [17, 38]. When the two cylinders are very close together, the shear layers that separate from the upstream cylinder flow past the second cylinder and generate vortices in the downstream wake. The flow pattern is thus similar to that for a single elongated bluff body [38], giving the *extended body regime* shown in Figure 5.1(a,i). For intermediate values of $\ell < \ell_c$, the shear layers shed by the upstream cylinder reattach on the surface of the downstream cylinder, giving the *reattachment regime* shown in Figure 5.1(b,c,h). The reattachment regime can itself be divided into two regimes consisting of "after-body" reattachment and "fore-body" reattachment [108, 114]. For all cases with $\ell < \ell_c$, the upstream cylinder does not shed vortices into the gap region. For $\ell > \ell_c$, in contrast, vortices are shed from the upstream cylinder into the gap between cylinders, giving the *co-shedding regime* shown in Figure 5.1(d–g), which is sometimes referred to as the *wake-in-the-gap regime* [18]. As ℓ is increased to greater than ℓ_c, the downstream Strouhal number and the lift and drag forces on both cylinders increase suddenly and significantly [see, e.g., Figure 5.2 and the reviews by 76, 93, 111, 114, 118].

For cylinder spacings near ℓ_c, bistable behavior has been observed, with the flow switching intermittently between the reattachment regime and the co-shedding regime [38, 114]. A computational study at low Re found that this bistable behavior is due to both regimes existing as stable solutions for a range of spacing values, $\ell_{c,\min} \leq \ell \leq \ell_{c,\max}$ [67]. Initial conditions influence which solution appears, giving a hysteresis effect as the system parameters are varied [67, 112]. If, for example, a flow is established in the co-shedding regime with $\ell > \ell_{c,\max}$, then quasi-statically reducing the spacing until $\ell < \ell_{c,\max}$ can maintain co-shedding behavior for $\ell_{c,\min} < \ell < \ell_{c,\max}$ [41, 98]. Conversely, gradually increasing the spacing from $\ell < \ell_{c,\min}$

can maintain flow in the reattachment regime for $\ell_{c,min} < \ell < \ell_{c,max}$. This hysteresis effect has also been observed when varying the Reynolds number [17, 94, 108, 112].

The published results generally agree that $3 \leq \ell_c \lesssim 5$ for $50 \lesssim Re \lesssim 10^4$ and $3 \leq \ell_c \lesssim 4$ for $10^4 \lesssim Re \lesssim 2.5 \times 10^5$. However, there is poor agreement regarding more precise bounds on ℓ_c. At $Re \approx 1.5 \times 10^4$, for example, Kiya *et al.* [50] found $3 \leq \ell_c \leq 3.5$, Igarashi [38] gave $3.3 \lesssim \ell_c \lesssim 3.6$ [see 38, fig. 16], Xu & Zhou [108] showed $3.5 \leq \ell_c \leq 4$, and Ishigai *et al.* [39] reported $3.8 \leq \ell_c \leq 4$. There is even disagreement in the detailed values reported by the same research group: for $Re \approx 10^5$, Zdravkovich [111] showed $3 \leq \ell_c \leq 3.5$ in their figures 1 and 3, while Zdravkovich [111] showed $3.5 \leq \ell_c \leq 4$ in his figure 9; curiously, the latter data is cited as being from Zdravkovich [111].

Some discrepancy in the various results may be explained by the resolution of the data — a number of studies considered spacing increments of $\Delta\ell = 0.5$ or larger. Furthermore, the influence of hysteresis on the results has been investigated inconsistently, having been considered explicitly by only a subset of the available studies [17, 38, 67, 94, 98, 108]. Those studies having low levels of background noise and using initial conditions that bias the flow toward one of the bistable states (such as ramping up the flow speed from rest) may find only a single transition in the flow behavior at $\ell \approx \ell_{c,min}$ or $\ell \approx \ell_{c,max}$ according to whether the initial condition biases toward the co-shedding regime or the reattachment regime, respectively. In addition to issues of resolution and solution bias, results are also known to depend on details such as the free-stream turbulence intensity [58]. For $Re > 190$ the wake is three-dimensional [16], with complex structures that have a clear influence on the value of ℓ_c [77]. Differences in cylinder end effects and aspect ratio have been given as possible explanations for discrepancies in the data [94].

This complex dependence of critical spacing on Reynolds number and other system details motivates focusing attention on $50 \lesssim Re \lesssim 190$, for which the wake is expected to remain

Experiments		
Reference	ℓ_c	method
Huhe-Aode [37] fig. 2	4.5–5.0	water in free-surface towing tank
Ohmi & Imaichi [74] fig. 2	≈ 5	water in free-surface towing tank
Ohmi *et al.* [75]	4–5	water in free-surface towing tank
Tasaka et al. *[94] fig. 8*	*$\approx$ 4.6–5*	*water in free-surface channel*
Wang et al. *[98] fig. 10*	*2.5–6.6*	*flowing soap film*
Computations		
Reference	ℓ_c	method
Li *et al.* [55] fig. 14	≈ 4	2D finite element method
Sharman *et al.* [89] fig. 14	3.75–4.0	2D finite volume method
Mizushima & Suehiro [67] figs. 10–12	*3.1–3.5*	*2D streamfunction-vorticity method*
Papaioannou *et al.* [77] fig. 8	3.8–4.0	2D/3D spectral/hp element method
Didier [25] fig. 2	3.95–4.0	2D finite volume method
Mahír & Altaç [61] table 5	3–4	2D finite volume method
Lee *et al.* [52] fig. 6	3.75–4.0	2D finite volume method
Mussa *et al.* [72] fig. 11	3.25–3.5	2D lattice Boltzmann method
Carmo et al. *[17] fig. 6*	*3.2–3.8*	*2D/3D spectral/hp element method*
Singha & Sinhamahapatra [91] fig. 17	3–5	2D finite volume method
Lin *et al.* [57] fig. 4	3.5–4	2D lattice Boltzmann method
Jiang *et al.* [45] fig. 4	3.5–4	2D lattice Boltzmann method
Tu *et al.* [95] fig. 4	3.5–4	2D finite element method
Vu *et al.* [97] fig. 6	4–4.2	2D finite volume method

Table 1.1: Previous results for critical spacing, ℓ_c, with $Re = 100$, listed chronologically. Italicized studies explicitly considered hysteresis effects.

laminar and two-dimensional [16], as a foundation for understanding tandem cylinder flow and the critical spacing. A summary of previously published experimental results for $Re = 100$ is shown in Table 1.1. With one exception, these experiments suggest that $4.5 \lesssim \ell_c \lesssim 5$. The outlying study by [98] used a flowing soap film system, while all others were conducted in a three-dimensional system. Huhe-Aode [37] showed the existence of bistable behavior for $4.5 \lesssim \ell \lesssim 5$, although they did not comment explicitly on this phenomenon. Ohmi *et al.* [75] focused on wake behavior for large values of ℓ and thus did not resolve the critical spacing beyond determining $4 \leq \ell_c \leq 5$. Tasaka *et al.* [94] demonstrated hysteresis in the value of the critical spacing when holding ℓ fixed and varying the value of Re: they found $4.6 \leq \ell_{c,min} \leq 4.7$ when Re is decreased, and $\ell_{c,max} \approx 5$ when Re is increased. The flowing soap film study by Wang *et al.* [98] also demonstrated hysteresis in the critical spacing, but in this study the Re value was held fixed and the cylinder spacing was varied quasi-statically. They reported $\ell_{c,max} = 6.6$ for increasing Re values and $\ell_{c,min} = 2.5$ for decreasing Re values, results that differ significantly from all other studies.

The laminar, 2D flow regime has the added benefit of being accessible to investigation via a number of computational methods. A summary of previously published computational results for $Re = 100$ is shown in Table 1.1. If one assumes that those computational studies not explicitly considering hysteresis were biased toward determining $\ell_{c,max}$ [77], these results can be interpreted as finding $3 \lesssim \ell_c \lesssim 4$ with a reasonable degree of consistency. The most significant deviation from this range is the study by Singha & Sinhamahapatra [91], which used the coarse resolution $\ell = 3, 4, 5$. Their results are also somewhat inconsistent, showing a jump in fluid forces on the cylinders for $3 < \ell_c < 4$ and a jump in the shedding frequency for $4 < \ell_c < 5$ [91, figure 17], suggesting that their computations give $\ell_{c,max} \approx 4$.

There is a consistent and significant discrepancy between the experimentally and computationally determined critical spacing for $50 \lesssim Re \lesssim 190$. Despite this disagreement, several

recent publications have used the established computational results for fixed tandem cylinders as the basis for code validation prior to performing more complex analyses of oscillating tandem cylinders [45, 57, 95] or heat transfer from tandem cylinders [61]. In the study reported here, a flowing soap film was used as a reduced-order experimental model in a step toward resolving this discrepancy between experimental and computational results. At $Re \approx 100$, flow patterns and Strouhal numbers in a tandem cylinder wake were monitored as a function of the dimensionless center-to-center cylinder spacing, $\ell = s/D$, for $1.3 \leq \ell \leq 6.6$. Chapter 5 illustrates the relationship between the longitudinal spacing and wake patterns in detail.

1.5 Flow-induced vibration of the downstream cylinder of a tandem pair

Flow-induced vibration of a bluff body due to the formation of a wake is an important problem in many fields of engineering. Flow-induced vibration determines the oscillation of the flexible pipes that transfer oil from the seabed to the surface of the ocean, for example [71]. In civil engineering, flow-induced vibration affects the design of bluff structures in wind such as bridges, chimneys and buildings [62]. Flow-induced vibration caused by vortices being shed from a bluff body is also a promising way to extract energy from geophysical flows [10]. FIV energy harvesting systems are especially suitable for slow flow speeds in the range 0.5-1.5m/s which cannot be efficiently harvested by traditional hydroelectric power technologies. When a pair of tandem cylinders is immersed in a flow, the downstream cylinder can be excited into wake-induced vibrations (WIV) due to the interaction with vortices coming from the upstream cylinder. It has been suggested by Assi *et al.* [3] that the WIV mechanism is sustained by unsteady vortex-structure interactions that input energy

into the system as the downstream cylinder oscillates across the upstream wake.

The existing investigations of FIV in the wake of a stationary upstream cylinder focus on the relationship between the normalized oscillation amplitude A^* and the reduced velocity λ^*. Many studies have found that the oscillation amplitude of the constrained transverse motion increases continuously with increasing reduced velocity [3, 13, 36]. However, the effect of the longitudinal spacing is rarely mentioned, especially for low Reynolds number. Bokaian & Geoola [13] did investigate the wake-induced vibration of two circular cylinder with longitudinal separations of 1.09, 1.5, 2, 2.5, 3, 4 and 5 diameters. Their experimental results show that the transverse vibration continually increases when increasing the longitudinal spacing for Reynolds number $600 - 6000$. Hover & Triantafyllou [36] studied the oscillation of a compliantly-mounted rigid cylinder, which was towed 4.75 diameters behind a stationary leading cylinder at $Re = 3 \times 10^4$. Wake-induced vibration response of the downstream cylinder at relatively large longitudinal separations (from 4.0 diameters to 20.0) was investigated by Assi *et al.* [3]. In their experiment, the smallest separation of 4.0 diameters presented the highest amplitudes of vibration, with increasing amplitude for higher reduced velocities, while the response for 20 diameters of separation was drastically reduced and more resembles that of VIV of a single cylinder.

The WIV response for small separation (< 4.0 diameters) at small Reynolds number ($Re < 200$) is seldom discussed in the existing literature. In contrast, the wake patterns of two stationary tandem cylinders have been studied systematically and comprehensively [93]. Zdravkovich [113] first introduced the wake pattern classification for two stationary tandem cylinders. The wake patterns depend on the Reynolds number and the center-to-center longitudinal spacing. As discussed in Section 1.4, the wakes can be divided into three basic types of wake interaction patterns: (i) a single bluff-body wake; (ii) shear layer reattachment at intermediate spacing, also referred to as the "reattachment regime"; and (iii) Karman vor-

tex shedding from each cylinder at larger spacing, also referred as the "co-shedding regime". The investigation of wake structures of two stationary tandem circular cylinders has close links with the flow-induced vibration of the downstream cylinder of a tandem pair. Inspired by the research of the two stationary tandem circular cylinders, several basic questions are addressed in this thesis: To what extent does the motion of the downstream cylinder affect the wake formed in the gap? What are the differences in wake structure between the two stationary tandem cylinders and flow-induced vibration of a tandem pair?

In a very small number of studies, researchers have investigated the effect of relatively small spacing on the oscillation of a downstream object. Jia investigated the response modes of a flexible filament in the wake of a cylinder in a flowing soap film [43]. A silk filament with 150 μm diameter and 6.2×10^{-10} Pa m^4 bending stiffness was set in the wake of the cylinder with its leading edge fastened to a cocoon silk fiber with $15\mu m$ diameter. Three response modes of the filament located in the wake of the cylinder were observed in the horizontal soap film tunnel. When the filament is close to the cylinder, the filament in the wake of the cylinder produces enough thrust to balance the drag without the support of the silk fiber (P mode). When the distance between the filament and the cylinder is large, the silk fiber becomes tight and the filament "slaloms" between the vortex cores shedding from the cylinder (S mode). In the third mode, the status of the silk fiber changes alternately between tight and loose. The filament flaps in the flowing soap film while rocking in the streamwise direction (R mode). The S mode is related to the wake-induced vibration but the R mode corresponds to the "galloping" response. However, the filament has much smaller transverse dimension than the cylinder so the downstream filament has no effect on the wake created by the upstream cylinder. Bandi studied the dynamics of a pendulum made of a rigid ring attached to an elastic filament immersed in a flowing soap film downstream from a fixed cylinder [5]. In this system, the string attaching the two cylinders was immersed in the flowing soap film, which

has a critical effect on the wakes of the two cylinders. It is valuable to fill in the knowledge gaps for wake-induced vibration in quasi-2D flow, which is addressed in Chapter 6. Qin *et al.* [81] carried out a systematic study of the cross-flow-induced vibration of a spring-supported circular cylinder with diameter D placed in the wake of a stationary cylinder having smaller diameter d. The diameter ratio d/D and the longitudinal separations s/d are varied from 0.2 to 1.0 and from 1.0 to 5.5, respectively. Their experimental results show no obvious vibration for the same diameter tandem cylinders ($d/D = 1.0$). The no-vibration phenomenon is caused by the large mass ratio ($m^* = m/m_f = 275$) in their experiments. Thus there is also a need to investigate the flow-induced vibration of two tandem cylinders for smaller mass ratio ($m^* = O(10)$), which is also addressed in Chapter 6.

The final part of the research work covered in this thesis uses a flowing soap film system, with behavior that resembles two-dimensional hydrodynamics, to experimentally investigate the wake interaction between a stationary upstream circular disk and a free downstream circular disk, which acts as a swinging pendulum. In these experiments, the upstream cylinder is fixed in place, while the downstream cylinder is free to oscillate like a pendulum that is driven by interactions with the flow, including the wake of the upstream cylinder. The support for the pendulum does interact with the soap film, in contrast to the system studied by Bandi *et al.* [5]. With the ability to tie together the wake structure and the object motion, the relationship between energy conversion and flow structure was investigated in the reduced order system for $Re \approx 150$. The research results also find several critical longitudinal spacings, which classify various wake patterns and oscillation modes. The study attempts to answer the following fundamental questions: Could the wake of upstream disk stimulate the vibration of the downstream disk in the flowing soap film? How stable is the motion of the downstream disk induced by wake interaction? To what extent does dimensionality affect vortex shedding and wake structure? How does the body motion influence flow topology during the vortex

formation process? Can the forces on the body in an exotic wake be predicted by the wake structure?

Chapter 2

Research Approach

2.1 Experimental setup

2.1.1 Soap film flow as a proxy for two-dimensional Navier–Stokes flow

The stability of the flowing soap film is due to the concentration of soap molecules on its surface, which leads necessarily to an elastic behavior in the film [19]. As the film thins locally, soap molecules are spread apart, causing the surface tension σ to increase locally, which in turn generates a restoring force aimed at returning the film to its original surface area S. This Marangoni effect gives rise to an elasticity $E_M = S(\mathrm{d}\sigma/\mathrm{d}S)$ for the film. The significance of these effects in the soap film flow are characterized by the elastic Mach number, $M_e = U_\infty/v_M$, where U_∞ is the film flow speed and $v_M = \sqrt{2E_M/(\rho\, h_\mathrm{f})}$ is the Marangoni wave speed, with ρ the fluid density and h_f the film thickness.

Auliel *et al.* [4] considered an asymptotic expansion of the soap film governing equations for moderate values of the elastic Mach number, $M_e = \mathcal{O}(10^{-1})$. Their analysis is an extension of the earlier analysis by [19] for $M_e \ll 1$, which is applicable for horizontal films with no background gravity-driven flow. Auliel *et al.* [4] show that the surfactant concentration Γ

plays the role of pressure, and an asymptotic analysis leads to the equations of motion [4]

$$\frac{D\boldsymbol{u}}{Dt} = -\boldsymbol{\nabla}\Gamma + \frac{1}{Re}\boldsymbol{\nabla}^2\boldsymbol{u} + \frac{1}{Fr^2}, \tag{2.1}$$

where $\boldsymbol{u}$ is the velocity field in the two-dimensional plane of the film and all derivatives are confined to this plane. Marangoni elasticity induces thickness variations η proportional to the surfactant concentration [19]:

$$\eta = \frac{1+K^*}{K^*}\Gamma, \tag{2.2}$$

where η is the thickness variations and K^* is the virtual thickness of the interface. Thus the instantaneous Marangoni elasticity causes the thickness variations in the soap proportional to the pressure field in two-dimensional flow.

Many studies have validated certain features of the flowing soap film as a reduced-order experimental model of flow at low Reynolds number. Wen & Lin [102]'s experimental results show that the Strouhal–Reynolds number curve of the flowing soap film at low Reynolds number ($Re < 180$) is in good agreement with 2D computational results. Wu *et al.* [106] investigated the separation angle of the flow around a circular cylinder in a flowing soap film for $Re < 280$. Their experimental data are in excellent agreement with their 2D numerical simulations. Other studies of the soap film are closely associated with this PhD research work and will be discussed in the following sections and chapters below [5, 43, 88, 107].

2.1.2 Soap film setup

The soap film tunnel is an excellent experimental platform for visualizing the two-dimensional wake of a bluff body. The experimental setup of the soap film has evolved over decades. Couder first used the soap film to investigate two-dimensional vortex streets and two-

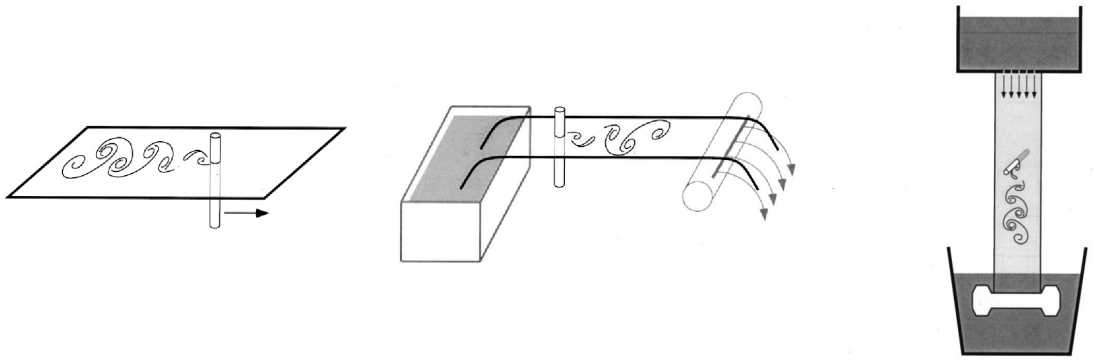

Figure 2.1: Three types of soap film setup: (a) An obstacle is dragged through a suspended horizontal stationary soap film [21, 22, 22]; (b) Suspended horizontal flowing soap film driven by a pulling mechanism [9, 29]; (c) Vertical flowing soap driven by grativty. (Figure from Rutgers *et al.* [86])

dimensional turbulence [21, 22, 22]. In these experiments, the bluff bodies were towed to produce wakes in a horizontal stationary soap film as shown in Figure 2.1(a). Gharib & Derango [29] developed a soap film setup where the film flows through a channel, similar to a tranditional water tunnel. The device includes one rectangle frame, one soap solution reservoir and a film-pulling mechanism. The motion of the soap film in the frame is driven by the contact action of a water jet as shown in Figure 2.1(b). Kellay *et al.* [49] modified the soap film device to a vertical flowing soap film driven by gravity. The soap film was formed between two parallel guide wires and the flow was perpetually supplied from the top soap solution reservior, as shown in Figure 2.1(c).

The soap film devices used for this PhD research are illustrated in Figure 2.2 and Figure 2.3. Some of work was conducted using a gravity-driven, vertically flowing soap film, as shown in Figure 2.2. The soap film, flowing from top to bottom, is developed between two parallel nylon guide wires (diameter 1 mm, spacing 10 cm). The nylon wires are tensioned by a spring and stretched by 4 horizontal pull lines (0.3 mm) to form a 10 cm by 1 m channel test section where the experiments are performed. The soap film has a 67 cm long triangular expansion

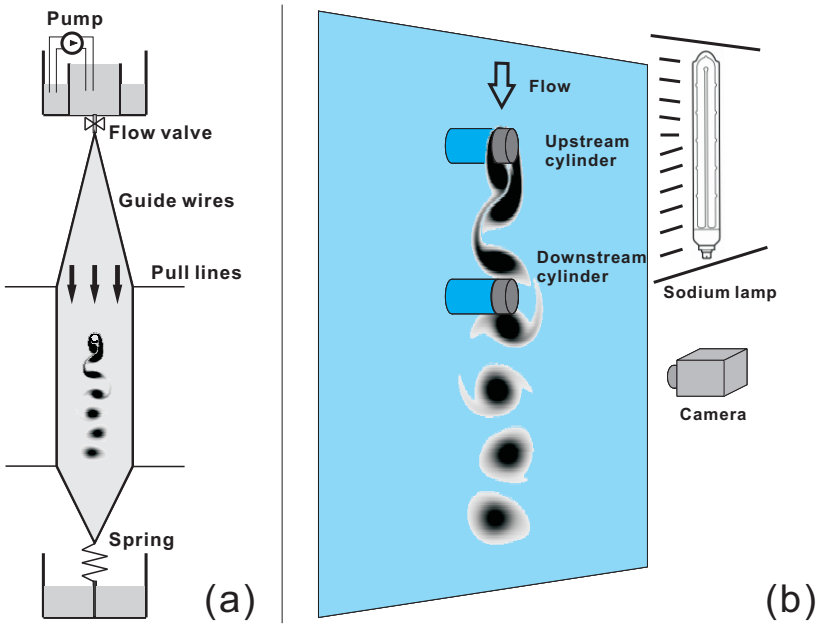

Figure 2.2: Schematic of the vertical soap film setup

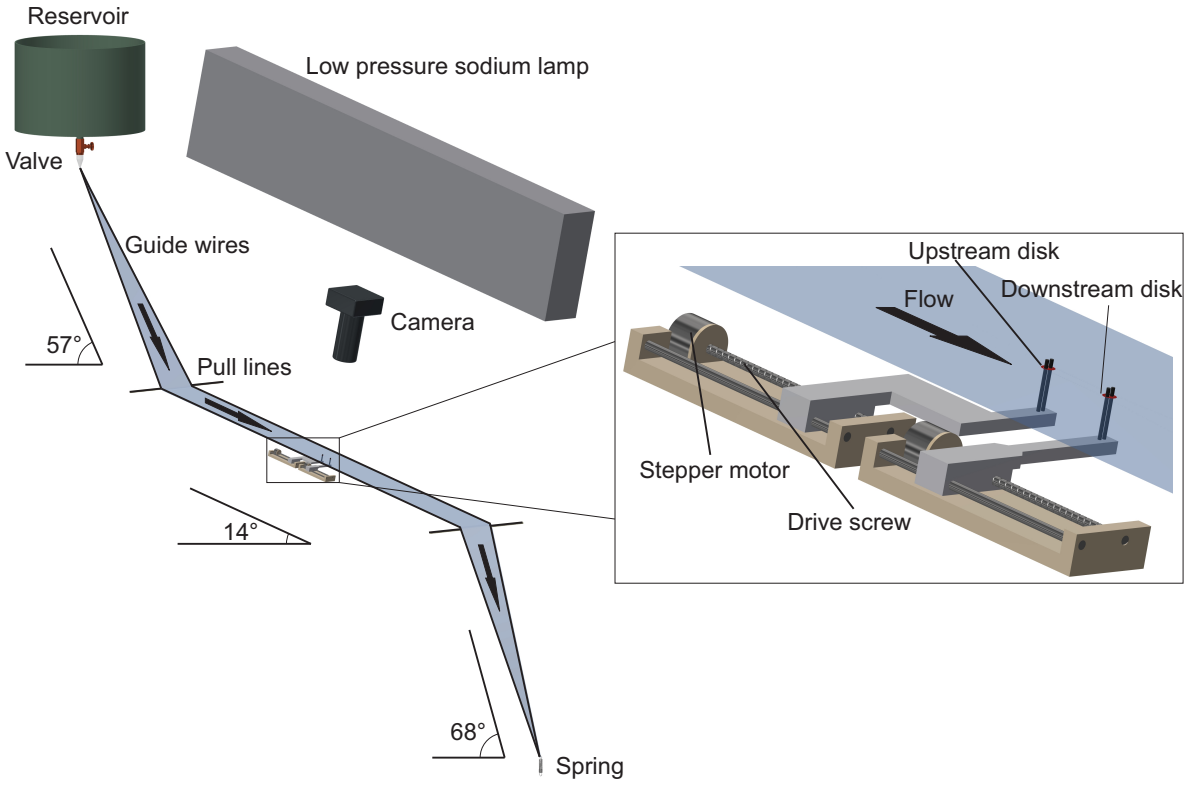

Figure 2.3: Schematic of the inclined soap film system.

section and a 43 cm long triangular contraction section. The soap solution for the soap film is $1-4\%$ Dawn $Escapes^{TM}$ dish soap in water. The differences in concentration were assigned to adjust the soap film thickness and Reynolds number. The solution is pumped to a top reservoir which has an overflow mechanism to maintain a constant pressure head at the valve so the average flow speed will be controllably stable. For experiments in this vertical film, the flow speed ranges from 1.5 m/s to 2.4 m/s. The one or two cylinders are penetrated perpendicularly through the flowing soap film.

Other experiments were conducted in an inclined soap film to enable lower flow speeds. A schematic of the gravity-driven inclined soap film system is shown in Figure 2.3. A valve at the outlet of the reservoir provides control of the volumetric flow rate. A soap film is developed between two nylon guide wires (with diameter 1 mm) that are tensioned at the bottom of the system by a spring. The guide wires are separated by four horizontal nylon pull lines (with diameter 0.3 mm) to form a 58 cm long triangular expansion section, a 10 cm wide by 1 m long rectangular test section, and a 56 cm long triangular contraction section. The expansion section is inclined 57° from the horizontal axis, the test section has a 14° inclination angle, and the contraction section has a 68° inclination angle. The flow speed ranges from 0.6 m/s to 1.2 m/s in the inclined system. The inclination angle of 14° in the test section was the minimum angle for which out-of-plane displacement of the film by gravity was fully obscured by the nylon guide wires when viewed from the side. In this configuration the curvature of the film surface is approximately $0.4\,\mathrm{m}^{-1}$, which we consider to be negligible.

The gravity-driven soap film system follows closely the designs of Jia & Yin [42, 43] and Wang *et al.* [98]. The overall dimension of the soap film systems is always 5-10 cm wide and over 2 m long [42, 86, 88, 98]. The large aspect ratio was designed to give small channel expansion angle and contraction angle. A large expansion angle would result in the separation of the center fluid jet from the channel walls, and then the flow would wander laterally in an

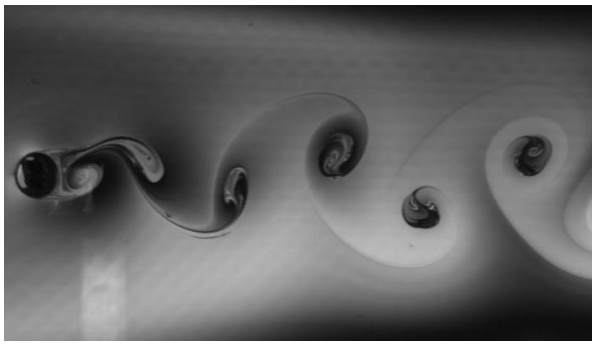

Figure 2.4: The interference fringes of the wake pattern for one circular cylinder. The circular disk is located at left side of the image. The soap film flows from left to right. The support mechanism appears as a light colored strip at lower left of image.

unstable fashion [86]. The diameters of the obstacles in the soap film were below 7 mm so the blockage ratios were smaller than 8% for all experiments. Therefore no blockage correction was used in any of the data analysis [3, 101].

2.1.3 Flow visualization

Flow visualization was the experimental method used to investigate the wake structures. Three low-pressure sodium lamps (wavelength 589 nm, Philips SOX 180W), which were wired to each phase of the alternating current power, were employed to illuminate the soap film. The phase delay gives an essentially constant power transfer to the illumination system. Therefore, the intensity of the monochromatic light does not vary significantly with the alternating electric current, giving a consistent illumination. The thickness of the film changes with the flow speed. Vortices are shed from the cylinder in the form of film thickness variations. Dark and bright fringes become visible on the film under the monochromatic light from the sodium lamps. A high-speed camera (Falcon 4M60, Teledyne DALSA) recorded the optical interference between the front and back surfaces of the film.

The actual frequency of the intensity's variation is $120Hz$ because of the light source, while

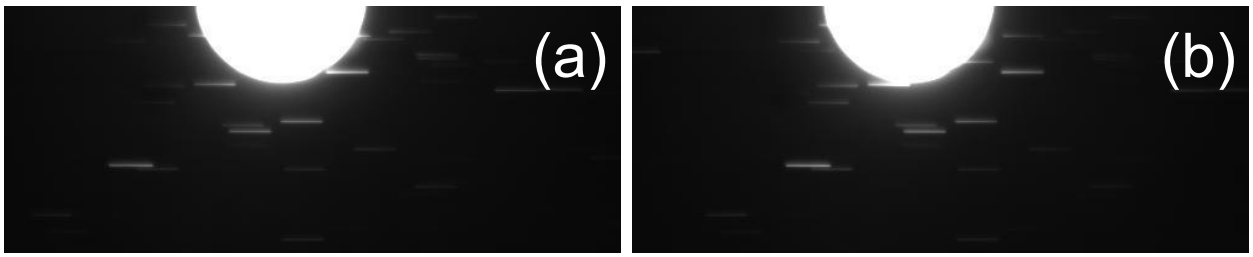

Figure 2.5: Trajectories of the seeding particles. Time interval between (a) and (b) is 1/300 second.

the vortex shedding frequency is below $80Hz$. The minimum framerate in the experiments is $170Hz$ and the resolution of the image under this framerate is $2352\times600\,\mathrm{px}^2$. The maximum framerate used in the experiments is $380Hz$ and the resolution of the image for this framerate is $2352\times260\,\mathrm{px}^2$. An example of a vortex wake in the system is shown in Figure 2.4. The exposure time during the experiments is $0.5-3$ millisecond.

2.1.4 Speed, thickness, viscosity, force and measurements

By tracking the trajectories of seeding particles, the distances they traveled downstream per unit time were measured to calculate the flow speed. That is, the speed measurement used here was a simplied particle tracking velocimetry (PTV) approach. One white light source (Elinchrom Modeling Lamp, EL23006) was placed behind the soap film, and the diffraction patterns of the seeding particles were visualized in the soap film and recorded by the high speed camera, as shown in Figure 2.5. Titanium oxide powder (diameter $0.2\mu m$) and hollow glass spheres (diameter $10\mu m$) were used as seeding tracers in the soap film. The results show that there is no difference in the calculated flow speed between the two types of seeding particles. PTV measurements were made at the end of each experimental test to avoid having seed particles interfere with the wake visualization.

By measuring the volumetric flow rate and the flow speed simultaneously, we estimated

the film thickness for the 10 cm wide test section. The film thickness was in the range of $h_{\mathrm{f}} = 2.25 - 3.37\,\mu$m for various speeds in the experiments. This range agrees with Rutgers *et al.* [86]'s thickness measurements. Wu *et al.* [107] developed an infrared technique for measuring the thickness of a flowing soap film. The technique is based on the absorbtion of infrared light by the water molecules in the film. Due to the complexity of the measurement, this technique has not been widely applied. However, Wu *et al.* [107]'s experimenal results show that the film thickness is basically uniform in the center area of the channel and decreases slightly near the guide wires [107]. Thus a laminar flowing soap film such as used in this PhD research is expected to have a reasonably uniform film thickness in the center of the channel. The mass of the soap film volume having the same cross-sectional area as one circular disk was calculated as

$$m_f = \frac{1}{4}\pi\rho {D_{\mathrm{d}}}^2 h_{\mathrm{d}}. \tag{2.3}$$

Thus the mass ratio between one circular disk and the soap film with same cross-sectional area is $m^* = m_D/m_f$.

Direct calculation of the Re value for a flowing soap film experiment is difficult owing to the challenges in determining an appropriate value for kinematic viscosity [85]. The effective viscosity μ_f for the soap film can be determined by [22]

$$\mu_f = \mu_b + 2\frac{\mu_S^s}{h_{\mathrm{f}}}, \tag{2.4}$$

where μ_b is the bulk viscosity of the soap solution, μ_S^s is the surface Poise of the two superficial layers and h_{f} is the thickness of the soap film. However, the thickness was only roughly estimated using the volumetric flow rate in the current experiments, so another method was applied to determine the effective viscosity. Gharib & Derango [29] proposed using the Strouhal number for flow past an isolated cylinder to estimate the Reynolds number in a soap

Flow parameters		Re		St	
D [mm]	U [m/s]	measured	predicted	measured	predicted
4.4	0.74		100.1	0.1667	
3.5	0.74	81	76.4	0.1521	0.1551
5.5	0.74	124	125.0	0.1774	0.1771

Table 2.1: St–Re relationships for the inclined soap film system. Predicted Re values were found using measured St values in the functional relationship (2.5) from Williamson & Brown [104]. The base case with $D = 4.4\,\text{mm}$ was used to estimate $\nu = 3.27 \times 10^{-5}\,\text{m}^2/\text{s}$, which was then used to calculate the measured Re values for $D = 3.5\,\text{mm}$ and $5.5\,\text{mm}$. Predicted St values were found using measured Re values in (2.5).

film. Wen & Lin [102] showed that the Strouhal–Reynolds number curve for a cylinder in a soap film is in good agreement with established results [103]. We used this same approach to determine the Reynolds number in our experiments. For each test run, St was measured for flow past an isolated cylinder. Using the St–Re relationship from [104],

$$St = 0.2731 - 1.1129\ \text{Re}^{-1/2} + 0.4821\ \text{Re}^{-1}, \tag{2.5}$$

each St value was then converted into a Reynolds number. Table 2.1 shows the difference in Strouhal number between the measured value from single cylinder experiments and the St-Re relationship introduced by Williamson and Brown [104]. The film viscosity was calculated based on the wake of a single cylinder in the flow for $Re = 100$. With the same value of film viscosity, the Stouhal number for the Reynolds number of $Re = 81$ and $Re = 124$ were compared between the measured value based on the vortex shedding frequency and the value calculated by the St-Re relationship, as shown in Table 2.1. Results show that the measured Strouhal number agrees well with the value calculated by the St-Re relationship, and the discrepancies are always within 2%.

For the research presented in Chapter 6, a micro-cantilever laser-mirror sensor system was used to measure the force induced on a downstream ring by the wake of an upstream cylinder,

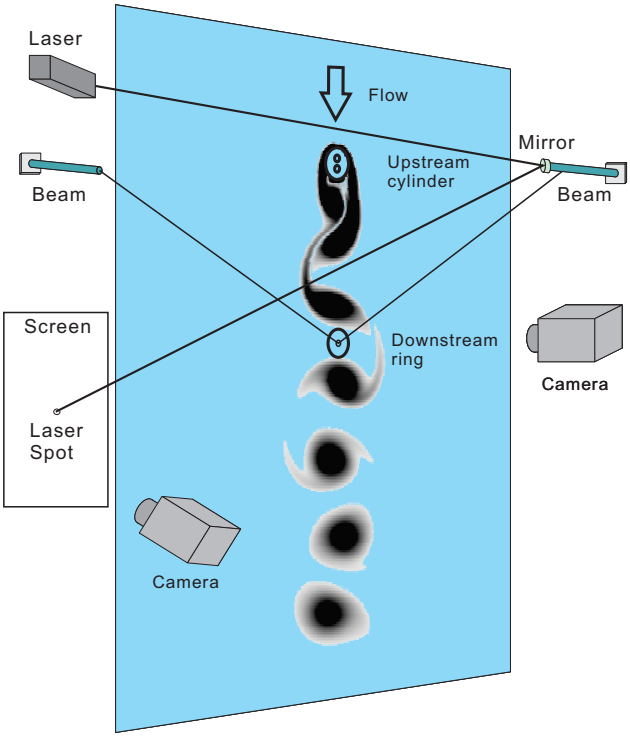

Figure 2.6: Schematic of force measurement

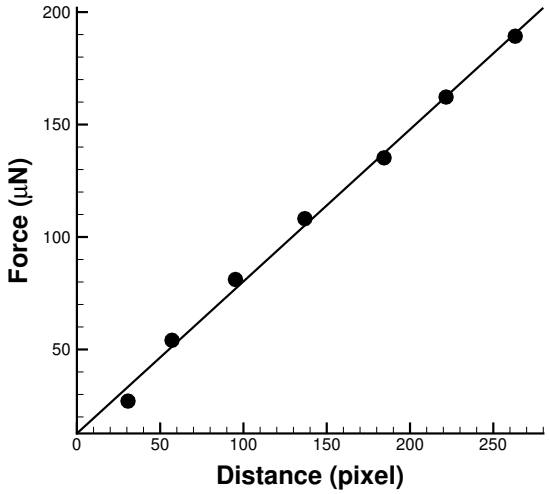

Figure 2.7: Calibration of force measurement

as shown in Figure 2.6. The force measurement system follows closely the design of Jia & Yin [43]. A thin fiber passed through the inner hole of the ring, and the ends of this fiber were connected to two cantilever beams. A millimeter mirror was adhered to the tip of one of the two beams. The millimeter mirror reflected an incident laser beam onto a screen. The location of the reflected laser beam spot correlates with the cantilever beam's bending, which is related to the force exerted on the beam. The horizontal component of the force comes from the lift of the downstream ring, and the vertical component is associated with the drag of the downstream ring. Two high speed cameras were synchronized to simultaneously record the transient wake and the trajectory of the laser spot. The force measurement was calibrated, and the results show that the methodology can attain a precision of 0.1 μN, the same as Jia & Yin [43]'s calibration results. The linear fitting of the calibration measurements is shown in Figure 2.7. The linear slope is $6.76\mu\text{N}/pixel$ with 99.6% confidence.

2.2 Numerical method

2.2.1 Lattice Boltzmann Method

A code based on the lattice Boltzmann method was implemented to simulate the two-dimensional flow around circular cylinders. This method has been widely applied to unsteady and multi-component flows [45, 54, 110]. The popular BGK model of the Boltzmann equation with the single relaxation time approximation was used for the numerical simulation [11]:

$$f_i(\mathbf{x} + e_i\Delta t, t + \Delta t) - f_i(\mathbf{x}, t) = -\frac{1}{\tau}[f_i(\mathbf{x}, t) - f_i^{eq}(\mathbf{x}, t)], \tag{2.6}$$

where Δt is the time step, τ is the relation time, and $f_i(x,t)$ and $f_i^{eq}(x,t)$ are the density distribution function and local equilibrium distribution function in ith direction of the phase space, respectively. The D2Q9 model was used here to simulate two-dimensional incompressible viscous flow. For this model, the velocity vector in phase space was discretized in nine directions:

$$\mathbf{e}_i = \begin{cases} (0,0), & i = 0, \\ c[cos(i-1)\pi/2, sin(i-1)\pi/2], & i = 1-4, \\ \sqrt{2}c[cos(2i-1)\pi/4, sin(2i-1)\pi/4], & i = 5-8, \end{cases} \tag{2.7}$$

where $c = \Delta x/\Delta t$ is the lattice speed and Δx is the lattice spacing. The equilibrium equation in Eq. 2.6 for the D2Q9 model is in the form of

$$f_i^{eq}(\mathbf{x},t) = \rho w_i \Big[1 + \frac{3}{c^2}\mathbf{e}_i \cdot \mathbf{u} + \frac{9}{2c^4}(\mathbf{e}_i \cdot \mathbf{u})^2 - \frac{3}{2c^2}\mathbf{u} \cdot \mathbf{u}\Big], \tag{2.8}$$

where the weighting factors w_i are:

$$w_i = \begin{cases} 4/9, & i = 0, \\ 1/9, & i = 1-4, \\ 1/36, & i = 5-8. \end{cases} \tag{2.9}$$

The macroscopic fluid density ρ and the momentum $\rho\mathbf{u}$ can be determined by:

$$\rho = \sum_{i=1} f_i \tag{2.10}$$

and

$$\rho \mathbf{u} = \sum_{i=1} f_i \mathbf{e}_i. \tag{2.11}$$

The sound speed in the mode is $c_s = c/\sqrt{3}$ and the fluid pressure p for the model is evaluated as:

$$p = \rho c_s^2. \tag{2.12}$$

The viscosity in the NS equation derived from Eq. 2.6 is

$$\nu = (\tau - 1/2) c_s^2 \Delta t. \tag{2.13}$$

For the standard Lattice Boltzmann method, the time step is equal to the space step so we have $\Delta x = \Delta y = \Delta t$. Thus the viscosity of the fluid becomes

$$\nu = (2\tau - 1) c \Delta x / 6. \tag{2.14}$$

A multi-block grid refinement method, which offers a way to satisfy different resolution requirements in the near wall region and in the far field, was adopted to improve numerical efficiency [27, 109]. The ratio of lattice spacings in the two-grid system was defined by

$$m = \Delta x_c / \Delta x_f, \tag{2.15}$$

where c refers to the coarse grid and f refers to the fine grid. With the purpose of keeping

a consistent viscosity for the overall flow field including different lattice sizes, the relation between the relaxation times, τ_c, on the coarse grid, and τ_f, on the fine grid, must meet the following requirement:

$$\tau_f = \frac{1}{2} + m(\tau_c - \frac{1}{2}). \tag{2.16}$$

In order to keep the variables and their derivatives continuous across an interface between two different grids, the probability density function of Eq. 2.8 in the neighboring grid blocks must obey the following rule:

$$f_i^{eq,c}(\mathbf{x}, t) = f_i^{eq,f}(\mathbf{x}, t). \tag{2.17}$$

Thus, the non-equilibrium part of the distribution function must satisfy:

$$(1 - \frac{1}{2\tau_c}) f_i^{neq,c}(\mathbf{x}, t) = (1 - \frac{1}{2\tau_f}) f_i^{neq,f}(\mathbf{x}, t), \tag{2.18}$$

or

$$f_i^{neq,c}(\mathbf{x}, t) = m\frac{\tau_c}{\tau_f} f_i^{neq,f}(\mathbf{x}, t). \tag{2.19}$$

Therefore, we obtain the relationship for the probability density function in the neighboring grid blocks as

$$f_i^c = f_i^{eq,f} + \frac{m\tau_c}{\tau_f}(f_i^f - f_i^{eq,f}), \tag{2.20}$$

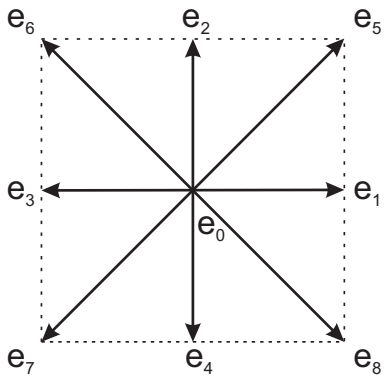

Figure 2.8: Discrete velocity vector for the D2Q9 lattice model

$$f_i^f = f_i^{eq,c} + \frac{\tau_f}{m\tau_c}(f_i^c - f_i^{eq,c}). \tag{2.21}$$

The numerical simulations in this work used the same lattice space ratio ($m = 2$) for all grid blocks and the mesh was refined 3 times from the far-field to the near wall region as shown in Table 2.2. The simulation used a rectangular computational domain with stream-wise dimension ($-107D$, $323D$) and transverse dimension ($-107D$, $107D$) with the upstream cylinder located at (0, 0). The grid was refined gradually from the far field and finally became finest for the inner-most block, which contains both the upstream cylinder and the downstream cylinder. The inner block had a size of $16D \times 8D$ and the upstream cylinder was located at $4D$ downstream of the block's upstream boundary, as shown in Figure 2.9. The initial condition was set as the incoming uniform flow U_∞ of the upstream far boundary. The side boundaries of the computational domain used the Neumann velocity boundary condition $\partial \boldsymbol{u}/\partial \boldsymbol{n}_F = 0$, where $\boldsymbol{n}_F$ indicates the unit vector in the boundary normal direction. The downstream far boundary condition was set as $\partial \boldsymbol{u}/\partial t + U_\infty \partial \boldsymbol{u}/\partial x = 0$. Bouzidi *et al.* [15]'s boundary treatment for a curved wall (i.e. a stationary cylinder) was applied in the simulations. This boundary condition satisfies the no-slip condition to second order.

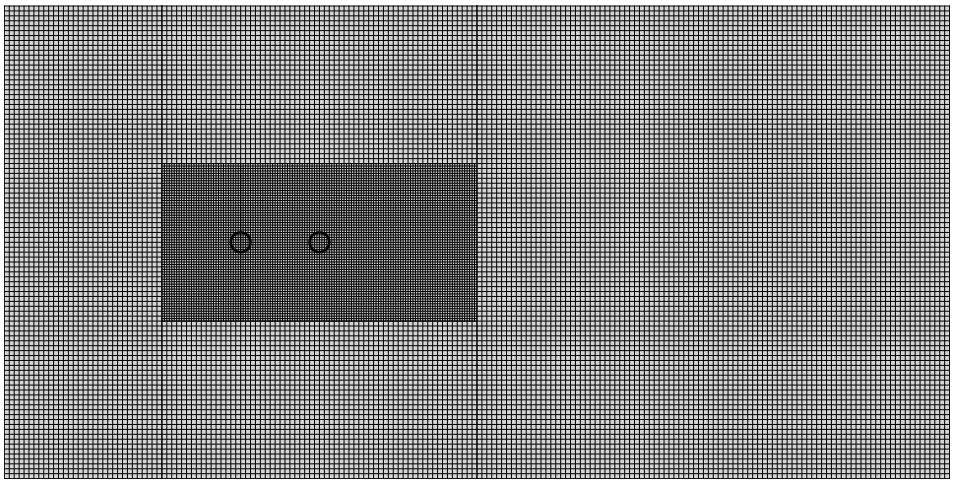

Figure 2.9: Schematic of grid refinement configuration: the grid is refined once between the outer block and inner block, and the lattice spacing ratio is 2. Mesh scheme is $D/\delta x = 8$ for the inner block

	Grid number	Computational domain
External block	$5,325,648$	$430D \times 214D$
First refinement block	$2,414,680$	$144D \times 72D$
Second refinement block	$1,097,848$	$48D \times 12D$
Third refinement block (innermost block)	$563,313$	$16D \times 8D$
Total	$9,401,489$	

Table 2.2: Grid number and computational domain

2.2.2 Numerical validation

First, we performed a grid-dependent verification by simulating the flow past two stationary tandem cylinders with a spacing $L/D = 6.0$ at a Reynolds number $Re = 100$ using different spatial resolutions. The mean drag coefficient $\bar{C}_D$, the root-mean-square drag coefficient $C_{D,rms}$, the root-mean-square lift coefficient $C_{L,rms}$, and the Strouhal number St of the downstream cylinder were computed as shown in Table 2.3. Four values of lattice densities ($D/\Delta x = 16$, $D/\Delta x = 32$, $D/\Delta x = 64$, $D/\Delta x = 128$) were chosen for the grid-dependent investigation. It is obvious that as the mesh is refined, the results tend to become grid-independent. The results show that a minimum mesh size of $\Delta x/D = 1/64$ is good enough for this simulation. Balanced by the computational efficiency, a $\Delta x/D = 1/64$ minimum mesh size was finally selected in the simulations.

	Downstream cylinder			St
	$\bar{C}_D$	$C_{D,rms}$	$C_{L,rms}$	
Mesh scheme 1 ($D/\Delta x = 16$)	0.5462	0.0560	0.8944	0.1477
Mesh scheme 2 ($D/\Delta x = 32$)	0.5447	0.0536	0.8846	0.1483
Mesh scheme 3 ($D/\Delta x = 64$)	0.5440	0.0533	0.8831	0.1489
Mesh scheme 4 ($D/\Delta x = 128$)	0.5441	0.0533	0.8830	0.1489

Table 2.3: Grid-dependent study for flow over two tandem cylinders ($L/D = 6$) at $Re = 100$

The accuracy of the algorithm was also validated by applying it to the flow past a stationary circular cylinder at a Reynolds number $Re = 100$. Table 2.4 summarizes the results of our current simulation and previous research on the mean drag coefficient $\bar{C}_D$, the root-mean-square drag coefficient $C_{D,rms}$, the root-mean-square lift coefficient $C_{L,rms}$, and the Strouhal number St. Results show that the current computed force coefficient and Strouhal number agree well with many previous simulations, and the discrepancies of the results between the

present simulations and the previous research are always within 5%.

	Force coefficient			St
	C_D	$C_{D,rms}$	$C_{L,rms}$	
Present	1.347	0.007	0.236	0.166
Park *et al.* [79]	1.33	–	0.235	0.165
Kravchenko [51]	1.32	–	0.222	0.164
Meneghini *et al.* [64]	1.37	–	–	0.165
Shi *et al.* [90]	1.318	–	0.222	0.164
Mittal [66]	1.322	–	0.226	0.164
Sharman *et al.* [89]	1.33	0.006	0.23	0.164
Stalberg *et al.* [92]	1.32	–	0.233	0.166
Posdziech & Grundmann [80]	1.325	–	0.228	0.164
Papaioannou *et al.* [78]	–	–	–	0.170
Li *et al.* [56]	1.336	–	0.228	0.164
Wang *et al.* [98]	1.48	–	–	–
Qu *et al.* [82]	1.319	–	0.225	0.165
Yuan *et al.* [110]	1.352	0.006	0.226	0.164

Table 2.4: Numerical values of St, $\bar{C}_D$, $C_{D,rms}$ and $C_{L,rms}$ for one single cylinder at $Re = 100$

Table 2.5 summarizes the results from flow past two tandem cylinders with various spacings for the current simulation and previous research. The mean drag coefficient $\bar{C}_D$, the root-mean-square drag coefficient $C_{D,rms}$, the root-mean-square lift coefficient $C_{L,rms}$, and the Strouhal number St of both the upstream cylinder and the downstream cylinder were determined to be as shown in Table 2.5 when the normalized spacing L/D ranges from 2.0 to 8.0. The results of Sharman *et al.* [89] and Didier [25] seem most consistent with the present study. The numerical method of Sharman *et al.* [89] and Didier [25] was the discretization of the 2D Navier–Stokes equations while the present simulation used the D2Q9 model of the Bhatnagar–Gross–Krook (BGK) scheme. Results show the current computed force coefficient and Strouhal number agree with the previous results using different numerical algorithms, and the discrepancies between the results of the present simulation and the previous research are always within 5%.

	Upstream cylinder			Downstream cylinder			St
	$\bar{C}_D$	$C_{D,rms}$	$C_{L,rms}$	$\bar{C}_D$	$C_{D,rms}$	$C_{L,rms}$	
$L/D = 2.0$							
Present	1.148	0.0000	0.003	-0.090	0.0000	0.013	0.120
Mizushima et al. (2005)[67]	1.196	–	0.024	-0.043	–	0.006	0.125
Sharman et al. (2005)[89]	1.168	0.0000	0.007	-0.088	0.0000	0.027	0.123
Didier et al. (2007)[25]	1.127	0.0003	0.005	-0.076	0.0000	0.021	0.130
Mussa et al. (2009)[72]	1.178	0.0011	0.008	-0.076	0.0018	0.041	0.124
Lin et al. (2013)[57]	–	–	–	–	–	–	0.128
Jiang et al. (2014)[45]	–	–	–	–	–	–	0.128
Tu et al. (2015)[95]	1.180	–	0.006	-0.075	–	0.022	0.122
Yuan et al. (2015)[110]	1.166	0.0000	0.003	-0.088	0.0000	0.011	0.120
$L/D = 3.0$							
Present	1.126	0.0001	0.009	-0.027	0.0013	0.079	0.111
Sharman et al. (2005)[89]	1.111	0.0014	0.023	-0.023	0.0084	0.182	0.110
Didier et al. (2007)[25]	1.104	0.0009	0.011	-0.022	0.0015	0.084	0.114
Papaioannou et al. (2008)[78]	1.16	–	–	0.05	–	–	0.116
Mussa et al. (2009)[72]	1.170	0.0025	0.065	0.078	0.0110	0.277	0.115
Wang et al. (2010)[98]	1.25	–	–	-0.06	–	–	–
Lin et al. (2013)[57]	–	–	–	–	–	–	0.117
Jiang et al. (2014)[45]	–	–	–	–	–	–	0.117
Tu et al. (2015)[95]	1.157	–	0.012	0.000	–	0.113	0.115
$L/D = 4.5$							
Present	1.259	0.0148	0.298	0.714	0.1238	1.034	0.151
Didier et al. (2007)[25]	1.261	0.0105	0.292	0.759	0.1290	1.060	0.151

Wang et al. (2010)[98]	1.41	–	–	0.91	–	–	–
Tu et al. (2015)[95]	–	–	0.308	–	–	1.088	–
$L/D = 8.0$							
Present	1.259	0.0084	0.242	0.569	0.0518	0.739	0.154
Sharman et al. (2005)[89]	1.300	0.0073	0.243	0.599	0.0507	0.777	0.160
Didier et al. (2007)[25]	1.249	0.0065	0.225	0.633	0.0507	0.797	0.158
Mussa et al. (2009)[72]	1.308	0.0062	0.256	0.631	0.053	0.805	0.158
Wang et al. (2010)[98]	1.42	–	–	0.74	–	–	–
Lin et al. (2013)[57]	–	–	–	–	–	–	0.163
Jiang et al. (2014)[45]	–	–	–	–	–	–	0.162
Tu et al. (2015)[95]	1.327	–	0.247	0.679	–	0.843	0.163

Table 2.5: Numerical values of St, $\bar{C}_D$, $C_{D,rms}$ and $C_{L,rms}$ for two tandem circular cylinders at $Re = 100$

2.3 Data analysis methodologies

2.3.1 Proper orthogonal decomposition

Proper orthogonal decomposition (POD), first used by Lumley [59, 60] to investigate coherent structures in turbulence, is a reduced order modeling technique based on eigenvalue transformations. The POD analysis in this PhD research work was conducted on the fluctuations of flow property $\boldsymbol{q}(\boldsymbol{x}, t)$, which is the mean field $\boldsymbol{Q}_{mean}(\boldsymbol{x})$ subtracted from the full field. The POD method works for various properties of the fluid, such as flow velocity, pressure, density, and temperature. The fluctuating flow property $\boldsymbol{q}(\boldsymbol{x}, t)$, as a function of space and time in N snapshots, is then reshaped to a matrix

$$\boldsymbol{Q} = [\boldsymbol{q}_1\ \boldsymbol{q}_2\ ...\ \boldsymbol{q}_N]. \tag{2.22}$$

The next step is to create the autocovariance matrix for $\boldsymbol{Q}$,

$$\boldsymbol{K} = \boldsymbol{Q}\boldsymbol{Q}^T, \tag{2.23}$$

where the T superscript means transpose of the matrix $\boldsymbol{Q}$. The matrix $\boldsymbol{K}$ is symmetric and positive and can be represented by an eigenvalue problem:

$$\boldsymbol{K}\boldsymbol{A}_i = \lambda_i \boldsymbol{A}_i, \tag{2.24}$$

where $\boldsymbol{A}_i$ are the eigenvectors and λ_j are the eigenvalues. The eigenvalues sort in descending order, with the first POD modes containing most of energy of the flow field. The eigenvectors give an eigenbasis for the POD modes,

$$\boldsymbol{\phi}_i = \frac{\sum_{n=1}^{N} A_{i,n}\boldsymbol{q}_n}{||\sum_{n=1}^{N} A_{i,n}\boldsymbol{q}_n||}, \tag{2.25}$$

where $A_{i,n}$ is the nth component of the the ith eigenvector of the POD modes. The projection of the fluctuation of the flow field onto the POD modes defines the time-dependent coefficients,

$$\boldsymbol{a}_n = \boldsymbol{\psi}^T \boldsymbol{q}_n, \tag{2.26}$$

where $\boldsymbol{\psi} = [\boldsymbol{\phi}_1\ \boldsymbol{\phi}_2\ ...\ \boldsymbol{\phi}_N]$.With the help of the POD repesentation, the spatial distribution of the flow field is decoupled from the time evolution. Thus the reconstructed flow field, which represents a reduced order model of a spatiotemporal variable function $\boldsymbol{q}(x,t)$, is determined

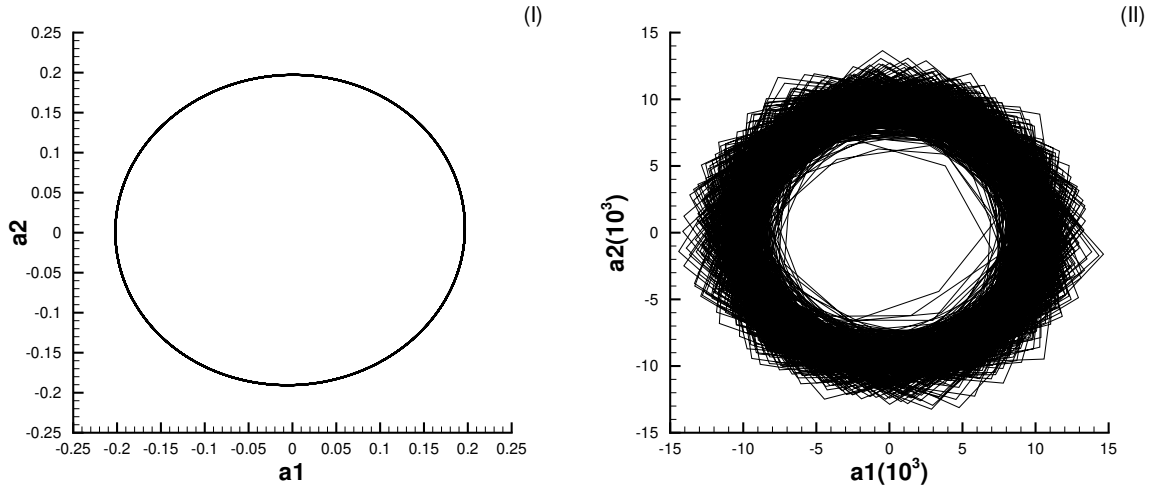

Figure 2.10: Orthogonality of POD analysis: (I) simulation for $Re = 100$; (II) experiment for $Re = 148$

by

$$\boldsymbol{q}(x,t) = \sum_{n=1}^{N} \boldsymbol{a}_n(t)\boldsymbol{\phi}_n(\boldsymbol{x}). \tag{2.27}$$

Figure 2.10 presents the orthogonality of the POD analysis. In Figure 2.10, the horizontal axis is the time-dependent coefficient of the first mode while the vertical axis is the time-dependent coefficient of the second mode. Figure 2.10(I) shows the results of the 2D simulation at $Re = 100$ and Figure 2.10(II) displays the results of the soap film experiment at $Re = 148$. The ideal a1-a2 curve should be elliptic, with a1 close to zero when a2 has maximum magnitude, and vice versa. The time-dependent coefficients of the 2D simulation in Figure 2.10(I) give an exact elliptic geometry. Limited by the framerate, the a1-a2 curve in Figure 2.10 for the experimental data shows a large random deviation, but the overall configuration is similar to an elliptic shape.

2.3.2 Machine learning

Mitchell [65] provided a widely quoted definition of machine learning: "A computer program is said to learn from experience E with respect to some class of tasks T and performance measure P if its performance at tasks in T, as measured by P, improves with experience E." One of the popular machine learning algorithms is the artificial neural network (ANN), which attempts to mimic a biological brain. The neural networks can "learn" to implement tasks without being programmed using detailed procedures. An ANN consists of connected units or nodes called artificial neurons. Each connection, similar to the brain synapses, can pass a signal from one artificial neuron to another. An artificial neuron that obtains a signal can process it and then inform additional artificial neurons connected to it. The learning process of ANN is an optimization procedure: minimization of the cost functions on a training set of examples. Cost functions show the discrepancy between the predictions of the model being trained and the actual problem instances. The training set is a set of examples used to fit the optimization parameters (e.g. weights of connections between neurons in ANN) of the model [84].

For Chapter 4, a neural network model was used to automate the wake classification by image recognition. Colvert *et al.* [20] used a neural network to classify vortex wakes using the vorticity field. In this PhD research work, the training examples came from the images of the high-speed flow visualization videos. Each training example was 188 pixel by 75 pixel gray-scale image (resized from 600 pixel by 1500 pixel). One floating point number normalized by 255 represented the gray-scale intensity at each pixel position. The 188×75 grid of pixels was then reshaped into a 14100-dimensional vector. The number of training examples was 14795 while the total frames of the high speed videos was 1183000. Therefore the training examples only contain 1.25% of the total frames. Each image vector constitutes a single row in a data matrix X so the dimension of the matrix X is 14795 by 14100.

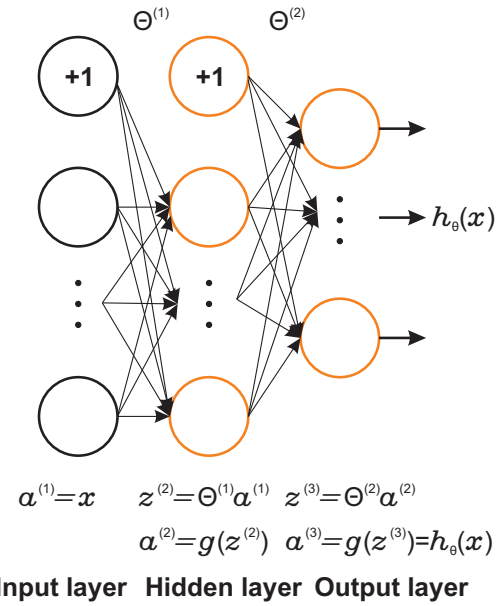

Figure 2.11: Neural network model.

Index	Wake pattern
1	2P wake
2	2S wake
3	Coalescing 2S wake
4	Perturbed von Karman wake
5	P+S model
6	Unsynchronized wake
7	Off-plane vibration

Table 2.6: Index of wake classification

Input layer	Hidden layer	Output layer
14100	300	7

Table 2.7: Neural network configuration

The other part of the training set is a 14795-dimensional vector y, which indexes labels for the training sets as shown in Table 2.6. Each neuron is a logistic unit in the learning process. The logistic operation was performed in three layers: input layer, hidden layer and output layer. In this learning process, the input layer has 14100 units, the hidden layer contains 300 units, and the output layer comprises 7 unit as shown in Table 2.7. For the input layer, the activation (input signal of neuron) $a^{(1)}$ is the intensity vector x. The mapping from the input layer to the hidden layer is:

$$z^{(2)} = \Theta^{(1)} a^{(1)},\ a^{(2)} = g(z^{(2)}), \tag{2.28}$$

where g is the sigmoid (logistic) activation function defined by:

$$g(z) = \frac{1}{1 + e^{-z}}. \tag{2.29}$$

$\Theta^{(j)}$ is the matrix of weights controlling function mapping from layer j to layer $j + 1$. The mapping between the hidden layer and the output layer is also based on the sigmoid activation function:

$$z^{(3)} = \Theta^{(2)} a^{(2)},\ a^{(3)} = g(z^{(3)}) = h_\theta(x). \tag{2.30}$$

The training process is to find $\Theta^{(1)}$ and $\Theta^{(2)}$ so that $h_\theta(x)$ is close to y (the index of the different wake patterns). The difference between $h_\theta(x)$ and y is described by the cost function

$J(\Theta)$. For the neural network, the cost function is defined as [30]:

$$J(\Theta) = -\frac{1}{m}\Big[\sum_{i=1}^{m}\sum_{k=1}^{K} y_k^{(i)} \log(h_\theta(x^i)_k) + (1 - y_k^{(i)}) \log(1 - h_\theta(x^i)_k)\Big] + \frac{\lambda}{2m}\sum_{l=1}^{L-1}\sum_{i=1}^{s_l}\sum_{j=1}^{s_l+1}(\theta_{ji}^{(l)})^2, \tag{2.31}$$

where m is the number of the training sample, L is the total number of layers in the network, s_l is the number of units in layer l, and K is the number of classes in the multi-class classification. For this wake classification process, we have three layers (L=3) and 7 different wake patterns ($K = 7$). The regularization parameter λ is used to avoid over-fitting. The test data set contains 4930 frames (0.42% of the total frames). Using the final $\Theta^{(1)}$ and $\Theta^{(2)}$ from the training process, the accuracy of the prediction for the test data set (distinct from the training set) is 95.72% for this image classifier. The image classifier was then used to predict the wake patterns for 845 runs (1400 frames per each run). For each run, we computed the "probability" that it belongs to each class using the trained neural network classifier. The prediction picked the class for which the corresponding neural network classifier output the highest probability and returned the class label (1, 2,..., 7) as the prediction for this run.

A Support Vector Machine (SVM) algorithm was used in Chapter 4 to find the boundaries between the different classes. The SVM is a maximum margin classifier, which determines the largest separations, or margins, between multiple classes. Figure 2.12 shows several possible boundaries: H1 does not separate the classes; H2 is a small margin classifier; and H3 is a large margin classifier. SVM is a maximum margin classifier as H3 in Figure 2.12. In addition to the linear classifier as shown in Figure 2.12, SVMs can efficiently conduct a non-linear classification using what is called the Gaussian kernel [83]. The Binary SVM offered by MATLAB is the SVM classifier used in this research. Figure 2.13 illustrates the non-linear decision boundary determined by the Gaussian kernel SVM for a repesentative example problem.

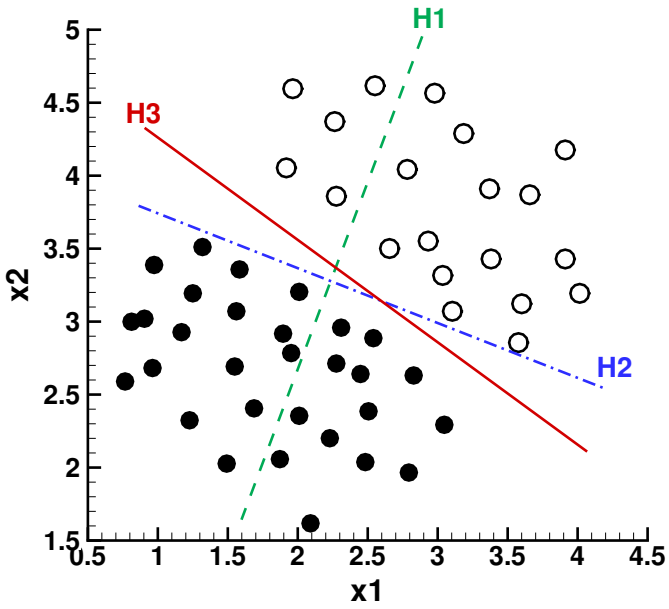

Figure 2.12: Boundaries of various classifier: H1 does not separate the classes; H2 is a small margin classifier; and $H3$ is a large margin classifier.

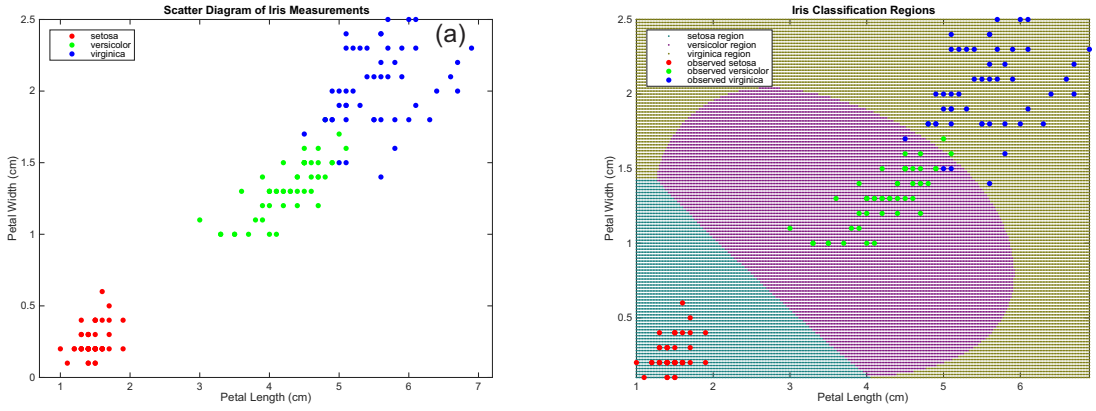

Figure 2.13: Multiple Class Boundaries determined by binary SVM: (a) a scatter plot of the original data; (b) Color in the regions of the plot based on the class to which the corresponding new observation belongs. (Figure from MATLAB support documentation)

Chapter 3

Vortex formation of a stationary circular cylinder

In this chapter, a new definition of vortex formation length based on POD analysis for steady flow past a stationary circular cylinder is introduced. As described in Section 1.2, the exact connection between the existing definitions of formation length of a single cylinder (like a mean recirculation region in the wake or the position of maximum velocity fluctuation on the wake centerline) and the critical spacing of two tandem cylinders has not been determined. Thus it is necessary to introduce a new definition that associates closely with the critical spacing of two tandem cylinders. POD analysis was conducted on both the 2D simulation results and the soap film experimental results. The first several POD modes take up the majority of the energy of the wake structures, so a reduced order model consisting of several POD modes is capable of predicting the spatial distribution and time evolution of the vortex shedding and propogation. In this application of POD analysis, the variable $q(\boldsymbol{x}, t)$ is the intensity distribution $I(\boldsymbol{x}, t)$ in the images of the soap film experiment. In contrast, the variable in the POD analysis of the 2D simulation results is the pressure field $p(\boldsymbol{x}, t)$ and the stream-wise velocity $u(\boldsymbol{x}, t)$. The intereference fringes on the soap film are directly related to the thickness variation, which is proportional to the local pressure in our soap film. So the pressure field in the 2D simulation is best suited for comparison with the soap film flow visualization results. The POD analysis is performed using MATLAB with double precision

as described in Chapter 2. POD reconstruction of the pressure field was then used to show the difference between this reduced order model and the unsteady pressure field.

3.1 Unsteady vortex formation length based on POD analysis

3.1.1 POD analysis of 2D simulation

The wake of one circular cylinder was simulated by the lattice Boltzmann method described in Section 2.2. The 2D code was initially developed by Li & Lu [54], upgraded to three-dimensional flow and used to simulate the wake pattern of a three-dimensional flapping plate [54]. The LBM method has been widely applied to unsteady and multi-component flows [45, 54, 110]. As described in Section 2.2, the D2Q9 model was used to simulate two-dimensional incompressible viscous flow. Bouzidi et al's boundary treatments for a curved wall was applied in the simulation [15]. This boundary condition satisfies the no-slip condition to second order. A multi-block method, which offers a way to satisfy a different resolution requirement in the near wall region and the far field, was adopted to improve the numerical efficiency [27, 109]. The Reynolds numbers for the simulations in this chapter range from 60 to 300.

The existing definitions of the "vortex formation length" were also investigated for the two-dimensional simulation. Figure 1.1(a) shows the mean recirculation region defined by the streamlines of the mean velocity field. The formation length based on this definition is approximately $L_r/D = 1.9$ for $Re = 100$ in the present simulations, which agrees with Papaioannou *et al.* [78]'s two-dimensional simulation. The velocity fluctuation with changing stream-wise location is illustrated in Figure 1.1(b). The maximum fluctuation of the stream-

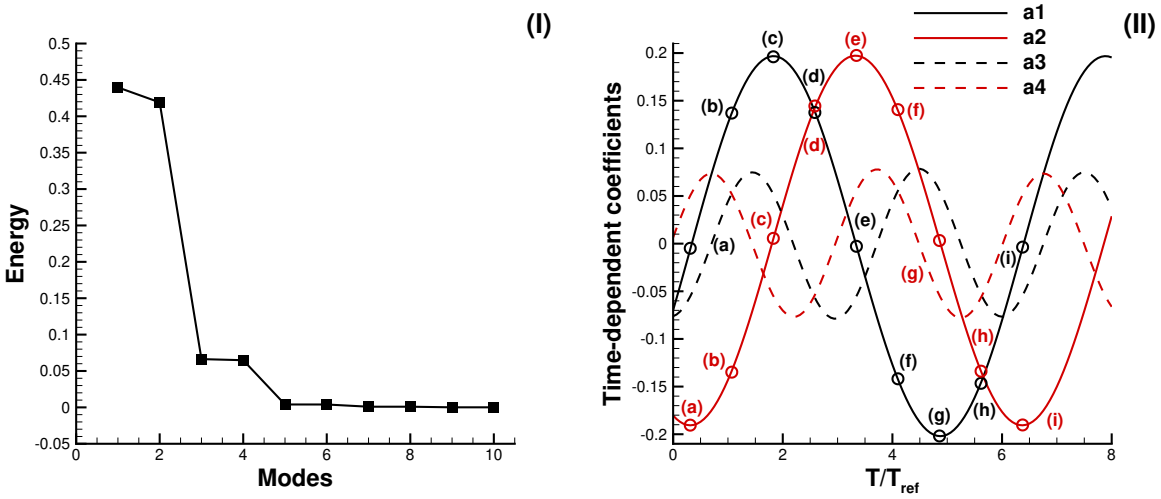

Figure 3.1: POD coefficients of the unsteady pressure field for $Re = 100$: (I) POD energy for each mode; (II) The first four time-dependent coefficients

wise velocity is located at $L/D = 2.83$ for $Re = 100$. Therefore the vortex formation length corresponding to the maximum velocity fluctuation L_f/D is 2.83 for $Re = 100$ in the present simulations. Table 3.1 summarizes the vortex formation length behind a single cylinder based on various definitions for $60 \leq Re \leq 300$. The vortex formation length for high Reynolds number is always smaller than that for low Reynolds number no matter what definition is used for the formation length.

The fluctuating part of the pressure field was used in the POD analysis. Figure 3.1(I) shows the POD mode energies of the 2D simulation for $Re = 100$. The first two modes take up 86% of the total energy and the first four modes occupy 99% of the total energy. The time-dependent coefficients of the first four modes ($a1 - a4$) are plotted in Figure 3.1(II). The amplitudes for the time-dependent coefficients of the first two modes $(a1, a2)$ are around 0.2 while the amplitudes for the time-dependent coefficients of the third and fourth modes $(a3, a4)$ are less than 0.08. The fluctuating frequency of $a1$ and $a2$ is the same as the vortex shedding frequency, and the frequency of $a3$ and $a4$ is twice that of the vortex shedding frequency. The phase difference between the four modes are clear in Figure 3.1(II) because

Re	L_r/D	L_f/D	$L_{\mathrm{p,max}}/D$	$L_{\mathrm{p,min}}/D$	$L_{\mathrm{u,max}}/D$	$L_{\mathrm{u,min}}/D$
60	2.58	5.30	4.30	3.22	4.40	3.02
80	2.15	3.55	3.97	3.00	3.38	2.09
100	1.90	2.83	3.38	2.47	3.15	2.05
150	1.53	1.69	3.22	2.35	3.18	2.38
230	1.25	1.23	2.60	1.98	2.92	2.20
300	1.24	1.09	2.59	1.92	2.60	2.05

Table 3.1: Vortex formation length based on 2D simulation: L_r/D is the vortex formation length based on mean recirculation region, L_f/D is the formation length defined by the position of maximum velocity fluctuation on the wake centreline, $L_{\mathrm{p,max}}/D$ is the maximum formation length based on POD analysis of pressure field, $L_{\mathrm{p,min}}/D$ is minimum formation length based on POD analysis of pressure field, $L_{\mathrm{u,max}}/D$ is the maximum vortex formation length based on POD analysis of stream-wise velocity, and $L_{\mathrm{u,min}}/D$ is the minimum vortex formation length based on POD analysis of stream-wise velocity

of the orthogonal decomposition.

The first four modes of the fluctuating pressure field are shown in Figure 3.2. The POD modes are shown for a spatial domain $(0.5D, 12D) \times (-2D, 2D)$. Two different regions are easy to recognize from the mode plot: the vortex formation region (having a strong pressure variation over a short distance) and the vortex street region (having a regular distribution of vortices of approximately the same magnitude). The zero contour lines of the pressure field shown as dark dash-dot lines in Figure 3.2(a) and (b) help define the boundaries between the two regions. The horizontal coordinates of the intersections between the zero contour lines and the centerline were labeled by blue long-dash lines in Figure 3.2(a) and (b). From the POD mode plots, the vortex formation length is determined by the distance between the center of the circular cylinder and the blue long-dash lines in Figure 3.2. According to this definition, the vortex formation length from mode 1 is around $3.38D$ while the vortex formation length from mode 2 is around $2.47D$. The maximum vortex formation length of a single cylinder, based on POD mode 1 at $Re = 100$, is $3.38D$; after adding the cylinder radius, this POD value is quite close to the critical spacing for two tandem cylinders (i.e., $(L/D)_c \approx 4$) during the increasing spacing scenario (which will be discussed in Chapter 5).

Similarly, the minimum vortex formation length based on mode 2 is $2.47D$; after adding the cylinder radius, this POD value is quite close to the critical spacing for two tandem cylinders (i.e., $(L/D)_c \approx 3$) during the decreasing spacing scenario (will also be discussed later in Chapter 5). In this approach, POD mode 1 defines a maximum vortex formation length and POD mode 2 defines a minimal vortex formation length.

The POD analysis of the steam-wise velocity is illustrated in Figure 3.3. The POD plots of the steam-wise velocity also show two vortex formations corresponding to mode 1 and mode 2, respectively. The maximum vortex formaton length determined by the POD analysis of the u velocity is $3.15D$ and minimum vortex formaton length determined by the POD analysis of the u velocity is $2.05D$. Both of these two formation lengths are smaller than those determined by the pressure field.

The POD analysis was also conducted for $Re = 150$. In this case, the maximum vortex formation length $L_{\mathrm{p,max}}$ is $3.22D$ and the minimum vortex formation length $L_{\mathrm{p,min}}$ is $2.35D$. It appears that the vortex formation length decreases with an increase of Reynolds number. Table 3.1 and Figure 3.4 summarizes the vortex formation length from the POD analysis with the change of Reynolds number. The vortex formation lengths from the pressure field agree with those from the stream-wise velocity in the cases $Re = 60$, $Re = 150$, and $Re = 300$. However, the differences become larger for other cases such as $Re = 80$ and $Re = 100$. The vortex formation length determined by the pressure field decreases monotonously with an increase of Reynolds number similar to the definition based on the mean recirculation region and the definition based on maximum velocity fluctuation. Thus it is more reasonable to use the POD analysis of pressure field to determine the vortex formation length instead of the POD analysis conducted on the stream-wise velocity.

The POD reconstruction helps provide a physical understanding of an unsteady vortex formation length. Figure 3.5 shows nine snapshots of the reconstructed pressure field and the

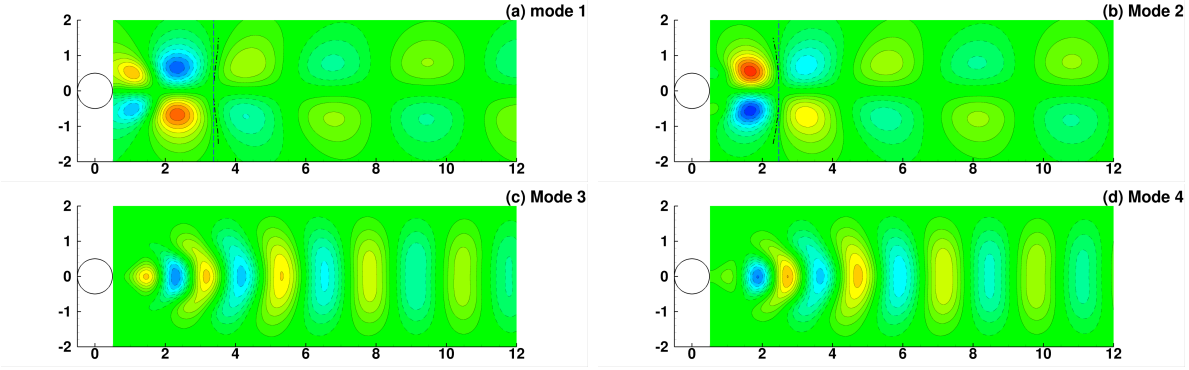

Figure 3.2: First four modes of the pressure field:(a)mode 1; (b) mode 2; (c) mode 3 and (4) mode 4 ($Re = 100$)

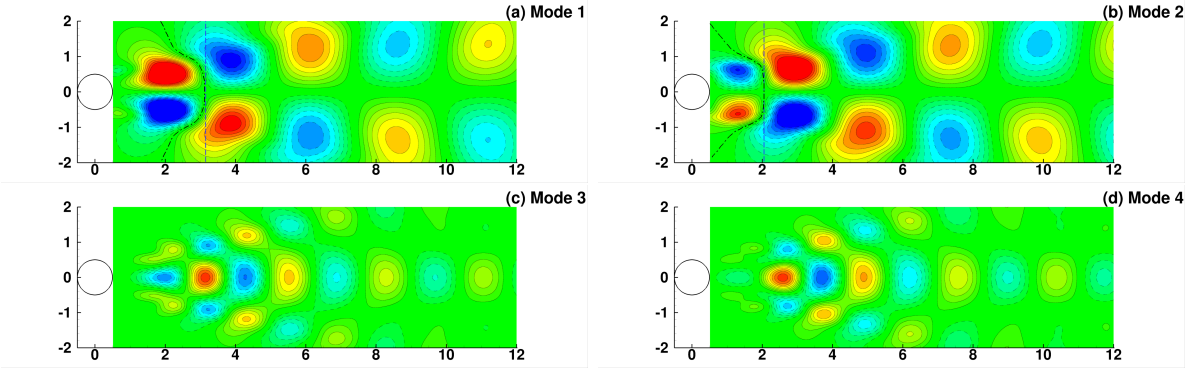

Figure 3.3: First four modes of the stream-wise velocity field:(a)mode 1; (b) mode 2; (c) mode 3 and (4) mode 4 ($Re = 100$)

Reconstruction (Mode 1 + Mode 2)	
(a) $T/T_{ref} = 0.3125$	$L/D = 2.4$
(b) $T/T_{ref} = 1.0703$	$L/D = 2.92$
(c) $T/T_{ref} = 1.8281$	$L/D = 3.43$
(d) $T/T_{ref} = 2.5859$	$L/D = 3.93$
(e) $T/T_{ref} = 3.3438$	$L/D = 2.41$
(f) $T/T_{ref} = 4.1016$	$L/D = 2.93$
(g) $T/T_{ref} = 4.8594$	$L/D = 3.41$
(h) $T/T_{ref} = 5.6172$	$L/D = 3.90$
(i) $T/T_{ref} = 6.3750$	$L/D = 2.41$

Table 3.2: Reconstructed vortex formation length based on POD modes of 2D simulation for $Re = 100$

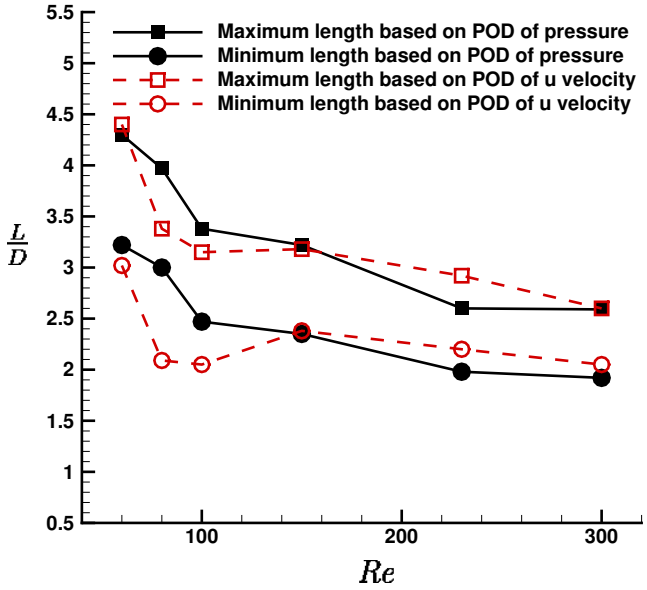

Figure 3.4: Vortex formation length determined by POD analysis as the change of Reynolds number.

original unsteady pressure field. The nine snapshots (a)-(i) of the time-dependent coefficients are labeled in Figure 3.1(II). The first column in Figure 3.5 is the reconstruction of mode 1 and 2, the second column is the reconstruction of the first four modes, and the third column is the mean pressure field subtracted from the original pressure field. The reconstruction of the first two modes is close to the unsteady pressure field while the reconstruction of the first four modes is almost as same as the unsteady pressure distribution. The vortex formation lengths determined from Figure 3.5 are listed in Table 3.2. The vortex formation length is smallest ($2.4D$) when the time-dependent coefficient $a2$ has the largest negative value and the time-dependent coefficient $a1$ is close to zero at point (a) in Figure 3.1(II). Then the vortex formation length increases as the wake evolves over time to point (e). The time-dependent coefficient $a1$ has the largest positive value and the time-dependent coefficient $a2$ is close to zero at point (e). Therefore the vortex formation length is about $3.4D$ at point(d). The vortex formation length continues to increase between point (c) and point (d) and attains

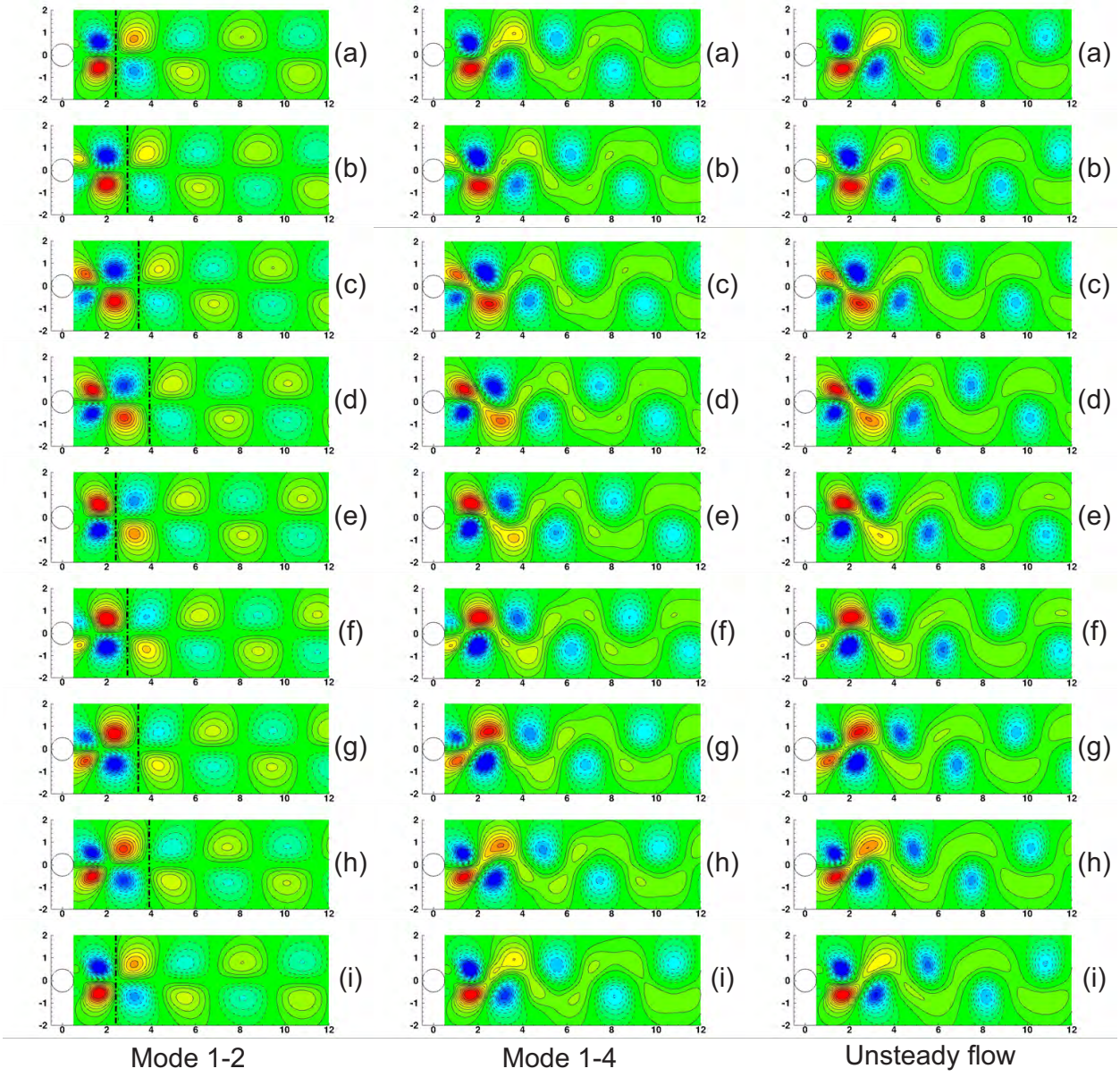

Figure 3.5: Reconstruction of the pressure field

Re	$L_{\mathrm{I,max}}/D$	$L_{\mathrm{I,min}}/D$
100 ± 10	3.34 ± 0.27	2.41 ± 0.20
148 ± 15	3.26 ± 0.05	2.22 ± 0.04

Table 3.3: Vortex formation length based on soap film experiment

its maximum value ($3.9D$) at point (d). The vortex formation length then decreases to the minimum value from point (d) to point (e). The vortex formation returns back to $2.4D$ at point (e) because the time-dependent coefficient $a2$ has the largest positive value and the time-dependent coefficient $a1$ is near zero. The vortex formation length repeats the same cycle when the wake evolves from (e) to (i).

3.1.2 POD analysis of soap film experiment

The wake of the single cylinder for $Re = 100$ was visualized using the inclined soap film setup, while the vortex patterns of the single cylinder for $Re = 150$ were generated using the vertical soap film setup. The fluctuating part of the intensity field was used for the POD analysis. Figure 3.6(I) shows the POD mode energies of the soap film flow for $Re = 100$. The first five modes take up 65.68% of the total energy. The time-dependent coefficients of the first five modes ($a1 - a5$) are plotted in Figure 3.6(II). The amplitude for the time-dependent coefficients of the first mode ($a1$) is larger than the amplitudes for the time-dependent coefficients of the second and third modes ($a2, a3$). However, there is a low frequency component in the time-dependent coefficient of the first mode. The high frequency components of the time-dependent coefficients for the first three mode ($a_1 - a_3$) are close to the vortex shedding frequency. It is speculated that the low frequency component is caused by off-plane vibration of the soap film. Thus this first mode, while containing much of the "energy" of the intensity variation, is not related to vortex shedding.

The first five modes of the intensity field for $Re = 100$ are shown in Figure 3.7. The first

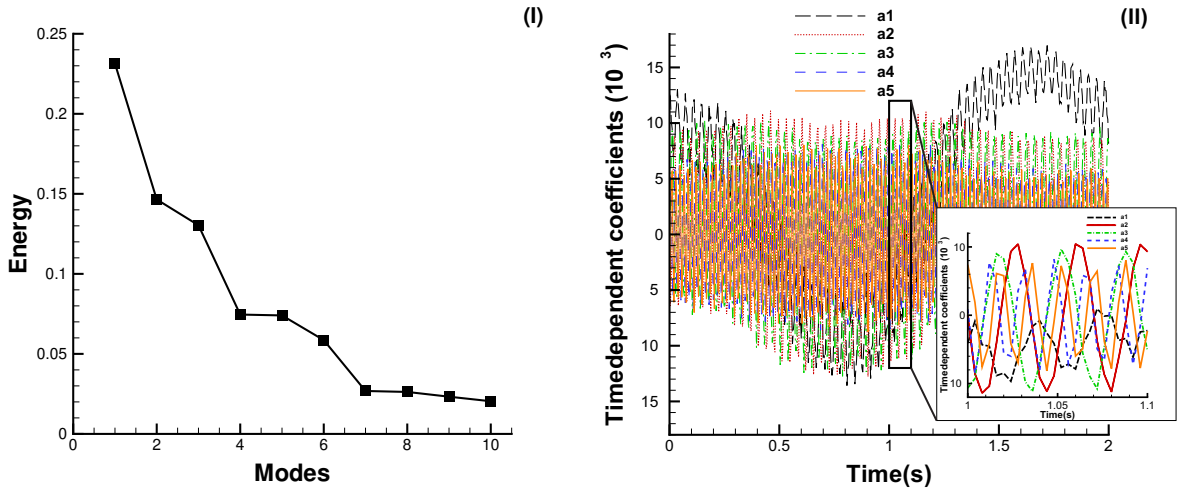

Figure 3.6: POD coefficients of the unsteady intensity field for $Re = 100$: (I) POD energy for each mode; (II) the first five time-dependent coefficients.

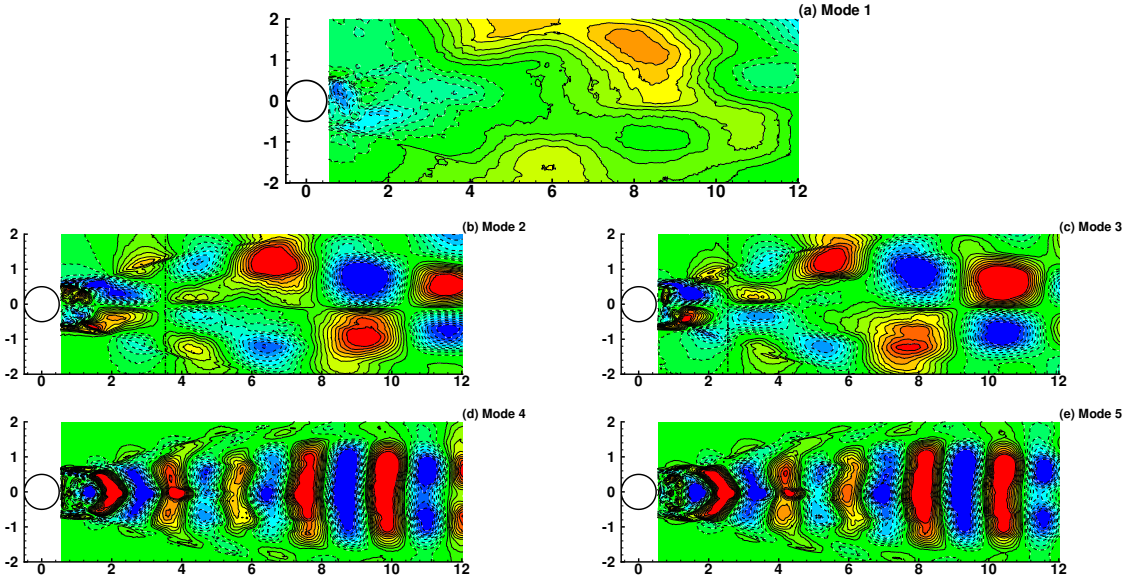

Figure 3.7: First five modes of the intensity field for $Re = 100$: (a) mode 1; (b) mode 2; (c) mode 3; (d) mode 4 and (e) mode 5.

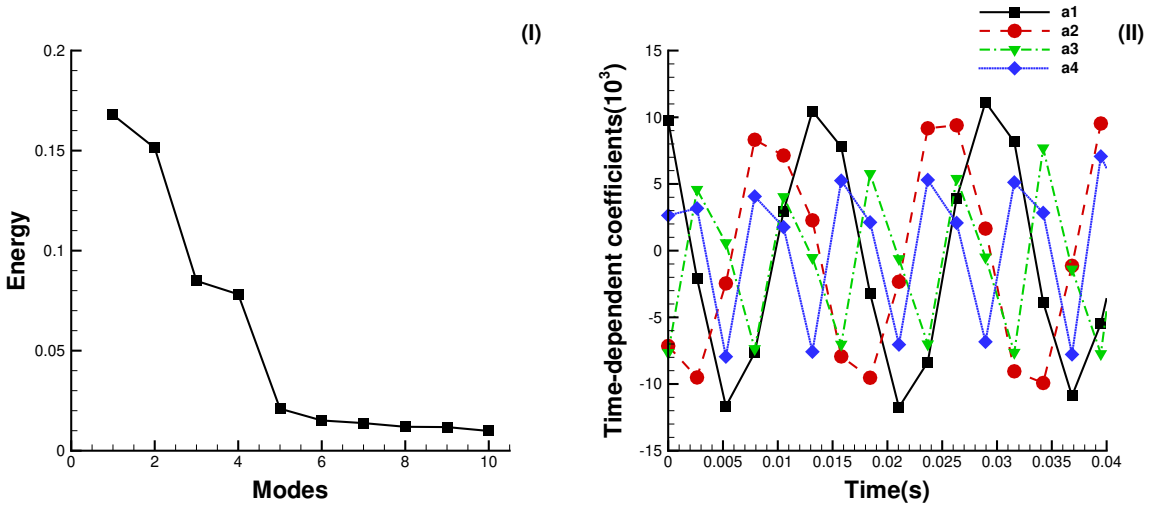

Figure 3.8: POD coefficients of the unsteady intensity field for $Re = 148$: (I) POD energy for each mode; (II) the first four time-dependent coefficients.

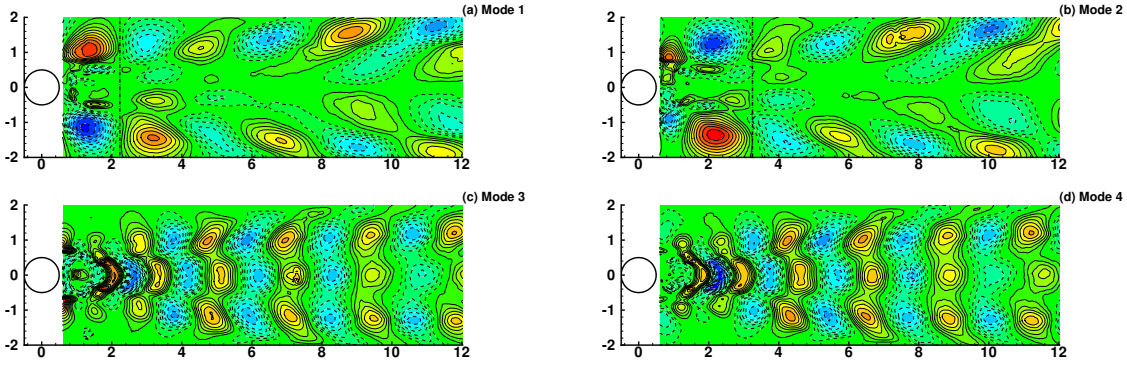

Figure 3.9: First four modes of the intensity field for $Re = 148$: (a) mode 1; (b) mode 2; (c) mode 3 and (d) mode 4.

mode shows no vortex shedding regimes but contains a variation from the center to the edge. This again supports the interpretation of mode 1 as showing the off-plane vibration in the inclined soap film system. For mode 2 and mode 3, the mode plots show the classic vortex street. The zero contour line of the intensity field again helps define the boundary between the vortex formation region and the vortex street. Again, the vortex formation length is determined by the distance between the center of the circular cylinder and the dot-dashed lines highlighting this zero-pressure contour as shown in Figure 3.7. According to this definition, from the experiment the dimensionless vortex formation length for mode 2 is 3.34 ± 0.27 while the vortex formation length for mode 3 is 2.41 ± 0.20. Thus we can define the maximum vortex formation length to be $L_{\mathrm{I,max}}/D = 3.34 \pm 0.27$ and the minimum vortex formation length to be $L_{\mathrm{I,min}}/D = 2.41 \pm 0.20$ in the soap film experiment. Both of these values are close to the results of the 2D simulation. Mode 4 and mode 5 of the experimental "pressure" field, shown in Figure 3.7, appears similar to mode 3 and mode 4 of the computational pressure field, shown in Figure 3.2. The frequency of mode 4 and mode 5 is also twice the frequency of mode 2 and mode 3 for the soap film experiment, as shown in Figure 3.6(II). Except for mode 1, the results of the POD analysis of the soap film experiment are close to the POD analysis of the two-dimensional simulation.

The POD analysis was also conducted on the soap film experiment for $Re = 148$. The soap film experiment for $Re = 148$ was conducted using the vertical soap film, so the off-plane vibration is much smaller compared to that of the incline soap film. Therefore no POD mode shows obvious off-plane vibration. Figure 3.8 shows the POD energies and time-dependent coefficients for $Re = 148$. The first four modes take up 48.22% of the total energy. Figure 3.8(II) shows the time-dependent coefficients of the first four modes. Due to the limitation of the framerate, the variations of the time-dependent coefficients are not smooth, but the approximate harmonic changes are obvious in Figure 3.8(II). The frequency of Mode 3

and Mode 4 are also twice as that of Mode 1 and Mode 2 in Figure 3.8(II). The first four POD modes for $Re = 148$ are presented in Figure 3.9. The first mode indicates that the minimum vortex formation length is around 2.22 while the second mode finds the maximum vortex formation length to be around 3.26. Table 3.3 summarizes the vortex formation lengths of the soap film experiments for various Reynolds numbers. Higher Reynolds numbers result in a smaller vortex formation length. This trend agrees with most existing definitions of vortex formation length [34, 44, 73, 78, 96].

3.2 Conclusions

In this chapter, the unsteady vortex formation lengths are defined using the zero contours of the fluctuating pressure field, which are identified using proper orthogonal decomposition (POD) for both the two-dimensional simulation and the (quasi-)two-dimensional experiment. This interpretation of vortex formation length could help with understanding of the vortex formation process and wake interaction between multiple bluff bodies. The POD mode plots identify two formation lengths: the maximum vortex formation length and the minimum vortex formation. The former length is related to the maximum critical spacing of two tandem circular cylinders, while the latter length is related to the minimum critical spacing, as described in Chapter 5. Figure 3.10 summaries the vortex formation length and critical spacing as the Reynolds number changes. The results of the vortex formation length as determined by the mean recirculation region in the current LBM simulations agree well with Papaioannou *et al.* [78]'s simulation results. The vortex formation length based on the location of maximum velocity fluctuation gradually approaches the formation length determined by the mean recirculation region with an increase of Reynolds number. The difference between the maximum vortex formation length of a single cylinder and the critical

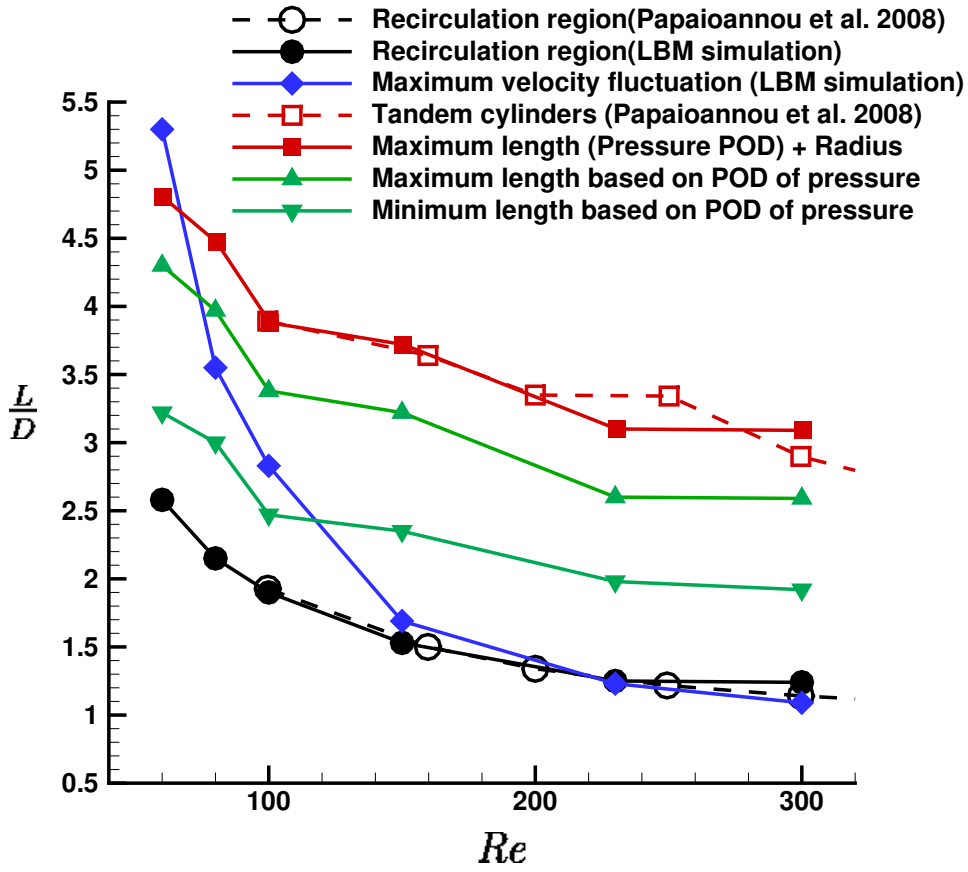

Figure 3.10: Two-dimensional vortex formation length and critical spacing as the change of Reynolds number.

spacing of two tandem cylinders is quite close to the radius of a single cylinder, as shown in Figure 3.10, especially for low Reynolds number ($Re < 200$). The experimental and simulation results also indicate that the POD modes are capable of predicting the spatial distribution and time evolution of vortex shedding and propagation.

Chapter 4

Wake structures of a circular cylinder undergoing controlled motion

In this section, the result of a parametric study of wake structures appearing behind a circular cylinder undergoing controlled motion will be discussed. A duplication of Williamson & Roshko [105]'s research of transverse cylinder oscillations was conducted in a flowing soap film. The research focuses on two forms of phase diagram: the (λ^*,A^*) and the (f^*,A^*) spaces. Here, λ^* is the normalized wavelength $\lambda^* = U_\infty/fD$; A^* is the normalized amplitude $A^* = A/D$; and f^* is the frequency ratio $f^* = f/f_N$. The dimensional parameters are defined as: D is the cylinder diameter, A is the oscillation amplitude, f is the oscillation frequency, U_∞ is the (uniform) background flow speed, and f_N is the frequency of vortex shedding from a fixed cylinder. The bifurcation diagram of the space (λ^*,A^*) is shown in Figure 4.1 while the phase map of the space (f^*,A^*) is displayed in Figure 4.2. There are several wake modes that appear as the amplitude and frequency of oscillation are varied. These include patterns such as a "2P" mode (two pair of vortices formed per cycle), a "2S" mode (two single vortices formed per cycle), a "Coalescing 2S" wake (a "2S" mode initially develops behind the cylinder, but the vortices coalesce downstream), a "Perturbed von Karman" wake, a "P+S" mode (a pair of vortices and a single vortex formed in each cycle) and an "Unsynchronized wake" as shown in Figure 4.3(F). Previous research includes 3D experiments [69, 105] and 2D numerical simulations [53]. These experiments and simulations

have some similarities, but disagree in key ways. Leontini *et al.* [53] found no "2P" mode wake pattern behind a circular cylinder oscillated transversely to a uniform background flow in their 2D simulations. They also determined that the synchronization regime and the wake modes observed within the synchronized regime are Reynolds number (Re) dependent. Leontini *et al.* [53] conjecture that the difference with experimental observations [69, 105] is related to the flow dimensionality and Reynolds number, but they do not provide any concrete explanation. The obvious reason for the difference would appear to be the third spatial dimension in the experiments. However, our (quasi) two-dimensional experimental results show that the "2P" wake structure can occur in a (quasi) two-dimensional experiment (see Figure 4.1, Figure 4.2, Figure 4.3), results that are consistent with earlier findings for in-line cylinder oscillations [22].

4.1 Oscillating cylinder setup

The soap film system in this research used the inclined film design adapted from Wang *et al.* [98] as shown in Figure 2.3. The soap solution was 1% (by volume) Dawn $Escapes^{TM}$ dish soap (Proctor & Gamble) in water. The average background flow speed used for these experiments was $U_\infty = 0.677 \pm 0.038\,\mathrm{m/s}$. The volumetric flow rate was measured simultaneously, and using mass conservation the film thickness was determined to be around $h_\mathrm{f} = 3.37\mu\mathrm{m}$.

The oscillating cylinder was forced to oscillate in transverse harmonic motion relative to the uniform background flow using a scotch-yoke mechanism driven by a brushless motor, with the center position of the cylinder given by:

$$y(t) = A\sin(2\pi f t + \phi). \tag{4.1}$$

The cylinder was fabricated from a circular acrylic rod with diameter $D = 6.35\,\mathrm{mm}$. The cylinder was penetrated perpendicularly through the flowing soap film. The cylinder was surrounded by a meniscus which follows the cylinder, so that the effective diameter of the cylinder becomes $D + 2m$ [22]. The vortex shedding frequency of fixed obstacles in the flow was used to determine the width m of the meniscus. The Strouhal number St was measured according to the vortex shedding frequency. Using equation (2.5), each St value was converted into a Reynolds number. Two different obstacles were used to determine the meniscus width m. One obstacle was the circular cylinder with diameter $D = 6.35\,\mathrm{mm}$ and the other was a very thin (thickness $h_\mathrm{d} = 25.4\,\mu\mathrm{m}$) circular disk of clear polyester film with the same diameter. For the circular disk, the effective diameter is almost as same as the actual diameter of the disk due to its small thickness. Because of the different effective diameters ($D + 2m$ and D), the Reynolds number varied between the two obstacles, so the vortex shedding frequencies based on the corresponding St also exhibited some difference. For the same flow speed and viscosity, the meniscus width m could be deduced from equation (2.5) by iteration. Therefore the meniscus width m was found to be around $0.325\,\mathrm{mm}$ for the current experiment, so that the effective diameter for the circular cylinder was approximately $7\,\mathrm{mm}$. The Reynolds number based on the effective diameter was $Re = 235 \pm 14$.

Flow visualization was used to investigate the wake structures. The frequency of vortex shedding downstream of the second cylinder was determined by monitoring the intensity variation at a location that was $5D$ downstream of the cylinder position in the flow. The frequency content of the flow at this position was extracted by taking a Fast Fourier Transform (FFT) of the spatially-averaged intensity in the selected area. In all experimental tests the vortex shedding frequency was $f < 40\,\mathrm{Hz}$. For each run, the wake patterns were recorded in 1400 frames at a frame rate of $170\,\mathrm{Hz}$. The use of 845 separate parameter values gave sufficiently fine resolution to allow for a comprehensive parametric study of distinct wake

patterns within this parameter regime. The boundaries between different wake patterns were determined by the support vector machine method as described in Subsection 2.3.2.

4.2 Vortex shedding classification for wake of the oscillating cylinder

The "2P" mode regime is located in the center of Figure 4.1 and covers a large area in this figure. The transition between the "2P" mode and the "Unsynchronized wake" lies between $\lambda^* = 8$ and $\lambda^* = 10$ for the full range of A^* considered. This value qualitatively agrees with the 3D experimental results [69, 105]. However, the "Perturbed von Karman" wake is distinguished from the "Unsynchronized wake" in the current classification. Both the amplitude and the frequency in the "Perturbed von Karman" regime is small, so the cylinder's transverse oscillation has a small effect in the wake. Thus, the wake pattern here is more periodic compared to the "Unsynchronized wake". The other four wake patterns are concentrated in the small wavelength region as shown in Figure 4.1. For small normalized wavelength, the wake shows the "2S" mode for which the normalized amplitude is also small. In contrast, the wake appears as the "P+S" mode when the normalized amplitude is increased beyond 0.4. The "Off-plane" vibration mode is located on the top left corner in Figure 4.1. For this mode, both the amplitude and the oscillation frequency are large, so a large "Off-plane" vibration is induced by the cylinder's oscillation. Several dark areas are observed in the wake images for the "Off-plane" cases, as shown in Figure 4.3(G). Under this circumstance, it is assumed that the flow behavior is no longer "quasi-2D", so this wake pattern is not considered suitable for comparison with previous experiments and simulations. In general, the wake regions for the different wake patterns (except for the "Off-plane" vibration mode) qualitatively agree with the 3D experiments [69, 105].

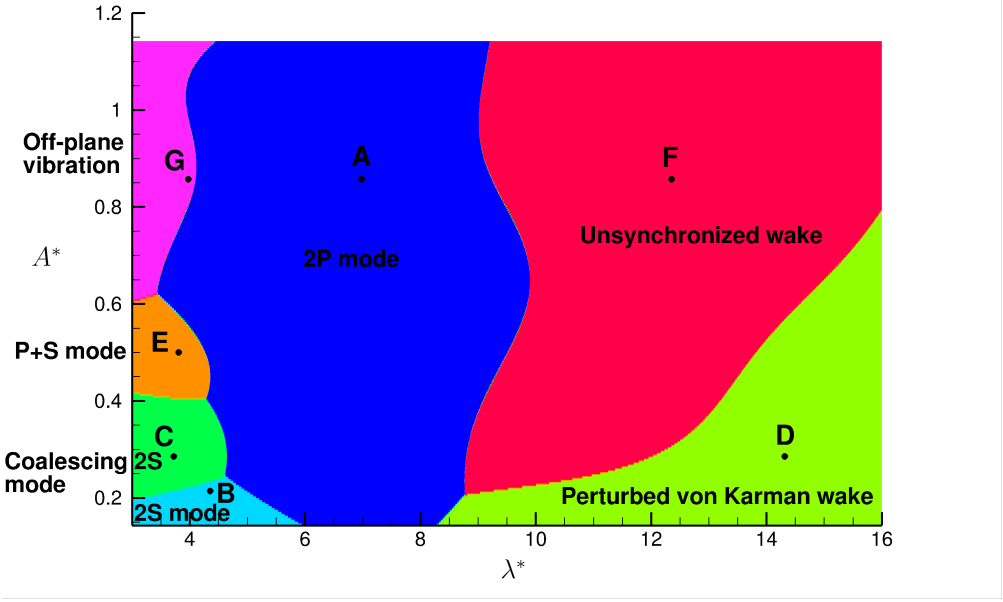

Figure 4.1: Bifurcation diagram of wake patterns for normalized wavelength and normalized amplitude.

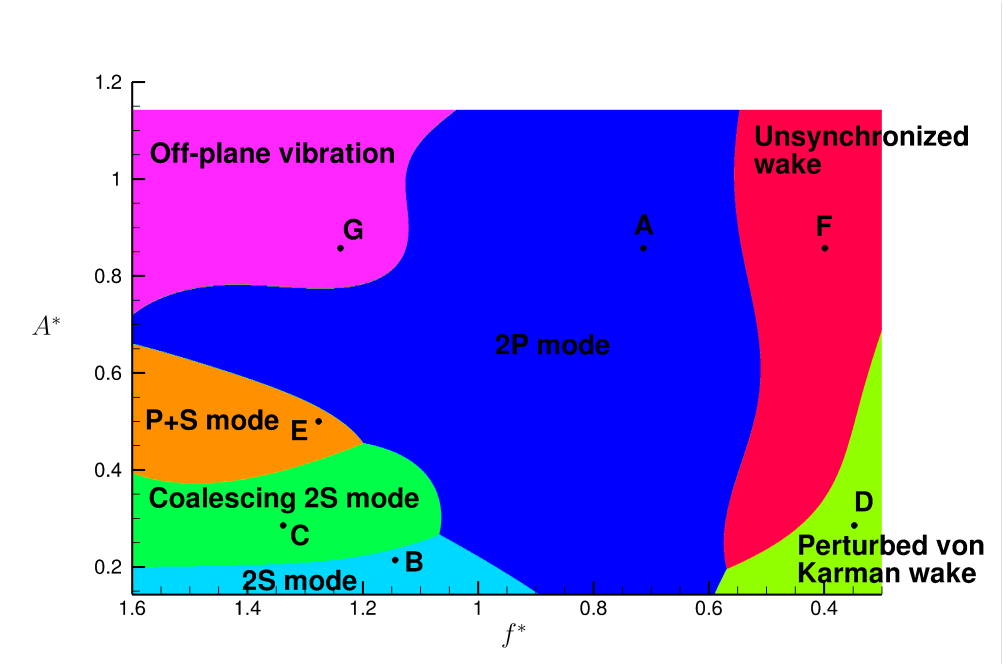

Figure 4.2: Bifurcation diagram of wake patterns for frequency ratio and normalized amplitude.

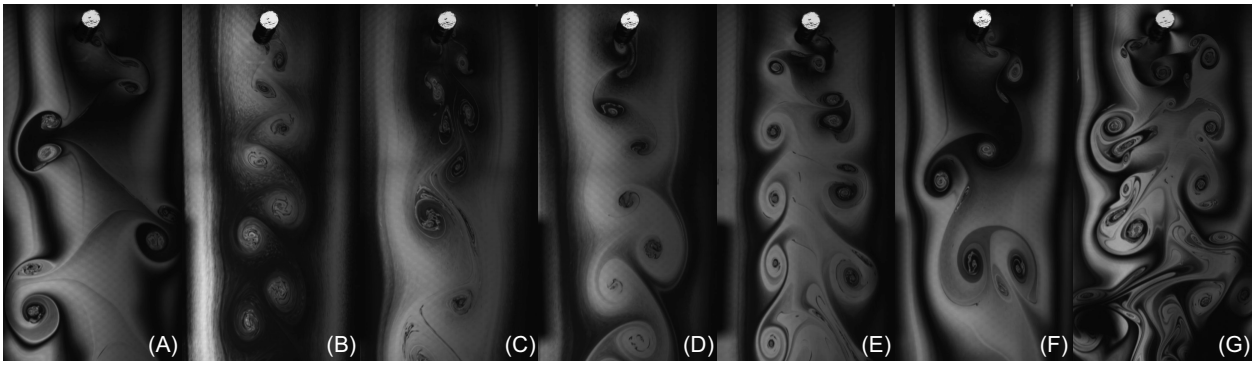

Figure 4.3: Wake patterns: (A) 2P wake model; (B) 2S wake model; (C) Coalescing 2S wake; (D) Perturbed von Karman wake; (E) P+S model; (F) Unsynchronized wake; (G) Off-plane vibration.

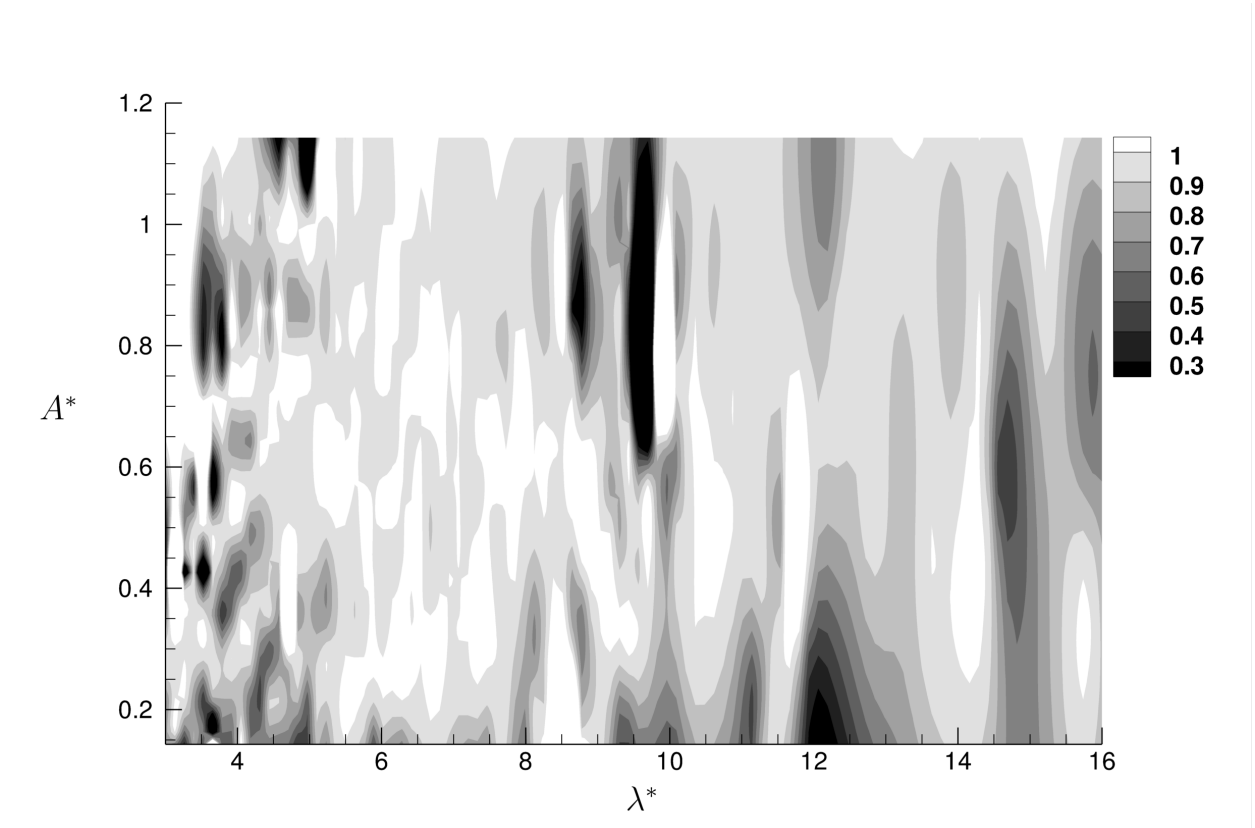

Figure 4.4: Maximum probability of the predicted wake patterns as determined by a neural network.

	A	B	C	D	E	F	G
"2P" wake model	**97.93%**	0%	0%	0%	00.14%	1.93%	0%
"2S" wake model	21.07%	**35.21%**	15.79%	18.14%	00.93%	8.86%	0%
"Coalescing 2S" wake	4.43%	0.5%	**95.07%**	0%	0%	0%	0%
Perturbed von Karman wake	0%	0.14%	0%	**99.86%**	0%	0%	0%
"P+S" model	3.14%	0.5%	0.57%	0.79%	**94.43%**	0.21%	0.36%
Unsynchronized wake	3.93%	0.07%	0.14%	0.36%	0%	**95.5%**	0%
Off-plane vibration	9%	0.21%	0.36%	0.07%	0.5%	0.07%	**89.79%**

Table 4.1: Probability of the predicted wake patterns.

The phase map of the space (f^*,A^*) in Figure 4.2 is shown for comparison with the 2D simulations [53]. It is possible to generate a clear "2P" wake in the soap film, which is not found in the 2D computational simulations [53]. Basically, the soap film experimental results are closer to the previous 3D experiments [69, 105] than the 2D simulations [53]. One possible reason why this (quasi) two-dimensional experiment disagrees with the 2D simulation is the existence of the meniscus between the film and the cylinder, as discussed in Section 4.4.

Figure 4.4 shows the probability of the predicted wake patterns as determined by a neural network for the (λ^*,A^*) space. The darker regimes indicate a lower probability of the predicted wake classification. For the darkest area, the probability is around 30% for the most possible wake pattern as predicted by the wake classifier. Areas with the lowest probability suggest that transitions occur between different wake regimes at these parameter values. One obvious transition boundary is located between the "2P" wake mode and the unsynchronized wake, while the other obvious transition regimes are focused in the low wavelength area where the "2P" wake mode transitions to the "P+S" wake or the "2S" wake. The highest probability is close to 1, so the wake patterns located in the corresponding areas remain stable in a very predictable way. Table 4.1 shows the probability of wake patterns in the 7 regimes shown in Figure 4.1, Figure 4.2 and Figure 4.3. Except for the "2S" wake mode, the probability for each labeled point ($A-G$) is over 89%, so the wake classification can be considered quite robust for these vortex shedding regimes. On the other hand, the highest

predicted probability for point B is only 35.21%, and the classifier indicates that the "2S" wake mode is the most frequently occurring mode at this point. This low probability suggests that there is overlap of multiple wake modes for these locations. Morse & Williamson [69] also found overlap of the "2S" wake mode with other modes.

4.3 Spectra of wake patterns for oscillating cylinder

Figure 4.5 shows the spectrum distributions of representative wakes for the labeled locations $(A - F)$ in Figure 4.1 and Figure 4.2. The oscillation frequency of the controlled transverse motion and the vortex shedding frequency of the stationary cylinder are labeled in Figure 4.5. For point A, the wake pattern is definitely the "2P" mode according to the probability prediction in table 4.1. There are two obvious peaks in Figure 4.5(A): 13.95 Hz and 27.89 Hz. The former frequency is the same as the oscillation frequency in this case, so the flow is fully synchronized with the transverse motion of the cylinder. The second frequency is almost twice that of the oscillation frequency. For the "2P" wake mode, two pairs of vortices are formed per cycle, so it is reasonable to expect two fundamental frequencies to appear in the spectra. Point B, in contrast, shows only one significant peak at 21.58 Hz. The flow is also fully synchronized with the transverse motion in this case and appears as the "2S" mode. The "Coalescing 2S" wake, represented by point C, shows multiple peaks in the spectra. One of the peaks is located at 25.23 Hz, which is also the frequency of the transverse motion. The first major fundamental frequency is 10.86 Hz, which is much smaller than the oscillation frequency. For the "Coalescing 2S" mode, the vortices coalesce downstream and merged into large vortices, so it is reasonable to find a low frequency component in the spectra. For the perturbed von Karman wake (the point D), there are two peaks in the spectra: 14.11 Hz and 20.75. The 14.11 Hz is close to twice the oscillation frequency, while the 20.75 Hz is close to

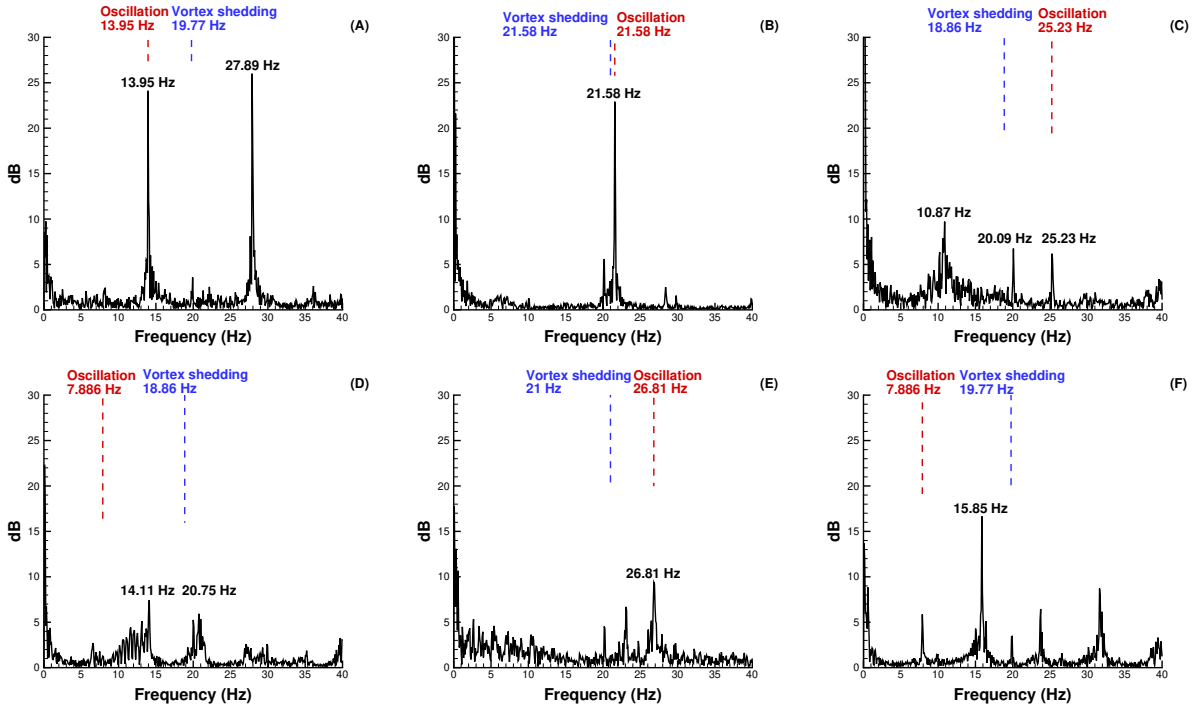

Figure 4.5: Spectra of the wake patterns.

the vortex shedding frequency (18.86 Hz). The difference is probably caused by the dynamic system shift of the oscillating system. The wave shape of the vortex street induced by the transverse motion causes the former fundamental frequency as shown in Figure 4.3. The latter fundamental frequency is related to the vortex shedding into a standard von Karman vortex street. Thus the wake pattern in this case is a disturbed von Karman vortex street. The first fundamental frequency of the spectra for point E is 26.81 Hz, which is the same as the oscillation frequency, so the "P+S" mode is also a fully synchronized flow. The spectra for the unsynchronized wake (point F) has multiple peaks. Although one of the peaks has the same frequency as the oscillation frequency, the power of this frequency is small compared to the other peaks. The flow patterns for point F do not appear to be obviously periodic with synchronized patterns, so the wake patterns are classified as unsynchronized wakes.

4.4 Conclusions

A systematic parametric study was conducted of the wake structure behind a controlled transversely oscillating cylinder. The inclined gravity-driven flowing soap film was used for visualizing the two-dimensional wake. Neural network and support vector machine methods assisted the wake classification and the identification of boundaries between different wake regimes.

There are several wake modes that appear as the amplitude and frequency of oscillation of the cylinder are varied. The critical parameters in the current research focus on the normalized wavelength λ^*, the normalized amplitude A^* and the frequency ratio f^*. The wake modes were discussed in two phase maps: the (λ^*,A^*) and the (f^*,A^*) spaces. The existing literature disagrees on the details of the map of vortex-shedding regimes, with flow dimensionality considered to be the primary factor. New experiments in a (quasi-)2D flowing soap film were implemented to investigate the impact of system dimensionality on the wake patterns generated behind an oscillating cylinder. These experimental results show that the "2P" wake structure can occur in a (quasi) two-dimensional experiment, results that are consistent with earlier findings for in-line cylinder oscillations [22] in a soap film. The phase map of the vortex shedding regimes for the (quasi) two-dimensional experiment qualitatively agrees somewhat surprisingly with previous experiments (3D). One possible reason why this (quasi) two-dimensional experiment disagrees with the 2D simulation is the existence of the meniscus between the film and the cylinder. The soap film experimental data are in excellent agreement with 2D numerical simulations when comparing the mid-wake vortex dynamics [102, 106], but the cylinder and corresponding meniscus were always stationary in those cases. For the case of a controlled transverse oscillation, the meniscus follows the cylinder's motions, so the shape of the meniscus in a film might not be constant and more or less fluid could accumulate in it. Due to the similarity of the present results with those for a

real 3D wake flow, the soap film experimental data could help with understanding (real) 3D vortex-induced vibration.

Chapter 5

Wake structures of two stationary tandem circular cylinders

5.1 Tandem-cylinder setup

The wake structures of two stationary tandem circular cylinders were investigated in the inclined soap film setup as described in section 2.1. The soap solution was 4% (by volume) Dawn $Escapes^{TM}$ dish soap (Proctor & Gamble) in water. The average speed of the background flow was measured by the particle tracing velocimetry (PTV) method to be $U_\infty = 0.732 \pm 0.009\,\mathrm{m/s}$ for these experiments. The film thickness was determined to be $h_\mathrm{f} = 2.25 \pm 0.03\,\mu\mathrm{m}$ by measuring the volumetric flow rate. Thus our system, assuming $\rho = 1.0\,\mathrm{g/cm^3}$ and $E_M \approx 22\,\mathrm{mN/m}$, had $v_M \approx 4.4\,\mathrm{m/s}$ and $\mathrm{M}_e < 0.2$ for all experiments. Therefore, any compressible-like effects caused by the film elasticity were assumed to have a negligible effect on the results reported here.

Two disks with controlled positions were used as stationary cylindrical obstacles in the flow. To minimize the undesirable effects from an object protruding through the surface, we used the approach of [22]: our cylinders consisted of very thin (thickness $h_\mathrm{d} = 25.4\,\mu\mathrm{m}$) circular disks of clear polyester film (McMaster–Carr, USA) with diameter $D_\mathrm{d} = 4.4\,\mathrm{mm}$. These disks were held in the plane of the film by surface tension. Since the disk thickness was close to the film thickness, the meniscus effect was small, giving less than 1% variation in the

effective diameter of each disk, which we neglect. The stationary position of each disk in the (x, y) plane of the film was controlled by two carbon fiber rods (diameter 1.5 mm) that pass through two holes (diameter 1.7 mm) in the disk; each disk was allowed to move along the rods as needed to remain in the film. The upstream pair of rods was connected to a drive screw that was driven by a 4-6V DC drive stepper motor (Banggood, Hong Kong), enabling controlled variation of the cylinder spacing L. Wake data was collected with L held fixed. Between periods of data collection, L was increased or decreased with $(\mathrm{d}L/\mathrm{d}t)/U_\infty \approx 0.001$ while maintaining steady flow in the film, so that the changes in L can be considered quasi-static. Reported values for ℓ were determined with a precision of ± 0.02.

The frequency of vortex formation downstream of the second cylinder was determined by monitoring two locations in the flow, labeled P_1 and P_2 in Figure 1.6(b). The intensity of the reflected light at these two "probe" locations is a function of the flow pattern in the film. The frequency content of the flow was extracted by taking a Fast Fourier Transform (FFT) of the spatially-averaged intensity in each probe area. Example spectra are shown in Figure 1.6(c,d). In all experimental tests the vortex formation frequency was $f < 40$ Hz.

5.2 Results

Three independent experimental trials were conducted at Re ≈ 100. Testing parameters are listed in table 5.1. For each trial, the dimensionless center-to-center cylinder spacing was varied over the range $1.3 \leq \ell \leq 6.6$ with a resolution $0.1 \leq \Delta\ell \leq 0.9$. Hysteresis effects were investigated by first incrementing the spacing from $\ell = 1.3$ to 6.6 and then decrementing from $\ell = 6.6$ to 1.3. Visual inspection of wake patterns and calculation of Strouhal numbers were used to determine the critical spacing of the two tandem circular cylinders. Example wake patterns from Trial 3 are shown in Figure 5.1.

Trial	U_∞[m/s]	f [Hz]	St	Re	$\ell_{\mathrm{c,min}}$	$\ell_{\mathrm{c,max}}$
1	0.742 ± 0.013	28.08 ± 0.25	0.167 ± 0.004	100 ± 9	2.91–3.04	3.92–4.06
2	0.724 ± 0.009	27.22 ± 0.25	0.165 ± 0.004	98 ± 7	2.89–3.03	3.93–4.05
3	0.729 ± 0.004	27.59 ± 0.25	0.166 ± 0.003	100 ± 5	3.00–3.13	3.90–4.03

Table 5.1: Experimental parameters for the three test runs: f and St were measured for flow past an isolated cylinder; Re was estimated with (2.5); bounds on Re and St were determined using min/max propagation of error; hysteresis bounds $\ell_{\mathrm{c,min}}$ and $\ell_{\mathrm{c,max}}$ were determined by decreasing and increasing ℓ, respectively.

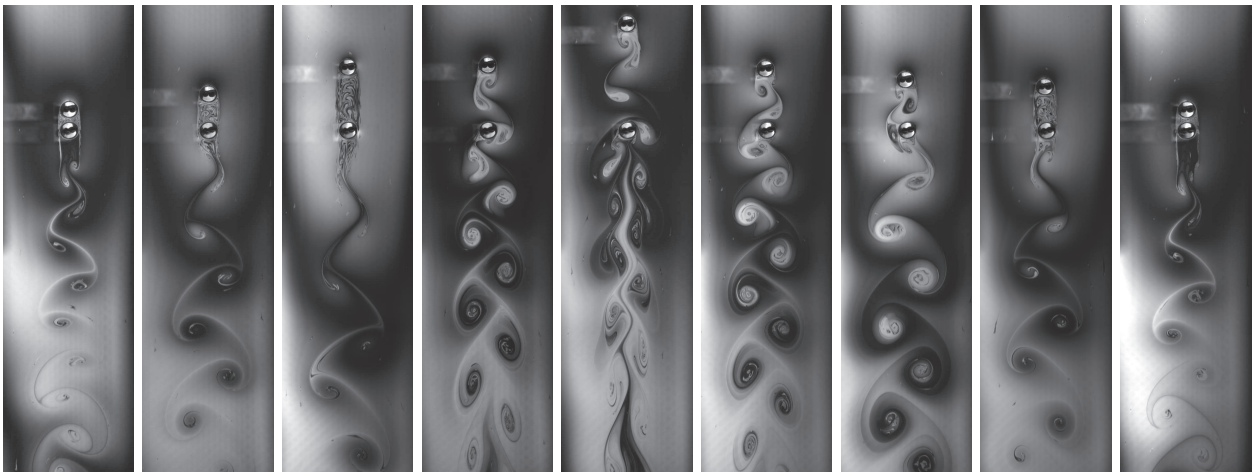

(*a*) (*b*) (*c*) (*d*) (*e*) (*f*) (*g*) (*h*) (*i*)

Figure 5.1: Wake patterns as a function of cylinder spacing from Trial 3 for first (*a*)–(*e*) increasing spacing and then (*e*)–(*i*) decreasing spacing; panels are arranged in chronological order. Wake patterns are shown for spacing values of $\ell =$ (*a*) 1.31, (*b*) 2.25, (*c*) 3.90, (*d*) 4.03, (*e*) 6.58, (*f*) 3.82, (*g*) 3.13, (*h*) 2.72, and (*i*) 1.29. Hysteresis is seen when comparing (*c*) and (*g*).

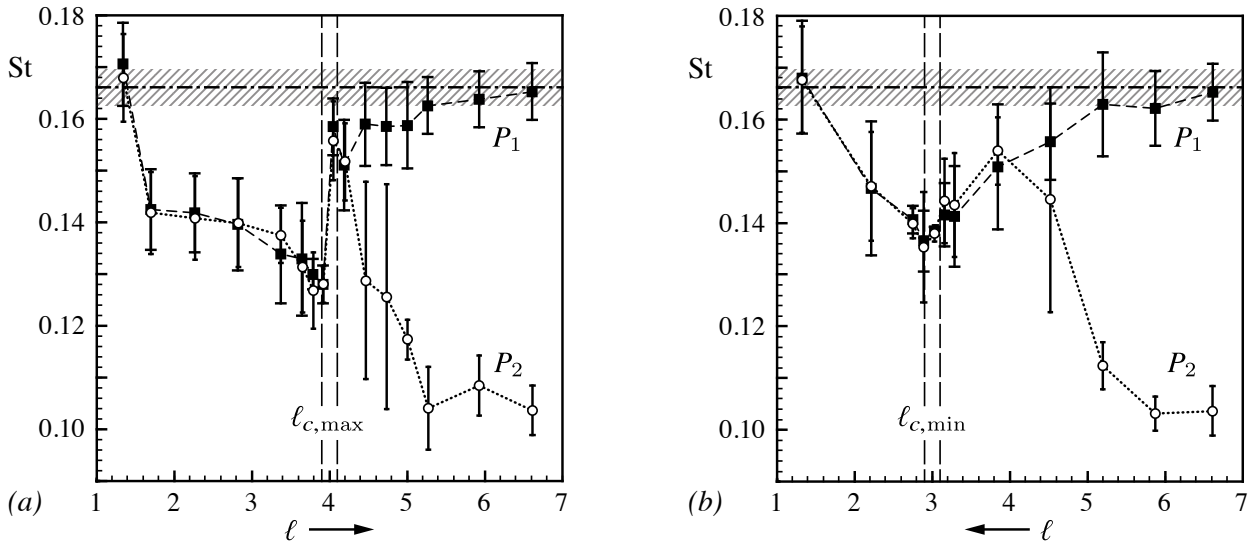

Figure 5.2: Measured Strouhal numbers for probe locations P_1 and P_2 as spacing ℓ is (a) increased and (b) decreased between data collection. Initial conditions for each trial were either (a) flow in the extended body regime at $\ell = 1.3$ or (b) flow in the co-shedding regime at $\ell = 6.6$. Error bars show standard deviation in St; standard deviation in ℓ is covered by the widths of the (narrow) error bar end caps for P_2. Vertical dashed lines mark the estimated bounds on (a) $\ell_{\mathrm{c,max}}$ and (b) $\ell_{\mathrm{c,min}}$; horizontal dashed-dotted lines show the St value for the isolated cylinder, with hatching indicating the estimated error in that value.

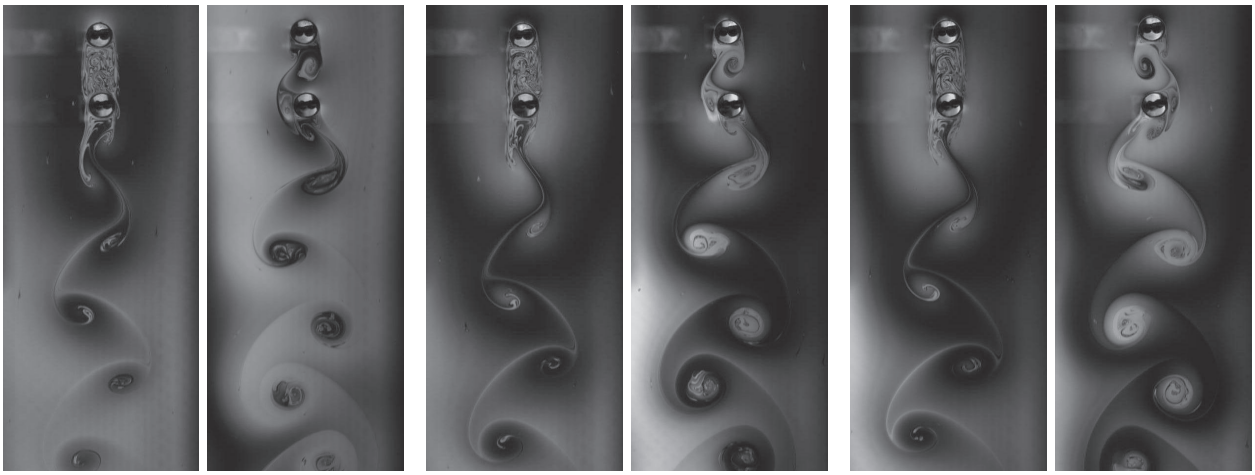

Figure 5.3: Wake images in the case of decreasing ℓ for Trial 1 with $\ell = (a)$ 2.91 and (b) 3.04; Trial 2 with $\ell = (c)$ 2.89 and (d) 3.03; and Trial 3 with $\ell = (e)$ 3.00 and (f) 3.13.

When increasing ℓ for each trial, the Strouhal number varied in a pattern consistent with previous observations. The St values for both probes with increasing ℓ are shown in Figure 5.2(a); values shown are an average from the three trials. When $\ell \approx 1$, St was similar to that observed for an isolated cylinder. The Strouhal number then decreased with increasing ℓ to a minimum value of St ≈ 0.13 at $\ell \approx 3.9$. As the spacing was increased to $\ell \approx 4.1$, the wake frequency suddenly increased to give St ≈ 0.16, corresponding to a transition from the reattachment regime to the co-shedding regime. The inclusive range from the three trials (see table 5.1) indicates that the upper bound for the critical spacing lies in the range $3.9 \lesssim \ell_{c,max} \lesssim 4.1$.

With decreasing ℓ, the established co-shedding flow persisted for $\ell < \ell_{c,max}$; cf. Figure 5.1(c,f,g). For $\ell \lesssim 4.0$, the Strouhal number gradually decreased with decreasing ℓ for both P_1 and P_2, shown in Figure 5.2(b), displaying only a small jump in value as the flow transitioned from the co-shedding regime to the reattachment regime.

Thus, identifying a critical spacing for decreasing ℓ required consideration of the flow patterns, shown in Figure 5.3. From these visual observations, it was determined that the lower bound for the critical spacing is $2.9 \lesssim \ell_{c,min} \lesssim 3.1$.

A second transition was observed to occur in St for probe P_2 when $\ell \gtrsim 4.2$. This transition, a rapid decrease (or increase) in St with increasing (or decreasing) ℓ, comes from vortex merger leading to formation of a "secondary street" in the far wake of the cylinders [18, 98]. This transition is not considered in detail here.

Figure 5.4 summarizes the simulation results about Strouhal number for various longitudinal spacing including the current simulation and previous research. The variation trend of the present simulation is coincident with the results of previous simulations except for small details such as the position of the critical spacing. Similar to the experimental results, the

critical spacing is where the Strouhal number jumps abruptly. For Huhe-Aode [37]'s water tunnel experiment, the critical spacing for $Re = 100$ is between 4.5 and 5. However, for many two-dimensional simulations starting from [25, 45, 57, 72, 89, 95], the critical spacing is between 3.25 and 4 as shown in Figure 5.4 . The simulation results for this work show good qualitative agreement with the experimental results for two tandem cylinders in a flowing soap film. As shown in table 5.1, the maximum critical spacing $\ell_{c,max}$ with $Re = 100$ for soap film experiment is between 3.9 and 4.06. For the simulation with $Re = 100$, the critical spacing is between 4 and 4.05. The critical spacing of the simulation is extremely close to the upper boundary of the critical spacings of the soap film experiment. The results of Sharman *et al.* [89] and Didier [25] approach the present study most on the critical spacing value. The critical spacing for Sharman *et al.* [89]'s simulation is between 3.7 and 4. Didier [25]'s work shows that the critical spacing is between 3.95 and 4, which is very close to our simulation. The recent simulations made by Lin *et al.* [57], Jiang *et al.* [45] and Tu *et al.* [95] have no results for the spacing between 3.5 and 4, so we are not able to further examine whether the critical spacings they obtained are consistent with the present LBM simulation.

5.3 Conclusions

The critical spacing of two identical tandem circular cylinders in a flowing soap film system at Re ≈ 100 was determined using visual inspections of the wake patterns and calculations of the Strouhal frequencies. Three trials were run with cylinder spacings varying over the range $1.3 \leq \ell \leq 6.6$. The dimesionless spacing ℓ was both increased and decreased quasi-statically with increments $0.1 \leq \Delta\ell \leq 0.9$. Hysteresis was observed in the flow patterns and Strouhal numbers. As ℓ was increased, the transition from the reattachment regime to the co-shedding regime occurred for a critical spacing of $3.9 \lesssim \ell_{c,max} \lesssim 4.1$. When instead ℓ was

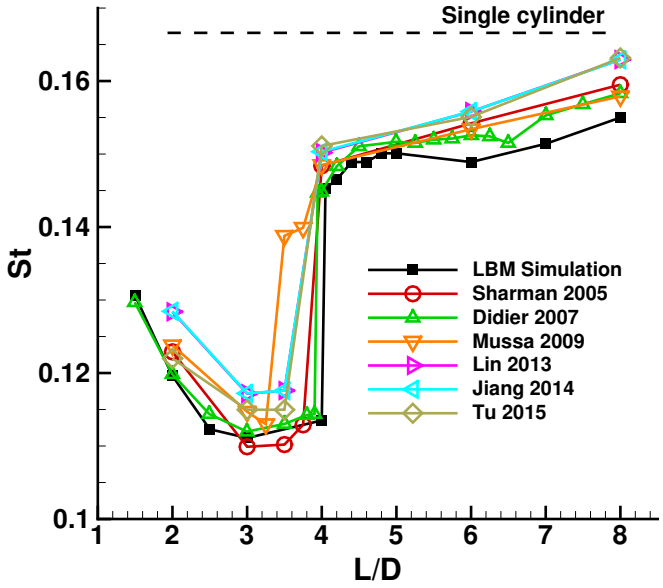

Figure 5.4: The simulation results of $St - L/D$ relations

decreased, this transition occurred for a critical spacing of $2.9 \lesssim \ell_{c,\min} \lesssim 3.1$. Thus, for this flowing soap film system with Re = 99 (± 7), the critical spacing of two identical tandem circular cylinders was found to be $2.9 \lesssim \ell_c \lesssim 4.1$. This study appears to provide the first experimental evidence of critical spacing values that agree with published computational results.

Chapter 6

Flow-induced vibration of the downstream cylinder of a tandem pair

6.1 Flow-induced vibration setup

The gravity-driven, vertically flowing soap film as described in section 2.1.2 was used to generate the quasi-2D flow as shown in Figure 6.1. The soap solution for the soap film was 2% Dawn soap in water. For the experiment reported here, the flow speed U was typically 2.2 m/s as measured by the particle tracing velocimetry (PTV) method (see Chapter 2). The mass ratio of the circular disk to the soap film is $m^* = m_D/m_f = 32.2$. The two identical diameter $D = 6.35$ mm circular disks were laser cut from thin ABS film (76.2 μm thick). Following Couder & Basdevant [22]'s design, the two circular disks floated and remained in the film. As the thickness of the disks is very small, the bordering meniscus has a negligible size and the effective diameter of the obstacle is 6.35 mm. This design was based on Couder & Basdevant [22]'s investigation about two-dimensional vortex formation. We used two carbon fiber rods (1.5mm diameter) passing through two holes (1.6 mm) in the upstream disk while the downstream disk was free to move like a pendulum system as shown in Figure 6.1. The stream-wise displacement x and the transverse displacement y between the upstream disk and the downstream disk are labeled in Figure 6.1. The longitudinal spacing in this study is defined by the normalized mean stream-wise displacement $\ell = x_{mean}/D$. The upstream pair

of rods was connected to a drive screw that was driven by a 4-6V DC drive stepper motor [Banggood, Hong Kong], enabling controlled variation of the longitudinal spacing ℓ. Wake data was collected with ℓ held fixed. Between periods of data collection, ℓ was increased or decreased with $(\mathrm{d}\ell/\mathrm{d}t)/U \approx 0.001$ while maintaining steady flow in the film, so that the changes in x can be considered quasi-static. The increments in x between data points correspond to $\Delta\ell \approx 0.2$; reported values for ℓ were determined with a precision of ± 0.02. The downstream disk is suspended by a thin fiber, which has a negligible mass. The two pivots of the pendulum system are off the soap film plane so only the downstream disk is in the wake of the upstream disk. The length of the pivot arm is 89 mm and the frequency of a periodic motion is $1.67Hz$. As described in Chapter 2, the significance of the compressive effects in a soap film flow are characterized by the elastic Mach number, $\mathrm{M}_e = U/v_M$, where $v_M = \sqrt{2E_M/(\rho\, h_\mathrm{f})}$ is the Marangoni wave speed and $E_M \approx 80\,\mathrm{mN/m}$[23]. The volumetric flow rate was measured simultaneously, and using mass conservation the film thickness was determined to be $h_\mathrm{f} = 2.7\mu\mathrm{m}$. Thus our system, assuming $\rho = 1.0\,\mathrm{g/cm^3}$ and $E_M \approx 80\,\mathrm{mN/m}$, had $v_M \approx 7.75\,\mathrm{m/s}$ and $\mathrm{M}_e < 0.3$ for all experiments. Therefore, while compressible-like effects may appear in a flowing soap film as a result of the Marangoni elasticity, these compressible-like effects were assumed to have a trivial influence on the results reported here. Two spacing variation processes were conducted in the experiment: the mean spacing ℓ was increased gradually from 1.4 to 8 and the mean spacing ℓ was decreased slowly back to 1.4.

The frequency of vortex formation downstream of the second cylinder was determined by monitoring the intensity variation of one location in the flow ($5D$ downstream from the downstream cylinder). The intensity of the reflected light at a particular location is a function of the flow pattern in the film. The frequency content of the flow was extracted by taking a Fast Fourier Transform (FFT) of the spatially-averaged intensity in the location. The frame

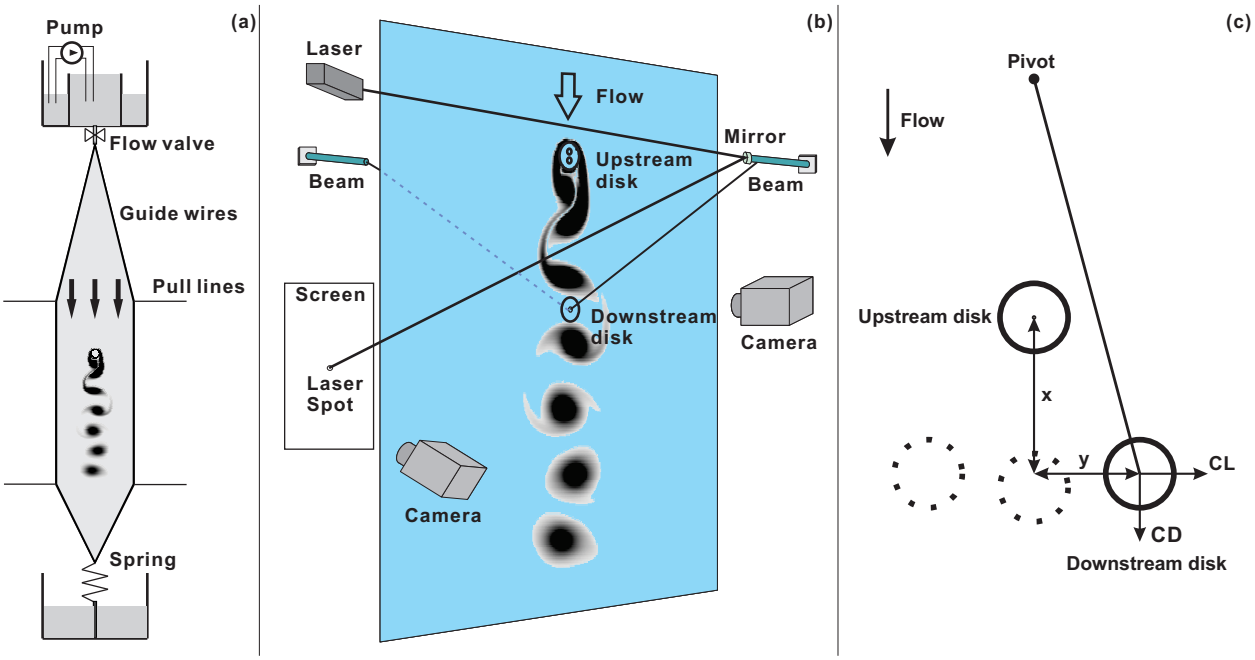

Figure 6.1: Schematic of experimental setup for flow-inducd vibration.

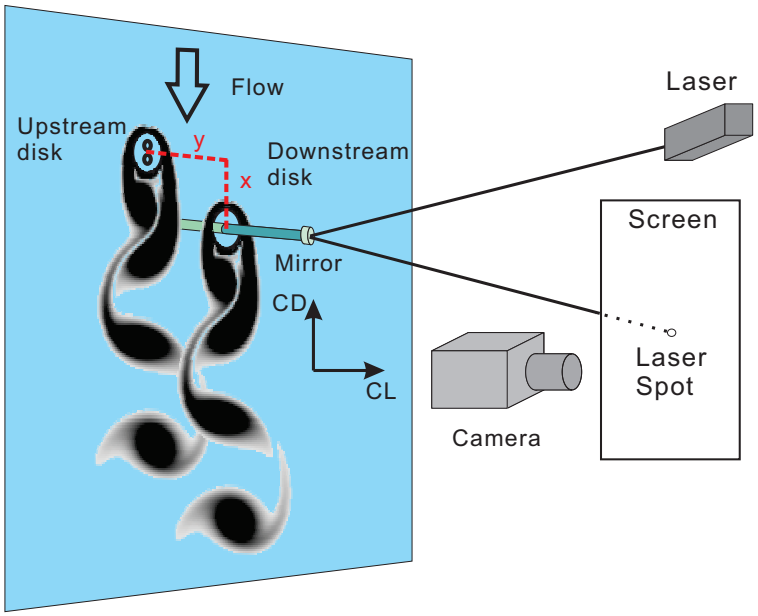

Figure 6.2: Schematic of experimental setup for the steady lift measurment.

rate for the high speed recording is $380Hz$ and each run consists of 3000 frames. Therefore the uncertainty of the FFT analysis is $0.25Hz$. The Reynolds number calculated by the St-Re relationship is $Re = 148 \pm 15$.

To measure the force caused by flow-induced vibration (FIV), a micro-cantilever laser-mirror sensor system inspired by Jia & Yin [43] was used to measure the force induced by the wake of the upstream cylinder as shown in Figure 6.1. The thin fiber passes through the inner hole of the ring and the ends of the fiber are connected to two cantilever beams. A micro mirror is adhered to the tip of one of the two beams. The micro mirror reflects the incident laser beam onto a screen. The spot of the reflected laser beam has the information of the cantilever beam's bending which is related to the force exerted on the beam. The horizontal component of the force comes from the lift on the downstream ring and the vertical component is associated with the drag on the downstream ring. We have calibrated the force measurement and the results show that the methodology can attain a precision of $0.1\mu N$ as Jia & Yin [43] reported. Another force measurement setup was used to measure the steady lift of the downstream disk of a stationary tandem pair as shown in Figure 6.2. In this system, the upstream disk was fixed and the downstream disk was placed on a linear stage oriented in the transverse direction. The transverse displacement of the downstream disk was adjusted by the stepper-motor of the linear stage and the downstream disk was fixed during the measurement. A cantilever beam was penetrated through the center of the downstream disk. The end of the cantilever beam was also adhered to a micro mirror, which reflected a laser beam onto a screen. The steady lift coefficients on a static downstream disk in various staggered positions were measured by this setup by recording the trajectories of the reflected laser spot on the screen. Two high speed cameras were synchronized to record the transient wake and the motion of the reflected laser point for both of the force measurement setups. With the ability to tie together the wake structure and the object motion, and the forces

causing that motion, the relationship between energy generation and flow structure in the simplified model FIV system was investigated.

6.2 Pendulum system with air resistance

The oscillation setup is a pendulum system. The pendulum system is free to swing due to gravity if the soap film is absent. The pendulum equation with a damping term is

$$\frac{d^2\theta}{dt^2} + \frac{\gamma}{m}\frac{d\theta}{dt} + \frac{g}{l}\theta = 0 \tag{6.1}$$

for a drag force $F_R(v) = -\gamma v$. This equation has an exact analytical solution that is oscillatory and/or decaying exponentially [24]. However, for air resistance ($F_R(v) = \frac{1}{2}C_D A\rho v^2$), the equation becomes

$$\frac{d^2\theta}{dt^2} + \frac{\gamma l}{m}\left|\frac{d\theta}{dt}\right|\frac{d\theta}{dt} + \frac{g}{l}\theta = 0. \tag{6.2}$$

For the first half period, the speed of the pendulum is negative ($\frac{d\theta}{dt} < 0$) with a positive inital position ($\theta(0) = \theta_0$). Thus the equation of the pendulum system becomes

$$\frac{d^2\theta}{dt^2} - \frac{\gamma l}{m}(\frac{d\theta}{dt})^2 + \frac{g}{l}\theta = 0 \tag{6.3}$$

for the first half period. The equation 6.3 has no exact solution, but Dahmen [24] came up with a perturbation solution for the equation. Dahmen [24] rewrote this equation as

$$\ddot{\theta} - \epsilon\dot{\theta}^2 + \omega_o^2\theta = 0, \tag{6.4}$$

where $\dot{\theta} = d\theta/dt$, $\epsilon = (\gamma l/m)$ and $\omega_o^2\theta = g/l$. Here we do not discuss the details of the perturbation solution but introduce the damping parameter based on the solution. Accord-

ing to the perturbation solution, the difference between the first two successive amplitudes becomes

$$\theta_0 - |\theta_1| = \frac{4}{3}\epsilon(\theta_0)^2 \tag{6.5}$$

for small parameter ϵ. Thus the constant for the quadratic damping can be calculated based on ϵ, normally giving

$$\gamma = \epsilon m/l = \frac{3m}{4l}\frac{\theta_0 - |\theta_1|}{(\theta_0)^2}. \tag{6.6}$$

The logarithmic decrement due to the air drag is defined as

$$\delta = \ln\frac{\theta_0}{|\theta_1|}. \tag{6.7}$$

The Scruton number (logarithmic decrement times mass ratio) Sc based on the logarithmic decrement becomes

$$Sc = \frac{2m_D\delta}{\rho D^2 h_{\mathrm{f}}}. \tag{6.8}$$

The reduced velocity is

$$V_r = \frac{U_\infty}{fD} \tag{6.9}$$

where f is the oscillation frequency of the pendulum system. The transverse motion of the pendulum system used in the current experiment is plotted in Figure 6.3. The viscous air drag dissipates the energy stored in the oscillation while the frequency f is constantly $1.67Hz$. Due to the small thickness of the flowing soap film (1-10μm), the mass ratio is larger than 30 in the current experiments. Only a few studies have addressed the flow-induced vibration of circular cylinders for such high mass ratio. Zdravkovich & Medeiros [116] investigated the flow-induced oscillation of two tandem circular cylinders for large mass ratio in a wind tunnel. Table 6.1 shows the Scruton number, the reduced velocity V_r and the normalized amplitude A_m/D for both the current experiments and Zdravkovich & Medeiros

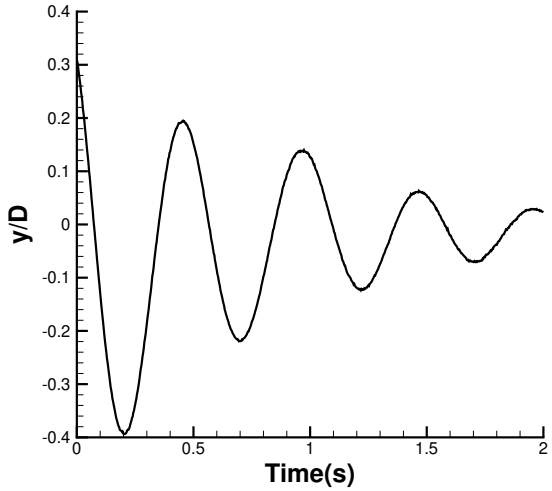

Figure 6.3: The oscillation of the pendulum driven by gravity and damped by the air drag.

	Sc	V_r	A_m/D
Current experiments	170.91	133.27	0.13
Current experiments	30.14	169.75	0.57
Zdravkovich 1991	200	120	0.18
Zdravkovich 1991	100	120	1.15

Table 6.1: Scruton number, reduced velocity and normalized amplitude for $\ell = 4$.

[116]'s results. In Zdravkovich & Medeiros [116]'s experiment, the amplitude A_m/D was 0.18 when Sc was 200 and V_r was 120. For the most relevant case in the current experiment, the amplitude A_m/D becomes 0.13 if Sc is 170.91 and V_r is 133.27. The results for this work show good qualitative agreement with the experimental results from Zdravkovich & Medeiros [116] in a wind tunnel. The Scruton numbers and the reduced velocities for the other two cases differ significantly, so direct comparisons between the two cases are difficult. The qualitative agreement of this one case indicates that the flowing soap film is not only a way to get a better understanding of flow-induced vibration but also a promising tool for optimization design of practical flow phenomenon.

6.3 Wake classification and oscillation modes

In this section, we focus on the variation of the vibration modes and the wake patterns with changes of center-to-center spacing between the two tandem cylinders. Figure 6.1(c) illustrates two critical spatial parameters in this work: the longitudinal spacing between the two tandem circular disks, x, and the transverse displacement of the downstream disk, y. The following discussion of the wake patterns and the oscillation modes will revolve around the normalized spacing x/D and the normalized amplitude y/D. We first introduce several classic wake patterns for various spacings and then discuss the relationship between the spacing, the vibration motion and the force of the downstream disk.

6.3.1 Extended-body wake

If the spacing between two stationary tandem cylinder is extremely small ($\ell < 1.5$), the wake of the two cylinders is close to the wake of one single bluff body. Zdravkovich [113] refers to this kind of wake as the "extended-body regime". We found similar wake patterns in this system even though the downstream disk is free to move. Figure 6.4 shows the extended-body wake observed for the spacing of ($\ell = 1.4$). Figure 6.5 displays the corresponding stream-wise and transverse motions of the downstream disk. The normalized amplitudes of the motions both in the stream-wise direction x/D and in the transverse direction y/D are smaller than 0.04, indicating that the downstream disk is almost stationary in the wake of the upstream cylinder.

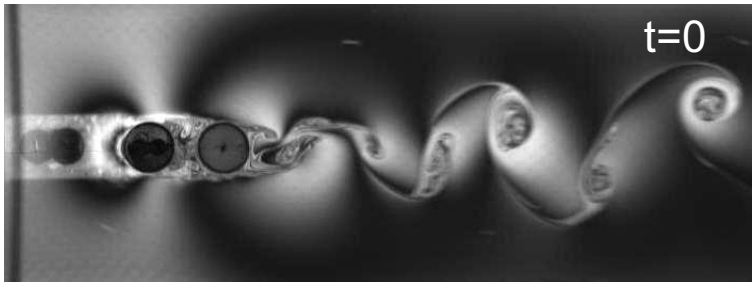

Figure 6.4: Wake patterns for $\ell = 1.4$ ("extended-body" wake) at $Re = 148$. Flow is from left to right. The upstream disk is fixed and the downstream disk is free to oscillate as shown in Figure 6.1. The support mechanism shows through the film upstream of the cylinders but does not interfere with the flow.

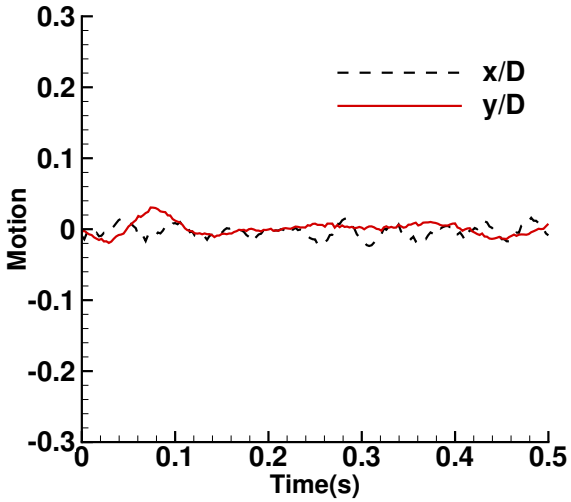

Figure 6.5: Motion of the downstream circular disk for $\ell = 1.4$ ("extended-body" wake) at $Re = 148$ in the stream-wise direction and the transverse direction.

6.3.2 Gap flow switching

The downstream circular disk starts to move if the spacing becomes sufficiently large. For intermediate spacing, the shear layers shed from the upstream cylinder reattach onto the surface of the downstream cylinder. This wake pattern is referred to as the "reattachment regime" for two stationary tandem cylinders. The flow visualization of the soap film with a moving second cylinder also presents the features of the "reattachment wake" when the downstream disk is stimulated to oscillate by the wake of the upstream disk. Figure 6.6 shows the wake patterns for the spacing of ($\ell = 2.1$) during one period of oscillation. As shown in Figure 6.6, when the downstream disk is displaced, streamlines of the flow switch from flowing around the downstream disk to flowing through the gap. This flow acceleration causes a lift force back to the aligned tandem arrangement, and the process is then repeated on the other side. Figure 6.7(a) depicts the trajectories of the the downstream disk during one oscillation period, while Figure 6.7(b) illustrates the motions both in the stream-wise direction and the transverse direction during one half second. The motion of the downstream disk is similar to a narrow "figure 8" shape, as shown in the Figure 6.7(a). Another interesting feature of the motion is that the disk moves upstream when it comes across the centerline of the wake, so the center of the narrow "figure 8" shape distorts toward the upstream direction. This motion is because of the negative drag experienced by the downstream cylinder when the spacing of two tandem disks ℓ is below 3.5. When the disk moves to the edge of the wake, the thrust (the negative drag) becomes weaker and the disk moves downstream. The motions both in the stream-wise direction and in the transverse direction are close to harmonic motion as shown in Figure 6.7(b). The amplitude of the oscillation in the stream-wise direction is much smaller than that in the transverse direction, while the period of the stream-wise vibration is one half of that of the transverse vibration. Jauvtis & Williamson [40] found similar figure-eight type (X, Y) trajectory shapes. In general, the vibration is uniform so

the system offers a relatively constant kinetic energy output.

The spectrum distributions of the oscillation in the stream-wise direction and the transverse direction are plotted in Figure 6.8. The major frequency of the stream-wise oscillation is 21 ± 0.50 Hz while the major frequency of the transverse oscillation is 10.58 ± 0.10 Hz. These two frequencies do not behavior as an exact factor of 2 due to the uncertainty of the FFT analysis. The spectrum distribution of the intensity for $\ell = 2.1$ is shown in Figure 6.9. There are two peaks for the spectrum distribution: $21.06Hz$ and $10.48Hz$. The former one is close to the frequency of the stream-wise oscillation, so the wake pattern is heavily affected by the cylinder's motion. The latter value, 10.48 Hz, is the frequency of the transverse oscillation.

6.3.3 Co-shedding wake

When the spacing between two tandem disks, ℓ, is larger than 3.5, each disk sheds its own vortex wake. This wake pattern is classified as the "co-shedding" wake, as discussed in many studies regarding the wake of two tandem stationary cylinders [76, 93, 111, 114, 118]. Figure 6.10 shows the wake interaction for the spacing of $\ell = 3.9$ in one period. If the downstream disk displaces from the centerline, the upstream disk wake causes, on average, a low pressure region, which provides a restoring force to the centerline. Therefore the downstream disk is induced to vibrate by the alternating resorting force. Figure 6.11(a) displays the trajectories of the downstream disk during one period of oscillation, while Figure 6.11(b) describes the displacements of the downstream disk both in the stream-wise direction and the transverse direction. The motion of the downstream disk in Figure 6.11(b) is quite different from the motion caused by the gap flow switching shown in Figure 6.7(a). The small fluctuations are observed over both the stream-wise motion curve and the transverse motion curve. The complex wake interactions might be contributing to the inconsistent

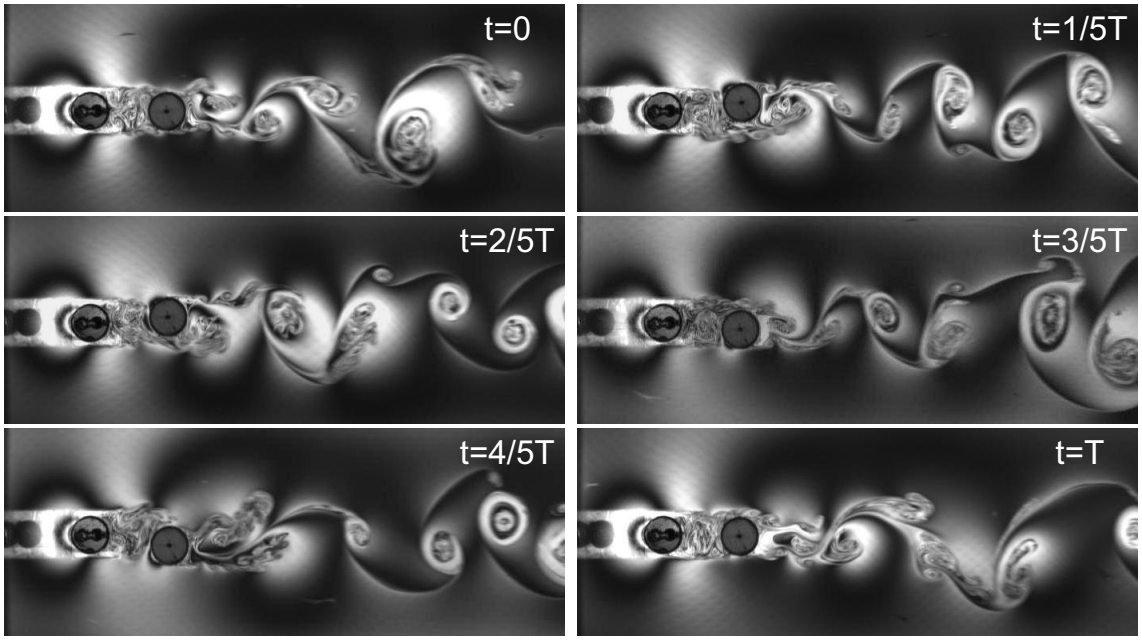

Figure 6.6: Wake patterns of one oscillation period for $x/D = 2.1$ ("Gap flow switching") at $Re = 148$.

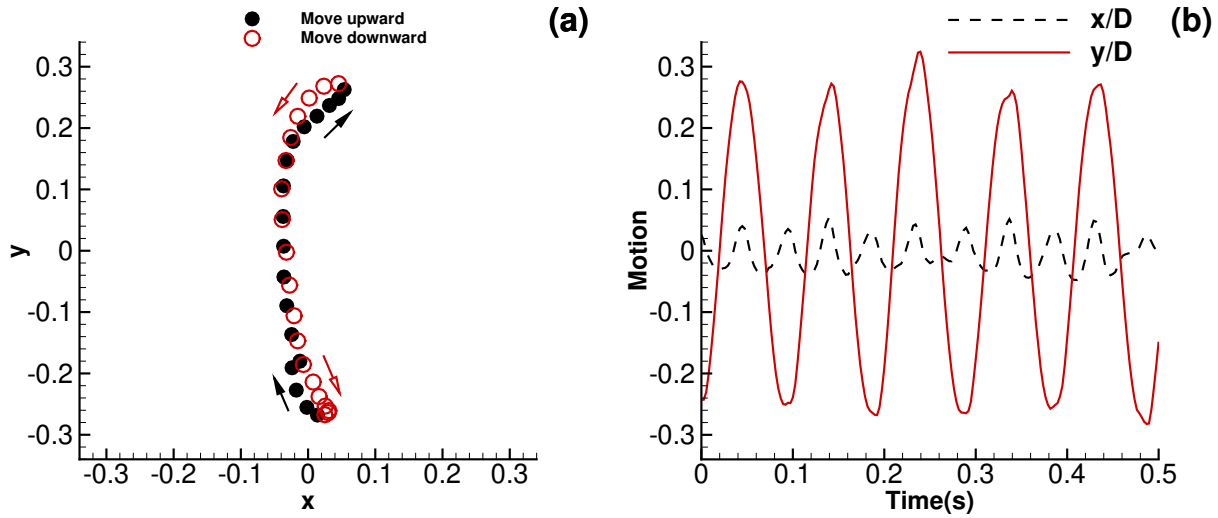

Figure 6.7: Motion of the downstream circular disk for $\ell = 2.1$ ("Gap flow switching") at $Re = 148$: (a) trajectories of the circular disk and (b) the motion curves of the downstream disk in the stream-wise direction and the transverse direction.

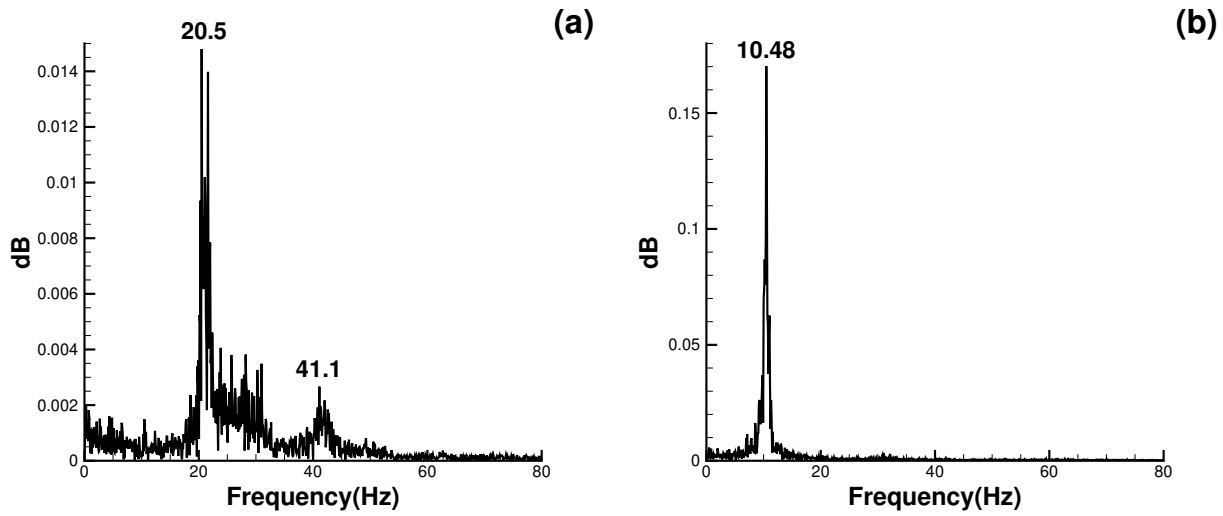

Figure 6.8: Spectrum distribution for motion of the downstream circular disk at $Re = 148$ ("Gap flow switching") for $\ell = 2.1$: (a) stream-wise oscillation (x/D) and (b) transverse oscillation (y/D).

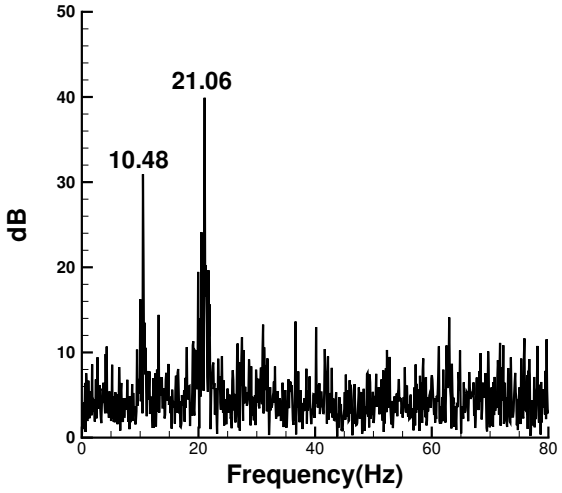

Figure 6.9: Spectrum distribution of the intensity for $\ell = 2.1$ ("Gap flow switching") at $Re = 148$.

motion of the downstream disk. The motion in the stream-wise direction is much smaller than the motion in the transverse direction so it is reasonable to consider the motion as quasi-one-dimensional in this case.

The spectrum distributions of the cylinder's oscillation for $\ell = 3.9$ are shown in Figure 6.12. Three peaks are dominant in Figure 6.12(a): $5.01Hz$, $39.06Hz$ and $59.28Hz$. The first peak at $5.01Hz$ is the same as the first peak in Figure 6.12(b), while both the stream-wise motion and the transverse motion have another peak at 59.28 in Figure 6.12(a, b). Thus, the major frequency of the oscillation is at $5.01Hz$ in the transverse direction but the oscillation also has another frequency component at $59.28Hz$. It is currently uncertain what causes the frequency component at $39.06Hz$ in Figure 6.12(a). However, the stream-wise oscillation is much smaller than the transverse oscillation, so the frequency component $39.06Hz$ has no significant effect on flow-induced vibration. The spectrum distribution of the image intensity for the position $x/D = 3.9$ is shown in Figure 6.13. The only dominant peak in Figure 6.13 is $59.28Hz$, so the wake fluctuation frequency is $59.28Hz$ for the downstream wake.

6.4 Motion amplitude and force response

This section focuses on the effect of the spacing on the wake patterns, the vibration motion and the force response. The amplitude of the oscillation and the "drag" coefficient of the downstream disk are illustrated as a function of the mean spacing of the two tandem disks in Figure 6.14 and Figure 6.15, respectively. Figure 6.16 shows the wake patterns for changes in the spacing for both the increasing spacing process and the decreasing spacing process. The specific positions of wake patterns in Figure 6.16 are labeled from A to L in Figure 6.14 and Figure 6.15.

The amplitude of oscillation in the stream-wise direction is largest when the wake is in the

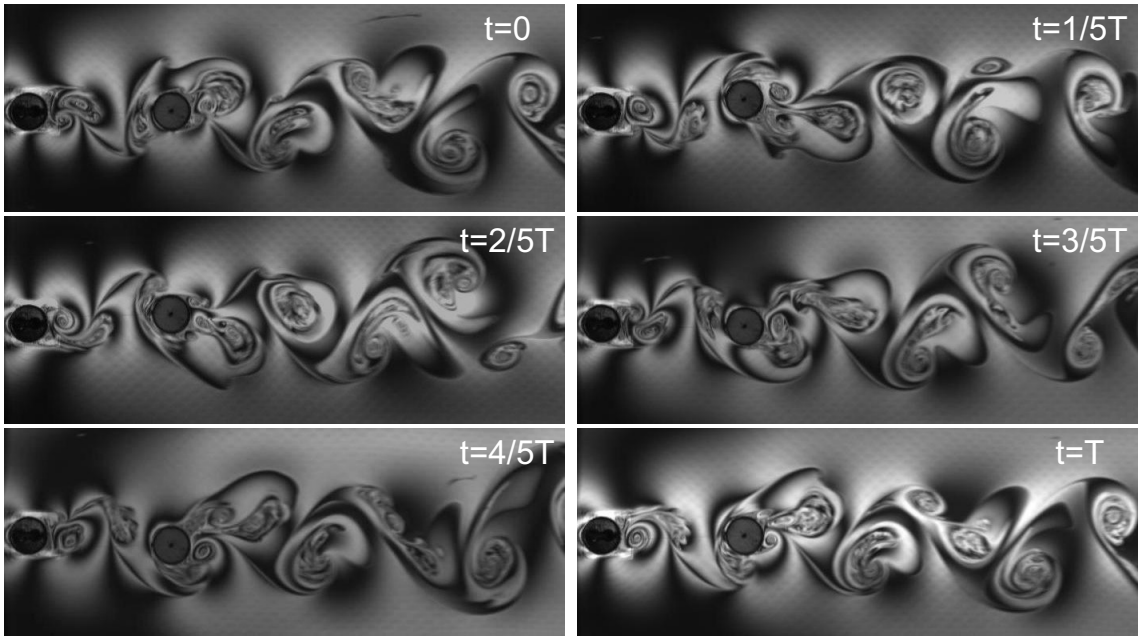

Figure 6.10: Wake patterns of one oscillation period for $\ell = 3.9$ ("Co-shedding" wake) at $Re = 148$.

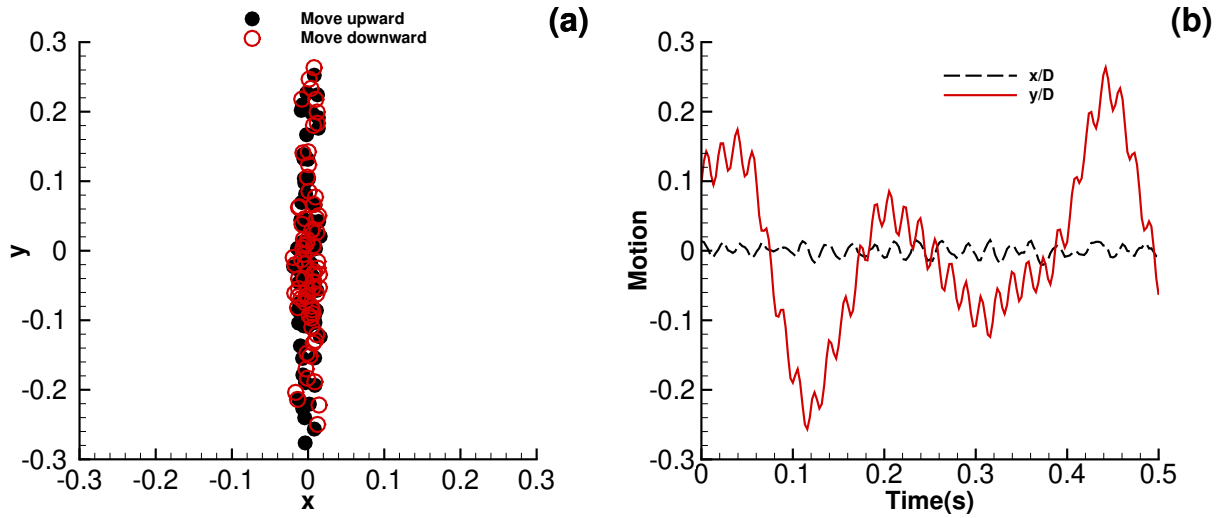

Figure 6.11: Motion of the downstream circular disk for $\ell = 3.9$ ("Co-shedding" wake) at $Re = 148$: (a) trajectories of the circular disk and (b) the motion curve of the downstream disk in stream-wise direction and in transverse direction.

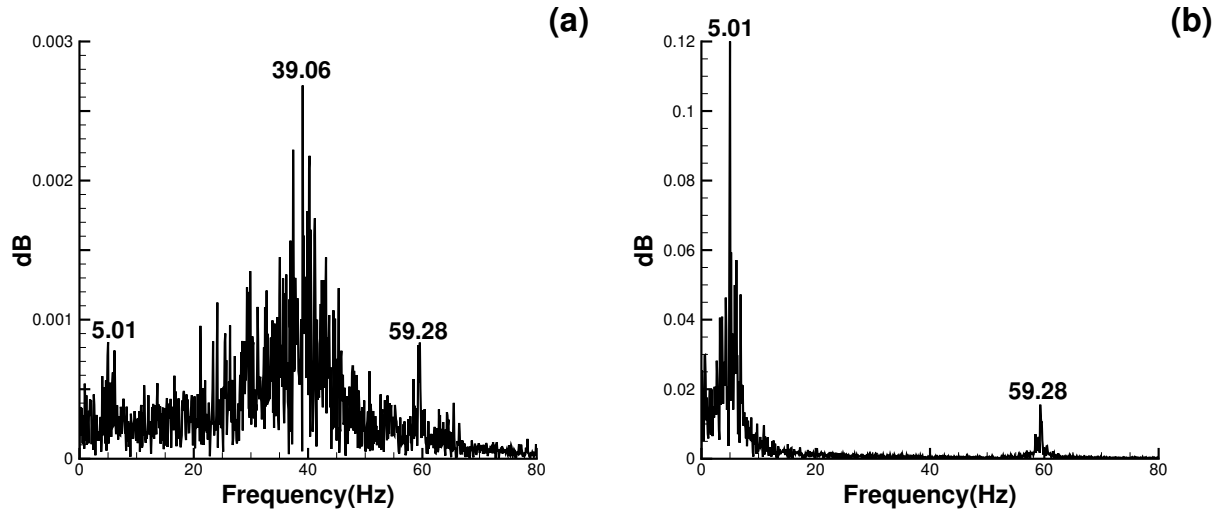

Figure 6.12: Spectrum distribution for motion of the downstream circular disk for $\ell = 3.9$ ("Co-shedding" wake) at $Re = 148$: (a)stream-wise oscillation (x/D); (b)transverse oscillation (y/D).

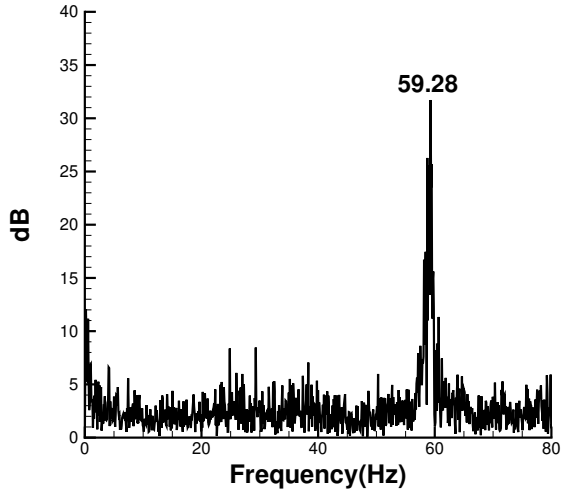

Figure 6.13: Spectrum distribution of the intensity for $\ell = 3.9$ ("Co-shedding" wake) at $Re = 148$.

"gap flow switching" regime. This maximum amplitude is achieved both for the increasing spacing process and the decreasing spacing process, as shown in Figure 6.14(a). Beyond the peak in Figure 6.14(a), the amplitude of the stream-wise oscillation decreases with increasing mean spacing and approaches zero for large ℓ. The transverse vibration displays more variation with changing mean spacing, as shown in Figure 6.14(b). The root-mean-square transverse amplitude y_{rms}/D increases to approximately 0.2 abruptly from almost zero when ℓ changes from 1.4 to 1.6. The transverse oscillation amplitude stabilizes around 0.2 if the mean spacing is between 1.6 and 2.2. The amplitude then decreases quite abruptly from 0.19 to 0.04 when the mean spacing increases from 2.2 to 2.9. As the mean spacing is incremented, the amplitude increases again before a jump occurs around $\ell = 3.5$. Along with the sudden increase of the oscillation amplitude, the wake shifts from the "gap-flow switching" regime to the "co-shedding" regime at a spacing $\ell = 3.5$ as shown in Figure 6.16 (E) and (F). For the "co-shedding" wake regime, the amplitude has another peak at 0.15 when the spacing increases to 3.9. After this peak, the amplitude of the transverse oscillation decreases with increasing mean spacing and reaches close to 0.06 at the largest spacing of $\ell = 7.9$. The quasi-steady process of decreasing the mean spacing has a similar variation trend in amplitude as compared with the quasi-steady increasing process. One notable difference is the hysteresis of the oscillation amplitude between $\ell = 3.1$ and $\ell = 3.5$. When the spacing decreases from 3.3 to 3.1, the amplitude decreases suddenly from 0.13 to 0.07; conversely, the amplitude jumps from 0.07 to 0.13 when the spacing for the quasi-steady increasing process is around 3.5. The switch of wake patterns for the quasi-steady decreasing process is not evident in Figure 6.14(b). The wake alternates from "co-shedding" to "gap-flow switching" when the spacing is around 2.7, as shown in Figure 6.16 (I) and (J). However, the amplitude for wake (I) and wake (J) is extremely close, so they appear as one single data point in Figure 6.14(b).

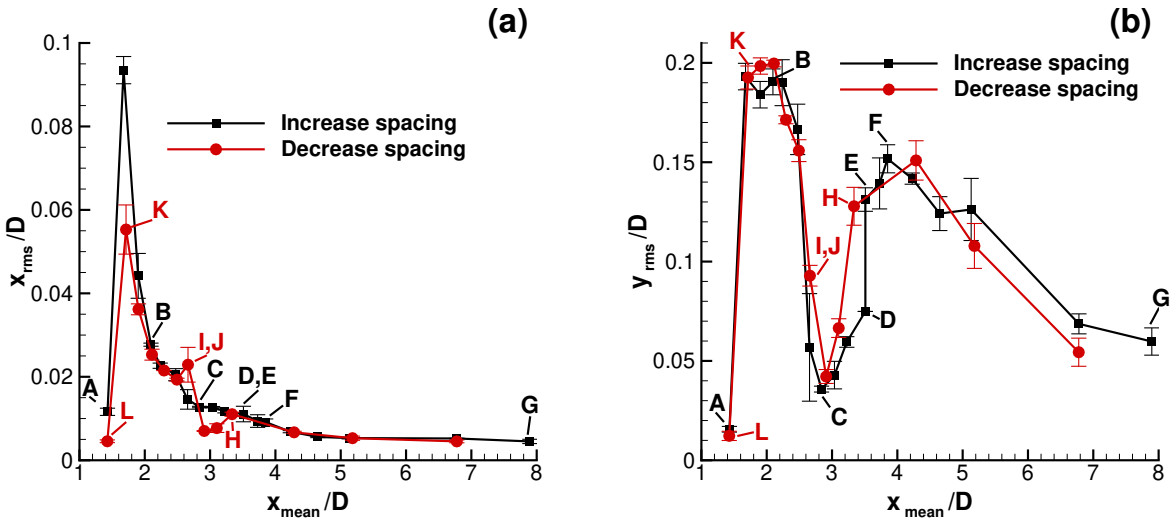

Figure 6.14: Root-mean-square of the downstream disk's displacements at $Re = 148$: (a) stream-wise; (b) transverse.

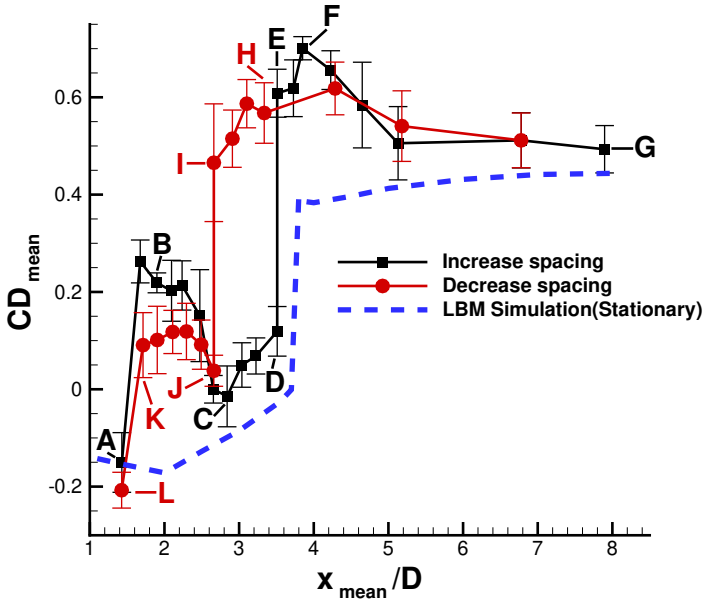

Figure 6.15: Force of the downstream cylinder in longitudinal Direction.

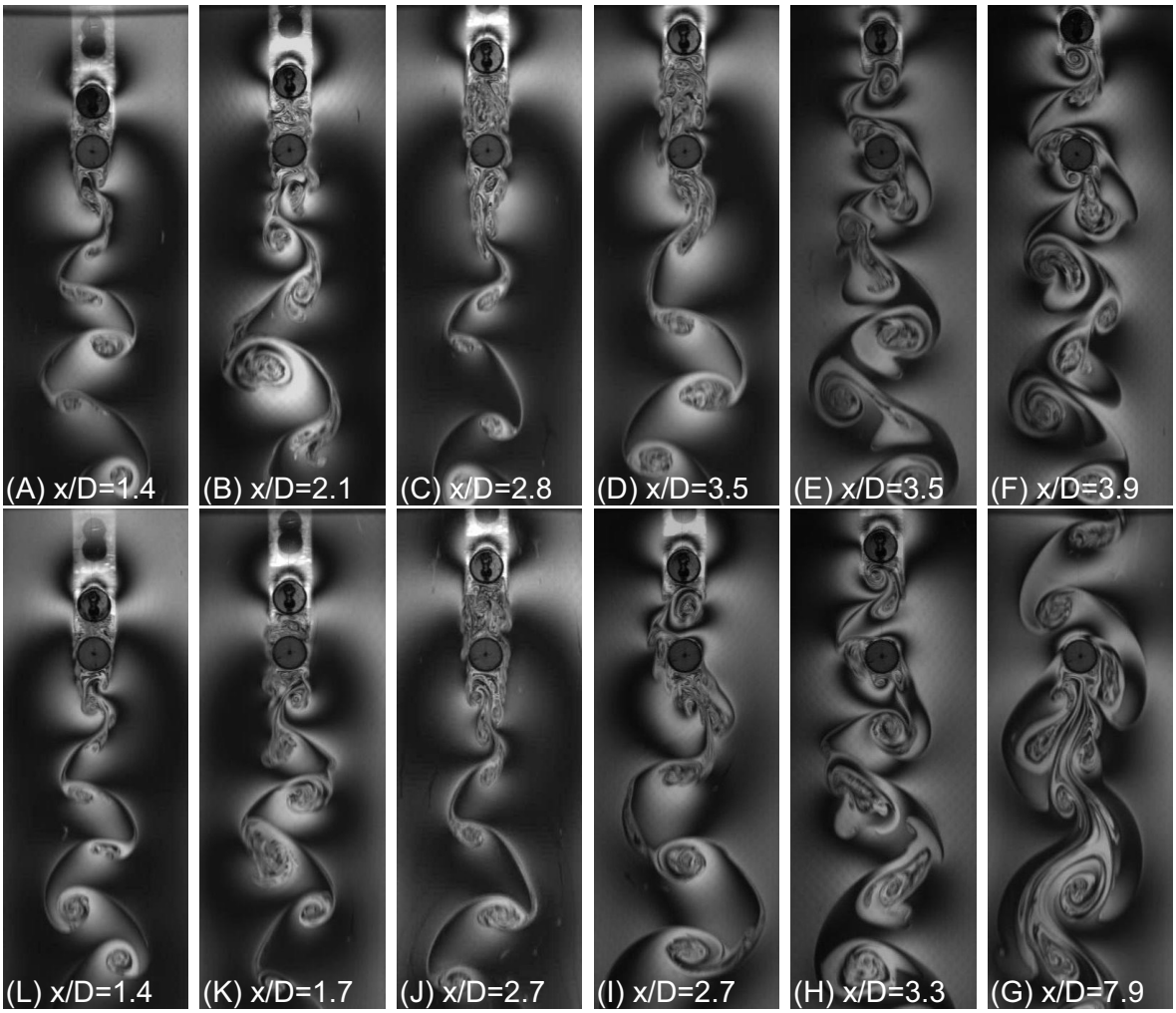

Figure 6.16: Wake pattern for various spacings

The mean drag coefficient shows obvious hysteresis between the increasing spacing process and the decreasing spacing process in Figure 6.15. To compare with the force measurement results conducted in the soap film, the mean drag of the downstream cylinder in a stationary tandem pair simulated by LBM is depicted as a blue dash line in Figure 6.15. The "drag" coefficient determined from the flowing soap film experiment actually includes the inertial force of the downstream disk. In Figure 6.15, the mean "drag" coefficients of the downstream disk agree with the results from the LBM simulation in terms of the minimum spacing and the maximum spacing. The stream-wise oscillation has the minimum vibration amplitude for both the minimum spacing and the maximum spacing, so the inertial force of the downstream disk is negligible in these cases. Therefore it is reasonable to expect that the "drag" measured in the experiment in these cases will approach that from the simulation results. For the smallest spacing ($\ell = 1.4$), the "drag" is negative, as shown in Figure 6.15, so the downstream disk is propelled forward by the wake of the upstream disk. For the simulation results in Figure 6.15, the negative drag regime occurs for small values ($\ell < 3.7$). However, due to the transverse oscillation, the downstream disk always deviates from the centerline of the wake in the experiments, and the resulting "drag" coefficient is positive for the spacings $1.6 < \ell < 2.7$. The "drag" coefficient displays a sharp increase when the spacing is around $\ell = 3.5$ during the increasing spacing process; while it shows a sharp decrease when the spacing is around $\ell = 2.7$ during the decreasing spacing process. Therefore, the critical spacing is around $\ell = 3.5$ for the increasing spacing process and around $\ell = 2.7$ for the decreasing spacing process. The wake patterns also show the corresponding bifurcation of the flow patterns, as shown in Figure 6.16 (D) and (E) for the increasing spacing process and in Figure 6.16 (I) and (J) for the decreasing spacing process. The simulation results also show a critical spacing between 3.7 and 3.8, as shown in Figure 6.15 for the sudden jump of the mean drag coefficient. The results suggest that the oscillation of the downstream disk decreases the critical spacing slightly. When the spacings are larger than the critical spacing,

	$\ell_{c,min}$	$\ell_{c,max}$
Flow-induced vibration	around 2.67	around 3.48
Two tandem stationary circular cylinders (experiment)	2.66–2.87	3.60–3.80
Two tandem stationary circular cylinders (2D simulation)		3.70–3.80

Table 6.2: Critical spacings for flow-induced vibration and two tandem cylinders.

the "drag" coefficient decreases with increase of the mean spacing and reaches close to 0.49 at the largest spacing of $\ell = 7.9$.

Figure 6.17 shows the Strouhal numbers for both the flow-induced vibration (the upstream disk is fixed and the downstream disk is free to oscillate) and two tandem stationary circular disks. Basically the Strouhal numbers of the flow-induced vibration agree with the results from two tandem stationary circular disks. The abrupt variation of the Strouhal number in Figure 6.17 indicates the critical spacings at which the wake patterns transition between the "reattachment" mode and the "co-shedding" mode. Table 6.2 summarizes the critical spacings for various experimental and simulation results. The critical spacing $\ell_{c,max}$ for the 2D simulation is between 3.70 and 3.80. The maximum critical spacing $\ell_{c,max}$ for the experiments of the two stationary disks is between 3.60 and 3.80, which is close to the simulation results. The minimum critical spacing $\ell_{c,min}$ for the two stationary disks is between 2.66 and 2.87. The minimum critical spacing $\ell_{c,min}$ of the flow-induced vibration experiment is also around 2.67. However, the maximum critical spacing $\ell_{c,max}$ is around 3.48 for the oscillating case so the wake of the flow-induced vibration is more likely to transition from the "reattachment" mode to the "co-shedding" mode when compared to the two tandem stationary disks experiment.

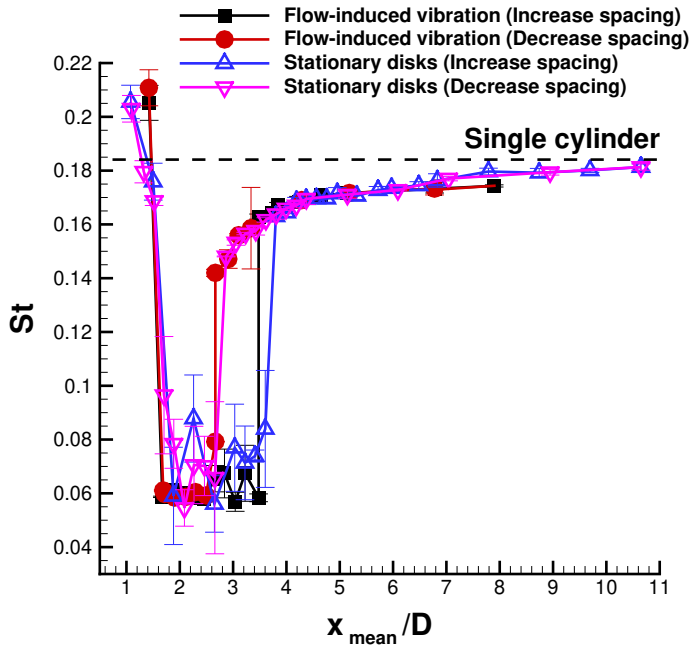

Figure 6.17: Force in longitudinal Direction.

6.5 Wake-stiffness model for the flow-induced vibration

Assi *et al.* [2] introduced a wake-stiffness model for the analysis of flow-induced vibration. This model focuses on the steady lift across the wake of a single stationary cylinder. Figure 6.18 shows the steady lift for two tandem spacings: (a) $\ell = 2.1$; (b) $\ell = 3.9$. The $C_{L_{mean}}$ values show a strongly linear behavior between $-0.4 \leq y/D \leq 0.4$ for $\ell = 2.1$ and between $-1.0 \leq y/D \leq 1.0$ for $\ell = 3.9$. Although the nonlinearities become obvious for larger transverse separation, we can estimate the slope in the linear region as

$$\left| \frac{\partial \bar{C}_{L_{mean}}}{\partial (y/D)} \right| \equiv \Delta \bar{c}_y. \tag{6.10}$$

$\Delta \bar{c}_y$ is 1.543 for $\ell = 2.1$ with 97.54% confidence inside the linear region, while $\Delta \bar{c}_y$ is 0.3794

for $\ell = 3.9$ with 95.4% confidence. For the wake-stiffness model, the steady lift is treated as a restoring force towards the centerline. That is, the $C_{L_{mean}}$ works as a "fluid-dynamic spring" driven by the flow within the region of wake interference when the upstream cylinder is fixed and the downstream cylinder oscillates around the wake centerline. The maximum oscillation amplitude in this flow-induced vibration setup is smaller than $0.4D$ for this particular situation, so the downstream cylinder moves in the linear wake interference region of the upstream cylinder.

The equivalent spring constant for the soap film setup is defined as

$$k_w = \frac{1}{2}\rho U_\infty^2 h_\mathrm{f} \Delta \bar{c}_y, \tag{6.11}$$

where h_f is the thickness of the soap film. The mass ratio is $O(30)$ so the effect of the added mass of the soap solution is negligible in the current analysis. For a pendulum system driven by gravity without damping effects, the equation of motion is

$$\frac{d^2\theta}{dt^2} + \frac{g}{l}\theta = 0 \tag{6.12}$$

under the small amplitude approximation. If we add the wake-stiffness effect, the equation becomes

$$\frac{d^2\theta}{dt^2} + \frac{g}{l}\theta + \frac{k_w}{m}\theta = \frac{d^2\theta}{dt^2} + (\frac{g}{l} + \frac{k_w}{m})\theta = 0. \tag{6.13}$$

Now the frequency f_{w+g} is given by

$$f_{w+g} = \frac{1}{2\pi}\sqrt{\frac{g}{l} + \frac{k_w}{m}}. \tag{6.14}$$

ℓ	f_T	f_w	f_g	f_{w+g}
2.1	10.48	9.88	1.67	10.02
3.9	5.01	4.90	1.67	5.18

Table 6.3: Oscillation frequency predicted by wake-stiffness and gravity

The frequency determined only by the wake-stiffness will be

$$f_w = \frac{1}{2\pi}\sqrt{\frac{k_w}{m}}. \tag{6.15}$$

Table 6.3 shows multiple frequencies of the pendulum system. The frequency of the transverse motion f_T is $10.48Hz$ for $\ell = 2.1$ and the frequency becomes $5.01Hz$ for $\ell = 3.9$. The frequency based on the wake-stiffness model for $\ell = 2.1$ is $9.88Hz$, while this frequency becomes $4.90Hz$ for $\ell = 3.9$. The frequency of the pendulum driven only by gravity is $1.67Hz$. Thus, the frequency determined by combining the wake-stiffness model and the pendulum model is 10.02 Hz for $\ell = 2.1$, and this frequency is 5.18 Hz for $\ell = 3.9$. Assi *et al.* [2] only applied the wake-stiffness model for cylinder separations of $\ell \geq 4.0$, for which a developed wake was observed to be present in the gap. The steady lift results in this section indicate that the wake-stiffness model also works for the gap flow switching wake region with $2.1 \leq \ell \leq 4.0$.

6.6 Conclusions

In the presented study, we discussed the two-dimensional wake-induced vibration of the downstream cylinder in a tandem pair for a vertical flowing soap film. The results include both the motion of the downstream disk and flow visualization of the wake pattern for $Re \approx 148$. As the longitudinal spacing of the cylinders is varied, flow visualization results show three types of flow: the "extended-body" wake, the "gap-flow switching" wake

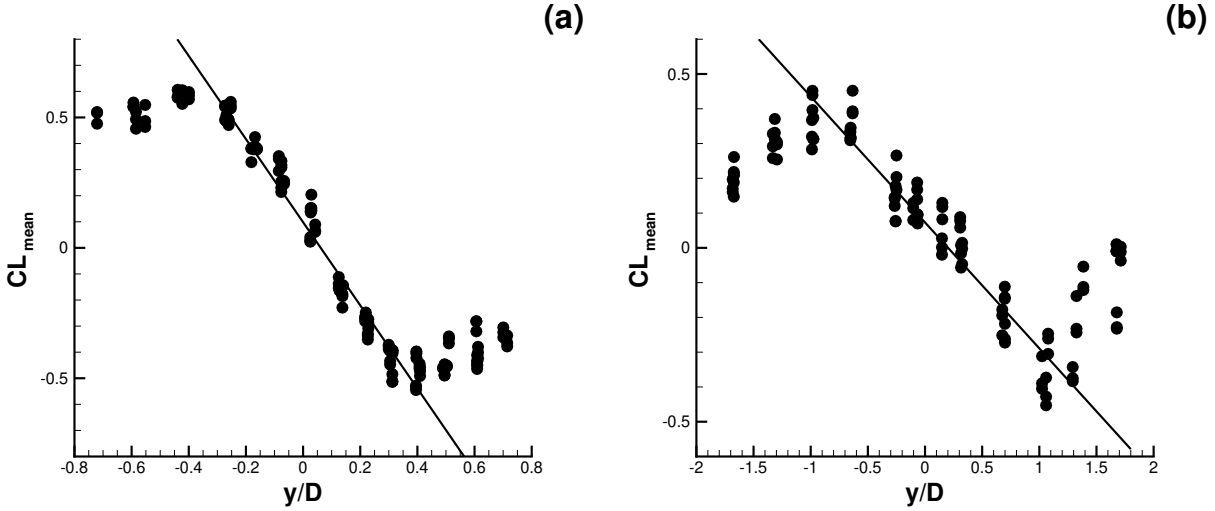

Figure 6.18: Steady lift coefficient on a static downstream cylinder and various staggered positions at two longitudinal spacing: (a)$\ell = 2.1$; (b)$\ell = 3.9$.

and the "co-shedding" wake. The downstream disk remains stationary, moves on a narrow "figure-8" shape, or vibrates inconsistently along a one-dimensional path, respectively, for the above three types of wake patterns. With the ability to tie together the wake structure, the object motion and the mean "drag" coefficient, we investigate the hysteresis between an incremented spacing process and a decremented spacing process. The hysteresis is not obvious in the variation of the motion amplitudes. However, the mean "drag" coefficient shows a remarkable hysteresis effect with the change in cylinder spacing. For the "gap-flow switching" wake regime, the downstream disk achieves a maximum oscillation amplitude and relatively consistent vibration, so this regime is suitable for energy harvesting. The wake-stiffness model was used to analyze the transverse oscillation. The steady lift across the wake of a single stationary cylinder appears to give strongly linear behavior in a region near the centerline. The slope of the linear fitting represents the "wake-stiffness", which predicts the oscillation frequency of the transverse motion. The wake-stiffness model works for both the "gap-flow switching" wake and the "co-shedding" wake. These research results could help with the optimization of energy harvesting systems based on flow-induced vibration of

circular-cylinder systems, and also benefit the understanding of wake interactions between multiple bluff bodies such as schooling fish, natural draft cooling towers and wind turbine farms.

Chapter 7

Summary

This PhD research work consists of two closely associated parts: a study of the vortex shedding of a single cylinder and a study of the wake interaction of two tandem cylinders. Flow visualization from flowing soap film experiments and two-dimensional numerical simulations were used to investigate the wakes behind the circular cylinders. Flowing soap films provide a beautiful platform for quasi-two-dimensional experiments, and the simulations based on the 2D Lattice Boltzmann method supplied many additional features and details of the wake structures. Data analysis methods such as proper orthogonal deocmposition, neural nets and support vector machine algorithms were used to uncover and understand several important behaviors of vortex formation and interaction behind circular cylinders.

A new definition of the vortex formation length was constructed using POD analysis in both the two-dimensional simulations and the quasi-two-dimensional experiments. This definition is based on the unsteady flow fields and helps with understanding the wake interaction between two tandem cylinders. The POD mode plots identify two formation lengths: the maximum vortex formation length and the minimum vortex formation length. The former length is related to the maximum critical spacing of two tandem circular cylinders, while the latter length is related to the minimum critical spacing. The experimental and simulation results also indicate that the POD analysis is capable of predicting the spatial distribution and time evolution of the vortex shedding and propogation.

A systematic parametric study of the wake structure behind a controlled transversely os-

cillating cylinder was conducted. Neural network and support vector machine algorithms helped with the wake classification and the boundary identification between different wake regimes. The critical parameters considered in this research were the normalized wavelength λ^*, the normalized amplitude A^*, and the frequency ratio f^*. The wake modes were distinguished in two phase maps: (λ^*,A^*) and the (f^*,A^*) space. The existing literature shows significant differences between the maps of vortex-shedding regimes in experiments (3D) and simulations (2D). The present experiments in a quasi-2D flowing soap film were implemented to investigate the impact of system dimensionality on the wake patterns generated behind an oscillating cylinder. The experimental results show that the "2P" wake structure can occur in a (quasi) two-dimensional experiment, results that are consistent with earlier findings for in-line cylinder oscillations [22]. The phase map of the vortex shedding regimes for the (quasi) two-dimensional experiments qualitatively agrees with that from previous experiments (3D). One possible reason why this (quasi) two-dimensional experiment disagrees with the 2D simulation is the existence of the meniscus (a cylinder-film intersection). Due to the similarity with the real 3D wake flow, the soap film experimental data could assist with understanding of the real 3D vortex-induced vibration.

The critical spacing of two identical tandem circular cylinders in a flowing soap film system at $Re \approx 100$ was determined using visual inspections of the wake patterns and calculations of the Strouhal frequencies. Three trials were run with cylinder spacings varying over the range $1.3 \leq \ell \leq 6.6$. The dimesionless spacing ℓ was both increased and decreased quasi-statically with increments $0.1 \leq \Delta\ell \leq 0.9$. Hysteresis was observed in the flow patterns and Strouhal numbers. As ℓ was increased, the transition from the reattachment regime to the co-shedding regime occurred for a critical spacing of $3.9 \lesssim \ell_{c,max} \lesssim 4.1$. When instead ℓ was decreased, this transition occurred for a critical spacing of $2.9 \lesssim \ell_{c,min} \lesssim 3.1$. Thus, for this flowing soap film system with Re = 99 ($\pm$7), the critical spacing of two identical tandem

circular cylinders was found to be $2.9 \lesssim \ell_c \lesssim 4.1$. This study appears to provide the first experimental evidence of critical spacing values that agree with published computational results.

The two-dimensional wake-induced vibration of the downstream cylinder in a tandem pair was also studied using a vertical flowing soap film. The results include both the motion of the downstream disk and flow visualization of the wake pattern for $Re = 150$. With variation of the longitudinal spacing, the flow visualization results show three types of flow: an "extended-body" wake, a "gap-flow switching" wake, and a "co-shedding" wake. The downstream disk remains stationary, moves in a narrow "figure-8" shape, or vibrates inconsistently in a one-dimensional direction, respectively, for the above three types of wake patterns. With the ability to tie together the wake structure, the object motion and the mean "drag" coefficient, the hysteresis between the spacing increment process and the spacing decrement process was investigated. The hysteresis was not obvious in the variation of the motion amplitudes with the change of the spacing. However, the mean "drag" coefficient showed a remarkable hysteresis effect with the change of the spacing. For the "gap-flow switching" wake regime, the downstream disk showed a maximum oscillation amplitude and relatively consistent vibration, so this regime is considered suitable for energy harvesting. The wake-stiffness model was used to analyze the transverse oscillation. The steady lift across the wake of a single stationary cylinder appears to display a strongly linear behavior. The slope of the linear fit determines the "wake-stiffness", which predicts the oscillation frequency of the transverse motion. The wake-stiffness model works well for both the "gap-flow switching" wake and the "co-shedding" wake. These research results can help with the optimization of energy harvesting systems based on flow-induced vibration of circular-cylinder systems, and also benefit the understanding of wake interactions between multiple bluff bodies such as schooling fish, natural draft cooling towers, and wind turbine farms.

Bibliography

[1] Aref, H., Stremler, M. A. & Ponta, F. L. 2006 Exotic vortex wakes - point vortex solutions. *Journal of Fluids and Structures* **22** (6-7), 929–940.

[2] Assi, G. R. S., Bearman, P. W., Carmo, B. S., Meneghini, J. R., Sherwin, S. J. & Willden, R. H. J. 2013 The role of wake stiffness on the wake-induced vibration of the downstream cylinder of a tandem pair. *Journal of Fluid Mechanics* **718**, 210–245.

[3] Assi, G. R. S., Bearman, P. W. & Meneghini, J. R. 2010 On the wake-induced vibration of tandem circular cylinders: the vortex interaction excitation mechanism. *Journal of Fluid Mechanics* **661**, 365–401.

[4] Auliel, M I, Castro, F, Sosa, R & Artana, G 2015 Gravity-driven soap film dynamics in subcritical regimes. *Physical Review E* **92**, 043009.

[5] Bandi, M. M., Concha, A., Wood, R. & Mahadevan, L. 2013 A pendulum in a flowing soap film. *Physics of Fluids* **25** (4).

[6] Basu, S. & Stremler, M. A. 2015 On the motion of two point vortex pairs with glide-reflective symmetry in a periodic strip. *Physics of Fluids* **27** (10).

[7] Basu, S. & Stremler, M. A. 2017 Exploring the dynamics of '2p' wakes with reflective symmetry using point vortices. *Journal of Fluid Mechanics* **831**, 72–100.

[8] Bearman, P. W. 1965 Investigation of the flow behind a two-dimensional model with a blunt trailing edge and fitted with splitter plates. *Journal of Fluid Mechanics* **21** (2), 241–255.

[9] Beizaie, M. & Gharib, M. 1997 Fundamentals of a liquid (soap) film tunnel. *Experiments in Fluids* **23** (2), 130–140.

[10] Bernitsas, M. M., Raghavan, K., Ben-Simon, Y. & Garcia, E. M. H. 2008 Vivace (vortex induced vibration aquatic clean energy): A new concept in generation of clean and renewable energy from fluid flow. *Journal of Offshore Mechanics and Arctic Engineering-Transactions of the Asme* **130** (4).

[11] Bhatnagar, P. L., Gross, E. P. & Krook, M. 1954 A model for collision processes in gases .1. small amplitude processes in charged and neutral one-component systems. *Physical Review* **94** (3), 511–525.

[12] Blondeaux, P., Fornarelli, F., Guglielmini, L., Triantafyllou, M. S. & Verzicco, R. 2005 Numerical experiments on flapping foils mimicking fish-like locomotion. *Physics of Fluids* **17** (11).

[13] Bokaian, A. & Geoola, F. 1984 Wake-induced galloping of 2 interfering circular-cylinders. *Journal of Fluid Mechanics* **146** (Sep), 383–415.

[14] Bos, F. M., Lentink, D., Van Oudheusden, B. W. & Bijl, H. 2008 Influence of wing kinematics on aerodynamic performance in hovering insect flight. *Journal of Fluid Mechanics* **594**, 341–368.

[15] Bouzidi, M., Firdaouss, M. & Lallemand, P. 2001 Momentum transfer of a boltzmann-lattice fluid with boundaries. *Physics of Fluids* **13** (11), 3452–3459.

[16] Carmo, B. S. & Meneghini, J. R. 2006 Numerical investigation of the flow around two circular cylinders in tandem. *Journal of Fluids and Structures* **22** (6-7), 979–988.

[17] Carmo, B. S., Meneghini, J. R. & Sherwin, S. J. 2010 Possible states in the flow around two circular cylinders in tandem with separations in the vicinity of the drag inversion spacing. *Physics of Fluids* **22** (5), 054101.

[18] Carmo, B. S., Meneghini, J. R. & Sherwin, S. J. 2010 Secondary instabilities in the flow around two circular cylinders in tandem. *Journal of Fluid Mechanics* **644**, 395–431.

[19] Chomaz, J. M. 2001 The dynamics of a viscous soap film with soluble surfactant. *Journal of Fluid Mechanics* **442**, 387–409.

[20] Colvert, B., Alsalman, M. & Kanso, E. 2018 Classifying vortex wakes using neural networks. *Bioinspiration and Biomimetics* **13** (2).

[21] Couder, Y. 1984 Two-dimensional grid turbulence in a thin liquid-film. *Journal De Physique Lettres* **45** (8), L353–L360.

[22] Couder, Y. & Basdevant, C. 1986 Experimental and numerical study of vortex couples in two-dimensional flows. *Journal of Fluid Mechanics* **173**, 225–251.

[23] Couder, Y., Chomaz, J. M. & Rabaud, M. 1989 On the hydrodynamics of soap films. *Physica D* **37** (1-3), 384–405.

[24] Dahmen, S. R. 2015 On pendulums and air resistance. *European Physical Journal H* **40** (3), 337–373.

[25] Didier, E. 2007 Flow simulations over two circular cylinders in tandem. *Comptes Rendus Mecanique* **335** (11), 696–701.

[26] Dong, Haibo, Mittal, Rajat, Bozkurttas, Meliha & Najjar, Fady 2005 *Wake Structure and Performance of Finite Aspect-Ratio Flapping Foils*. *Aerospace Sciences Meetings* 81. American Institute of Aeronautics and Astronautics.

[27] Filippova, O. & Hanel, D. 1998 Grid refinement for lattice-bgk models. *Journal of Computational Physics* **147** (1), 219–228.

[28] Gerrard, J. H. 1978 The wakes of cylindrical bluff bodies at low reynolds number. *Philosophical Transactions of the Royal Society of London. Series A, Mathematical and Physical Sciences* **288** (1354), 351–382.

[29] Gharib, M. & Derango, P. 1989 A liquid-film (soap film) tunnel to study two-dimensional laminar and turbulent shear flows. *Physica D* **37** (1-3), 406–416.

[30] Goodfellow, Ian, Bengio, Yoshua & Courville, Aaron 2016 *Deep Learning*. MIT Press, http://www.deeplearningbook.org.

[31] Green, R. B. & Gerrard, J. H. 1993 Vorticity measurements in the near wake of a circular-cylinder at low reynolds-numbers. *Journal of Fluid Mechanics* **246**, 675–691.

[32] Griffin, O. M. 1971 Unsteady wake of an oscillating cylinder at low reynolds number. *Journal of Applied Mechanics* **38** (4), 729–738.

[33] Griffin, O. M. 1974 Effects of synchronized cylinder vibration on vortex formation and mean flow. *In Flow-Induced Structural Vibrations, IUTAM/IAHR Symposium Karlsruhe 1972 (ed. E. Naudascher)* pp. 454–470.

[34] Griffin, O. M. 1995 A note on bluff-body vortex formation. *Journal of Fluid Mechanics* **284**, 217–224.

[35] Griffin, O. M. & Ramberg, S. E. 1974 Vortex-street wakes of vibrating cylinders. *Journal of Fluid Mechanics* **66** (Nov25), 553–+.

[36] Hover, F. S. & Triantafyllou, M. S. 2001 Galloping response of a cylinder with upstream wake interference. *Journal of Fluids and Structures* **15** (3-4), 503–512.

[37] Huhe-Aode, Tatsuno M. 1985 Visual studies of wake structure behind two cylinders in tandem arrangement. *Rep. Res. Inst. Appl. Mech. Kyushu Univ.* **32** (99), 1–20.

[38] Igarashi, Tamotsu 1981 Characteristics of the flow around two circular cylinders arranged in tandem. 1. *Bulletin of the Japan Society of Mechanical Engineers* **24** (188), 323–331.

[39] Ishigai, Seikan, Nishikawa, Eiichi, Nishimura, Keiya & Cho, Katsuzo 1972 Experimental study of structure of gas flow in tube banks with tube axes normal to flow Part I; Karman vortex flow from two tubes at various spacings. *Bulletin of the Japan Society of Mechanical Engineers* **15** (86), 949–956.

[40] Jauvtis, N. & Williamson, C. H. K. 2004 The effect of two degrees of freedom on vortex-induced vibration at low mass and damping. *Journal of Fluid Mechanics* **509**, 23–62.

[41] Jester, W. & Kallinderis, Y. 2003 Numerical study of incompressible flow about fixed cylinder pairs. *Journal of Fluids and Structures* **17** (4), 561–577.

[42] Jia, L. B. & Yin, X. Z. 2008 Passive oscillations of two tandem flexible filaments in a flowing soap film. *Physical Review Letters* **100** (22).

[43] Jia, L. B. & Yin, X. Z. 2009 Response modes of a flexible filament in the wake of a cylinder in a flowing soap film. *Physics of Fluids* **21** (10).

[44] Jiang, H. Y. & Cheng, L. 2017 Strouhal-reynolds number relationship for flow past a circular cylinder. *Journal of Fluid Mechanics* **832**, 170–188.

[45] Jiang, R. J., Lin, J. Z. & Ku, X. K. 2014 Numerical predictions of flows past two tandem cylinders of different diameters under unconfined and confined flows. *Fluid Dynamics Research* **46** (2), 22.

[46] Kármán, Th. von 1911 Über den mechanismus des widerstandes, den ein bewegter körper in einer flüssigkeit erfärt. 1. teil. Nachr. Ges. Wiss. Göttingen. Math.-Phys. Kl. pp. 509–517.

[47] Kármán, Th. von 1912 Über den mechanismus des flüssigkeits- und luftwiderstandes. *Phys. Z.* pp. 49–59.

[48] Kármán, Th. von 1912 Über den mechanismus des widerstandes, den ein bewegter körper in einer flüssigkeit erfärt. 2. teil. Nachr. Ges. Wiss. Göttingen. Math.-Phys. Kl. pp. 547–556.

[49] Kellay, H., Wu, X. L. & Goldburg, W. I. 1995 Experiments with turbulent soap films. *Physical Review Letters* **74** (20), 3975–3978.

[50] Kiya, M., Arie, M., Tamura, H. & Mori, H. 1980 Vortex Shedding From Two Circular Cylinders in Staggered Arrangement. *Journal of Fluids Engineering* **102** (2), 166.

[51] Kravchenko, Arthur G. 1998 B-spline methods and zonal grids for numerical simulations of turbulent flows. PhD thesis, copyright - Database copyright ProQuest LLC; ProQuest does not claim copyright in the individual underlying works; Last updated - 2017-03-07.

[52] Lee, Kyongjun, Yang, Kyung-Soo & Yoon, Dong-Hyeog 2009 Flow-induced forces on two circular cylinders in proximity. *Computers & Fluids* **38** (1), 111–120.

[53] Leontini, J. S., Stewart, B. E., Thompson, M. C. & Hourigan, K. 2006 Wake state and energy transitions of an oscillating cylinder at low reynolds number. *Physics of Fluids* **18** (6).

[54] Li, G. J. & Lu, X. Y. 2012 Force and power of flapping plates in a fluid. *Journal of Fluid Mechanics* **712**, 598–613.

[55] Li, J., Chambarel, A., Donneaud, M. & Martin, R. 1991 Numerical study of laminar-flow past one and 2 circular-cylinders. *Computers and Fluids* **19** (2), 155–170.

[56] Li, Y., Zhang, R., Shock, R. & Chen, H. 2009 Prediction of vortex shedding from a circular cylinder using a volumetric lattice-boltzmann boundary approach. *European Physical Journal-Special Topics* **171**, 91–97.

[57] Lin, J. Z., Jiang, R. J., Chen, Z. L. & Ku, X. K. 2013 Poiseuille flow-induced vibrations of two cylinders in tandem. *Journal of Fluids and Structures* **40**, 70–85.

[58] Ljungkrona, L., Norberg, Ch. & Sundén, B. 1991 Free-stream turbulence and tube spacing effects on surface pressure fluctuations for two tubes in an in-line arrangement. *Journal of Fluids and Structures* **5** (6), 701–727.

[59] Lumley, J. L. 1967 The structure of inhomogeneous turbulent flows. *Atmospheric Turbulence and Radio Wave Propagation* .

[60] Lumley, J. L. 1981 Coherent structures in turbulence. In *Transition and Turbulence* (ed. RICHARD E. MEYER), pp. 215 – 242. Academic Press.

[61] Mahír, Necati & Altaç, Zekeriya 2008 Numerical investigation of convective heat transfer in unsteady flow past two cylinders in tandem arrangements. *International Journal of Heat and Fluid Flow* **29** (5), 1309–1318.

[62] Mannini, C., Marra, A. M. & Bartoli, G. 2014 Viv-galloping instability of rectangular cylinders: Review and new experiments. *Journal of Wind Engineering and Industrial Aerodynamics* **132**, 109–124.

[63] Mareck, K., Jung, S., Shelley, M. & Zhang, J. 2006 The dynamics of a flexible loop in a quasi-two-dimensional flow. *Physics of Fluids* **18** (9).

[64] Meneghini, J. R., Saltara, F., Siqueira, C. L. R. & Ferrari, J. A. 2001 Numerical simulation of flow interference between two circular cylinders in tandem and side-by-side arrangements. *Journal of Fluids and Structures* **15** (2), 327–350.

[65] Mitchell, Tom M. 1997 *Machine Learning*. McGraw-Hill,.

[66] Mittal, S. 2005 Excitation of shear layer instability in flow past a cylinder at low reynolds number. *International Journal for Numerical Methods in Fluids* **49** (10), 1147–1167.

[67] Mizushima, J. & Suehiro, N. 2005 Instability and transition of flow past two tandem circular cylinders. *Physics of Fluids* **17** (10).

[68] Morse, T. L. & Williamson, C. H. K. 2006 Employing controlled vibrations to predict fluid forces on a cylinder undergoing vortex-induced vibration. *Journal of Fluids and Structures* **22** (6-7), 877–884.

[69] Morse, T. L. & Williamson, C. H. K. 2009 Prediction of vortex-induced vibration response by employing controlled motion. *Journal of Fluid Mechanics* **634**, 5–39.

[70] Morse, T. L. & Williamson, C. H. K. 2010 Steady, unsteady and transient vortex-induced vibration predicted using controlled motion data. *Journal of Fluid Mechanics* **649**, 429–451.

[71] Munir, A., Zhao, M., Wu, H. L., Ning, D. Z. & Lu, L. 2018 Numerical investigation of the effect of plane boundary on two-degree-of-freedom of vortex-induced vibration of a circular cylinder in oscillatory flow. *Ocean Engineering* **148**, 17–32.

[72] Mussa, A., Asinari, P. & Luo, L. S. 2009 Lattice boltzmann simulations of 2d laminar flows past two tandem cylinders. *Journal of Computational Physics* **228** (4), 983–999.

[73] Nishioka, M. & Sato, H. 1978 Mechanism of determination of shedding frequency of vortices behind a cylinder at low reynolds-numbers. *Journal of Fluid Mechanics* **89** (Nov), 49–60.

[74] Ohmi, Kazuo & Imaichi, Kensaku 1992 Vortex Wake Visualizations of Two Circular Cylinders in Parallel. In *Flow Visualization VI*, pp. 322–326. Berlin, Heidelberg: Springer.

[75] Ohmi, Kazuo, Li, Suxia, Jeon, Seunghee & Chen, Lingyun 2005 Vortex interference in the wake of two tandem circular cylinders in a cross flow. *Modern Physics Letters B* **19** (28-29), 1595–1598.

[76] Ohya, Yuji, Okajima, Atsushi & Hayashi, Masanori 1988 Wake Interference and Vortex Shedding. In *Encyclopedia of Fluid Mechanics, volume 8* (ed. N. P. Cheremisinoff), chap. 10, pp. 323–389.

[77] Papaioannou, G. V., Yue, D. K. P., Triantafyllou, M. S. & Karniadakis, G. E. 2006 Three-dimensionality effects in flow around two tandem cylinders. *Journal of Fluid Mechanics* **558**, 387–413.

[78] Papaioannou, G. V., Yue, D. K. P., Triantafyllou, M. S. & Karniadakis, G. E. 2008 On the effect of spacing on the vortex-induced vibrations of two tandem cylinders. *Journal of Fluids and Structures* **24** (6), 833–854.

[79] Park, J., Kwon, K. & Choi, H. 1998 Numerical solutions of flow past a circular cylinder at reynolds numbers up to 160. *Ksme International Journal* **12** (6), 1200–1205.

[80] Posdziech, O. & Grundmann, R. 2007 A systematic approach to the numerical calculation of fundamental quantities of the two-dimensional flow over a circular cylinder. *Journal of Fluids and Structures* **23** (3), 479–499.

[81] Qin, B., Alam, M. M. & Zhou, Y. 2017 Two tandem cylinders of different diameters in cross-flow: flow-induced vibration. *Journal of Fluid Mechanics* **829**, 621–658.

[82] Qu, L. X., Norberg, C., Davidson, L., Peng, S. H. & Wang, F. J. 2013 Quantitative numerical analysis of flow past a circular cylinder at reynolds number between 50 and 200. *Journal of Fluids and Structures* **39**, 347–370.

[83] Rahimi, Ali & Recht, Benjamin 2008 Random features for large-scale kernel machines. In *Advances in Neural Information Processing Systems 20* (ed. J. C. Platt, D. Koller, Y. Singer & S. T. Roweis), pp. 1177–1184. Curran Associates, Inc.

[84] Ripley, Brian D. 1996 *Pattern recognition and neural networks*. Cambridge University Press.

[85] Rutgers, M. A., Wu, X. I., Bhagavatula, R., Petersen, A. A. & Goldburg, W. I. 1996 Two-dimensional velocity profiles and laminar boundary layers in flowing soap films. *Physics of Fluids* **8** (11), 2847–2854.

[86] Rutgers, M. A., Wu, X. L. & Daniel, W. B. 2001 Conducting fluid dynamics experiments with vertically falling soap films. *Review of Scientific Instruments* **72** (7), 3025–3037.

[87] Schaefer, J. W. & Eskinazi, S. 1959 An analysis of the vortex street generated in a viscous fluid. *Journal of Fluid Mechanics* **6** (2), 241–260.

[88] Schnipper, T., Andersen, A. & Bohr, T. 2009 Vortex wakes of a flapping foil. *Journal of Fluid Mechanics* **633**, 411–423.

[89] Sharman, B., Lien, F. S., Davidson, L. & Norberg, C. 2005 Numerical predictions of low reynolds number flows over two tandem circular cylinders. *International Journal for Numerical Methods in Fluids* **47** (5), 423–447.

[90] Shi, J. M., Gerlach, D., Breuer, M., Biswas, G. & Durst, F. 2004 Heating effect on steady and unsteady horizontal laminar flow of air past a circular cylinder. *Physics of Fluids* **16** (12), 4331–4345.

[91] Singha, Sintu & Sinhamahapatra, K. P. 2010 High-Resolution Numerical Simulation of Low Reynolds Number Incompressible Flow About Two Cylinders in Tandem. *Journal of Fluids Engineering* **132** (1), 011101.

[92] Stalberg, E., Bruger, A., Lotstedt, P., Johansson, A. V. & Henningson, D. S. 2006 High order accurate solution of flow past a circular cylinder. *Journal of Scientific Computing* **27** (1-3), 431–441.

[93] Sumner, D. 2010 Two circular cylinders in cross-flow: A review. *Journal of Fluids and Structures* **26** (6), 849–899.

[94] Tasaka, Yuji, Kon, Seiji, Schouveiler, Lionel & Le Gal, Patrice 2006 Hysteretic mode exchange in the wake of two circular cylinders in tandem. *Physics of Fluids* **18** (8), 084104.

[95] Tu, J. H., Zhou, D., Bao, Y., Ma, J., Lu, J. B. & Han, Z. L. 2015 Flow-induced vibrations of two circular cylinders in tandem with shear flow at low reynolds number. *Journal of Fluids and Structures* **59**, 224–251.

[96] Unal, M. F. & Rockwell, D. 1988 On vortex formation from a cylinder .1. the initial instability. *Journal of Fluid Mechanics* **190**, 491–512.

[97] Vu, Huy Cong, Ahn, Jungkyu & Hwang, Jin Hwan 2016 Numerical simulation of flow past two circular cylinders in tandem and side-by-side arrangement at low Reynolds numbers. *KSCE Journal of Civil Engineering* **20** (4), 1594–1604.

[98] Wang, S. Y., Tian, F. B., Jia, L. B., Lu, X. Y. & Yin, X. Z. 2010 Secondary vortex street in the wake of two tandem circular cylinders at low reynolds number. *Physical Review E* **81** (3).

[99] Wang, X. K., Su, B. Y. & Tan, S. K. 2012 Experimental study of vortex-induced vibrations of a tethered cylinder. *Journal of Fluids and Structures* **34**, 51–67.

[100] Wang, Z. J., Birch, J. M. & Dickinson, M. H. 2004 Unsteady forces and flows in low reynolds number hovering flight: two-dimensional computations vs robotic wing experiments. *Journal of Experimental Biology* **207** (3), 449–460.

[101] Weidman, Patrick D. 1968 Wake transition and blockage effects on cylinder base pressures.

[102] Wen, C. Y. & Lin, C. Y. 2001 Two-dimensional vortex shedding of a circular cylinder. *Physics of Fluids* **13** (3), 557–560.

[103] Williamson, C. H. K. 1996 Vortex dynamics in the cylinder wake. *Annual Review of Fluid Mechanics* **28**, 477–539.

[104] Williamson, C. H. K. & Brown, G. L. 1998 A series in 1/root re to represent the strouhal-reynolds number relationship of the cylinder wake. *Journal of Fluids and Structures* **12** (8), 1073–1085.

[105] Williamson, C. H. K. & Roshko, A. 1988 Vortex formation in the wake of an oscillating cylinder. *Journal of Fluids and Structures* **2** (4), 355–381.

[106] Wu, M. H., Wen, C. Y., Yen, R. H., Weng, M. C. & Wang, A. B. 2004 Experimental and numerical study of the separation angle for flow around a circular cylinder at low reynolds number. *Journal of Fluid Mechanics* **515**, 233–260.

[107] Wu, X. L., Levine, R., Rutgers, M., Kellay, H. & Goldburg, W. I. 2001 Infrared technique for measuring thickness of a flowing soap film. *Review of Scientific Instruments* **72** (5), 2467–2471.

[108] Xu, G. & Zhou, Y. 2004 Strouhal numbers in the wake of two inline cylinders. *Experiments in Fluids* **37** (2), 248–256.

[109] Yu, D. Z., Mei, R. W. & Shyy, W. 2002 A multi-block lattice boltzmann method for viscous fluid flows. *International Journal for Numerical Methods in Fluids* **39** (2), 99–120.

[110] Yuan, R. F., Zhong, C. W. & Zhang, H. 2015 An immersed-boundary method based on the gas kinetic bgk scheme for incompressible viscous flow. *Journal of Computational Physics* **296**, 184–208.

[111] Zdravkovich, M. M. 1977 Review—review of flow interference between two circular cylinders in various arrangements. *Journal of Fluids Engineering* **99** (4), 618–633.

[112] Zdravkovich, M. M. 1984 Classification of flow-induced oscillations of two parallel circular cylinders in various arrangements. *ASME Symposium on Flow-Induced Vibrations* **2**, 1–18.

[113] Zdravkovich, M. M. 1987 The effects of interference between circular cylinders in cross flow??????an earlier version as originally presented as an invited paper, entitled "forces on pipe clusters", at the international symposium on separated flow around

marine structures, norwegian institute of technology, trondheim, norway, 26–28 june 1985. *Journal of Fluids and Structures* **1** (2), 239–261.

[114] Zdravkovich, M. M. 1988 Review of interference-induced oscillations in flow past 2 parallel circular-cylinders in various arrangements. *Journal of Wind Engineering and Industrial Aerodynamics* **28** (1-3), 183–200.

[115] Zdravkovich, M. M. 1996 Different modes of vortex shedding: An overview. *Journal of Fluids and Structures* **10** (5), 427–437.

[116] Zdravkovich, M. M. & Medeiros, E. B. 1991 Effect of damping on interference-induced oscillations of 2 identical circular-cylinders. *Journal of Wind Engineering and Industrial Aerodynamics* **38** (2-3), 197–211.

[117] Zhang, J., Childress, S., Libchaber, A. & Shelley, M. 2000 Flexible filaments in a flowing soap film as a model for one-dimensional flags in a two-dimensional wind. *Nature* **408** (6814), 835–839.

[118] Zhou, Y. & Alam, M. M. 2016 Wake of two interacting circular cylinders: A review. *International Journal of Heat and Fluid Flow* **62**, 510–537.